5-2012

Production of Green Aromatics and Olefins from Lignocellulosic Biomass by Catalytic Fast Pyrolysis: Chemistry, Catalysis, and Process Development

Jungho Jae
University of Massachusetts Amherst, jae@ecs.umass.edu

Recommended Citation
Jae, Jungho, "Production of Green Aromatics and Olefins from Lignocellulosic Biomass by Catalytic Fast Pyrolysis: Chemistry, Catalysis, and Process Development" (2012). *Open Access Dissertations*. 553.
https://doi.org/10.7275/ntt1-1y36 https://scholarworks.umass.edu/open_access_dissertations/553

PRODUCTION OF GREEN AROMATICS AND OLEFINS FROM LIGNOCELLULOSIC BIOMASS BY CATALYTIC FAST PYROLYSIS: CHEMISTRY, CATALYSIS, AND PROCESS DEVELOPMENT

A Dissertation Presented

by

Jungho Jae

Submitted to the Graduate School of the
University of Massachusetts Amherst in partial fulfillment
of the requirements for the degree of

DOCTOR OF PHILOSOPHY

May 2012

Chemical Engineering

PRODUCTION OF GREEN AROMATICS AND OLEFINS FROM LIGNOCELLULOSIC BIOMASS BY CATALYTIC FAST PYROLYSIS: CHEMISTRY, CATALYSIS, AND PROCESS DEVELOPMENT

A Dissertation Presented

by

JUNGHO JAE

Approved as to style and content by:

George W. Huber, Chair

Wei Fan, Member

W. Curt Conner, Member

Scott M. Auerbach, Member

T. J. (Lakis) Mountziaris, Department Head
Chemical Engineering

ACKNOWLEDGEMENTS

First of all, I would like to express my deepest appreciation to my advisor, Prof. George W. Huber, for his guidance and support. I was very excited and motivated during my doctoral studies owing to his invaluable encouragement and inspiration. I am lucky to meet him as my advisor here at Umass. I am also very thankful to Prof. Scott Auerbach, Prof. Curt Conner, and Prof. Wei Fan, for being not only my committee members but also their help and suggestions in many ways. Especially, I do thank Prof. Auerbach for giving me deep insights into this research.

Next, I express my thanks to my colleagues for this study. I thank Dr. Geoff Tompsett, Torren Carlson, Yu-ting Cheng, Yu-chuan Lin, and Robert Coolman in the Huber group for a fruitful collaboration on the CFP project. Their help, hard work, and enlightening discussions make it possible to publish several good papers. Especially, I do thank Dr. Tompsett for his help to revise my thesis. I would also like to thank Dr. Jiacheng Shen and Dr. Taiying Zhang in the Wyman group for the collaboration on biomass depolymerization project. They have carried out the extensive hydrolysis experiments. I would also like to thank Andrew Foster in the Lobo group for the collarboration on zeolite catalyst design for CFP project. He has carried out the synthesis of mesoporous ZSM-5 and several zeolite catalysts. Their contributions in this thesis are greatly valued. I would like to thank all the other present and past group members of the Huber group for all their help.

I am also grateful for my friends from the Amherst Korean Church. Their friendships and encouragements always made me to be happy, healthy, and motivated.

Lastly, I owe a special gratitude to my parents, Young Sung Jae and Ja Jung Kim, who always supported and believed in me. Their encouragement and indispensable love made possible what I am now. I greatly thank my mother who has given me endless courage, and prayed for my health and good future.

This work was supported by the National Science Foundation (CBET division) through a CAREER grant and an MRI award, John and Elizabeth Armstrong, and the Defense Advanced Research Project Agency through the Defense Science Office Cooperative Agreement 30 W911NF-09-2-0010.

ABSTRACT

PRODUCTION OF GREEN AROMATICS AND OLEFINS FROM LIGNOCELLULOSIC BIOMASS BY CATALYTIC FAST PYROLYSIS: CHEMISTRY, CATALYSIS, AND PROCESS DEVELOPMENT

MAY 2012

JUNGHO JAE
B.S., SOGANG UNIVERSITY
M.S., CARNEGIE MELLON UNIVERSITY
Ph.D., UNIVERSITY OF MASSACHUSETTS AMHERST
Directed by: Professor George W. Huber

Diminishing petroleum resources combined with concerns about global warming and dependence on fossil fuels are leading our society to search for renewable sources of energy. In this respect, lignocellulosic biomass has a tremendous potential as a renewable energy source, once we develop the economical processes converting biomass into useful fuels and chemicals.

Catalytic fast pyrolysis (CFP) is a promising technology for production of gasoline range aromatics, including benzene, toluene, and xylenes (BTX), directly from raw solid biomass. In this single step process, solid biomass is fed into a catalytic reactor in which the biomass first thermally decomposes to form pyrolysis vapors. These pyrolysis vapors

then enter the zeolite catalysts and are converted into the desired aromatics and olefins along with CO, CO_2, H_2O, and coke. The major challenge with the CFP process is controlling the complicated homogeneous and heterogeneous reaction chemistry.

The focus of this thesis is to study the reaction chemistry, catalyst design, and process development for CFP to advance the CFP technology. To gain a fundamental understanding of the underlying chemistry of the process, we studied the reaction chemistry for CFP of glucose (i.e. biomass model compound). Glucose is thermally decomposed in a few seconds and produce dehydrated products, including anhydrosugars and furans. The dehydrated products then enter into the zeolite catalyst pore where they are converted into aromatics, CO, CO_2, H_2O and coke. The zeolite catalyzed step is far slower than the initial decomposition step (>2 min). Isotopic labeling studies revealed that the aromatics are formed from random hydrocarbon fragments composed of the dehydrated products. The major competing reaction to aromatic production is the formation of coke. The main coking reaction is the polymerization of the furan intermediates on the catalyst surface.

CFP is a shape selective reaction where the product selectivity is related to the zeolite pore size and structure. The shape selectivity of the zeolite catalysts in the CFP of glucose was systematically studied with different zeolites. The aromatic yield is a function of the pore size and internal pore space of the zeolite catalyst. Medium pore zeolites with pore sizes in the range of 5.2 to 5.9 Å and moderate pore intersection size, such as ZSM-5 and ZSM-11 produced the highest aromatic yield and least amount of coke. The kinetic diameter estimation of the aromatic products and the reactants revealed that the majority of these molecules can fit inside the zeolite pores of the medium pore zeolites. The ZSM-5

catalyst, the best catalyst for aromatic production, was modified further to improve its catalytic performance. These modifications include: (1) adjusting the concentration of acid sites inside the zeolites catalyst; (2) incorporation of mesoporosity into the ZSM-5 framework to enhance its diffusion characteristics, and (3) addition of Ga to the ZSM-5. Mesoporous ZSM-5 showed high selectivity for heavier alkylated monoaromatics. Ga promoted ZSM-5 increased the aromatic yield over 40%.

A process development unit was designed and built for continuous operation of the CFP process in a pilot scale. The effects of process variables such as temperature, biomass weight hourly space velocity, catalyst to biomass ratio, catalyst static bed height, and fluidization gas velocity were studied to optimize the reactor performance. It was demonstrated that CFP could produce liter quantities of aromatic products directly from solid biomass.

TABLE OF CONTENTS

Page

CHAPTER

LIST OF TABLES

Page

LIST OF FIGURES

Page

CHAPTER 1

INTRODUCTION

Diminishing petroleum resources combined with concerns about global warming and dependence on fossil fuels are leading our society to search for renewable sources of energy [1]. In this respect, plant biomass is the only current sustainable source of organic carbon, and biofuels, fuels derived from plant biomass, are the only renewable source of liquid fuels [2-3]. However, lignocellulosic biomass is not widely used as a liquid fuel feedstock because the economical processes for its conversion have yet to be developed [4]. Lignocellulosic biomass is primarily composed of three polymeric components: cellulose, hemicellulose, and lignin [3]. Cellulose and hemicelluloses are polysaccharide composed of glucose and C5 sugar monomers (e.g. xylose), while lignin is a complex network of different phenyl propane units(p-coumaryl alcohol, coniferyl alcohol, and sinapyl alcohol). Thus, the first step in any biomass to fuels conversion process is deconstruction of the solid lignocellulosic material into reactive intermediates that can be used as building blocks for fuels and chemicals. There are two major pathways to deconstruct lignocellulosic biomass: low temperature hydrolysis and high temperature thermal deconstruction. Hydrolysis-based pathways involve depolymerization of sugar polymers using either acids or enzymes, with the products from hydrolysis being sugar monomer solutions that can be fermented either to alcohols [5] or converted into alkanes or alcohols by liquid phase processing [6]. Thermal depolymerization of biomass can be achieved by fast pyrolysis. Typically, fast pyrolysis consists of rapidly heating biomass (>500℃ s^{-1}) to intermediate temperatures (400—600℃) forming pyrolysis vapors. These pyrolysis vapors can then be cooled to form a liquid fuel called a bio-oil or pyrolysis oil [7]. The other products obtained from fast pyrolysis of biomass are undesired char (solid products) and non-condensable gases (e.g. carbon dioxide). It is well known that high heating rates and short residence times are required to maximize the yield of pyrolysis oils [8-10]. Bio-oil is a complex mixture of more than 300 compounds resulting from thermal degradation of different biomass building blocks. The bio-oil can be directly used for low grade fuels or catalytically upgraded to gasoline and diesel range fuels. In this thesis we will estimate which pathway between hydrolysis and pyrolysis gives a maximum amount of fuel precursors (Chapter 3). Moreover, we will show how hydrolysis and pyrolysis could be combined as an integrated process to maximize the utility of carbon in biomass. This analysis will help us in developing cost-effective biomass conversion processes by determining the optimal pathway of biomass deconstruction.

Fast pyrolysis of biomass has been receiving much attention due to its simplicity and low process cost [7]. The current challenge in using pyrolysis oils is to develop economical processes for upgrading pyrolysis oil into marketable products not now commercially available [11]. The difficulties of bio-oil upgrading arise from the complex chemical composition of bio-oil which consists of various chemical functionalities such as ketones, aldehydes, acid, furanic derivatives, phenolics, and sugars. Several approaches have been studies to convert bio-oil to transportation fuels including hydrotreating [12-13], aqueous phase processing [14-15], and catalytic cracking with zeolite catalysts [16-22]. Elliott and co-workers[12-13] developed a two-step hydrotreating process in which an initial low temperature catalytic treatment at 270°C and 13.8 MPa for stabilizing bio-oil is followed by a high temperature hydrotreating at 400°C and 13.8 MPa for production of gasoline range fuels. The conventional hydrotreating catalyst, suldified Co-Mo supported on alumina, was used for both steps. Using this process, they were able to convert to 40% of the original bio-oil into completely deoxygenated products. Vispute et al. [14-15] developed an aqueous phase processing that can convert bio-oil into alkanes and hydrogen. Using this method, aqueous fraction of bio-oil is first hydrogenated with Ru/C catalyst at 125-175°C and 68.9 bar and undergoes aqueous phase dehydration/hydrogenation (APD/H) with Pt/SiO_2-Al_2O_3 catalyst at 260°C and 51.7 bar to produce hydrogen and alkanes. Up to 97% selectivity of alkanes is obtained when hydrogen and HCl are added to the reactor. The main drawbacks to hydrotreating and aqueous phase processing are high hydrogen consumption and severe operating conditions. In contrast, upgrading of bio-oil can be achieved without hydrogen and at atmospheric pressure using zeolite catalysts. Bakhshi and co-workers[23] converted maple wood-derived bio-oil to aromatic hydrocarbons of 27.9 wt% of bio-oil feed at a temperature of 290-410°C using HZSM-5 catalyst. However, severe catalyst coking of up to 30 – 40 wt% of the bio-oil was observed. Gayubo et al. [21] developed a two-step process in which the first step involves thermal treatment of the bio-oil at 400°C to remove thermally unstable coke precursors. The second step involves catalytic reactions of thermally treated bio-oil with HZSM-5 catalyst. This method can attenuate the deactivation of the HZSM-5 catalyst and increase the catalyst lifetime.

As an another approach, zeolite catalysts can be added to a pyrolysis reactor to convert the pyrolysis vapors directly into aromatic hydrocarbons in a process called catalytic fast pyrolysis (CFP) [24-27]. Catalytic fast pyrolysis (CFP) is a promising technology for production of gasoline range aromatics (up to 30% carbon) including benzene, toluene, and xylenes (BTX) directly from raw solid biomass. In this single step process, biomass, including wood, agricultural wastes or fast growing energy crops, is fed into a fluidized-bed reactor containing zeolite catalysts, where the biomass first thermally decomposes to form pyrolysis vapors. These pyrolysis vapors then enter the zeolite catalysts and are converted into the desired aromatics and olefins along with CO, CO_2, H_2O, and coke. The spent catalyst and coke are then sent to a regenerator where they are burned to provide process heat. The advantage of CFP is that pyrolysis and catalysis occurs in a single reactor with short residence times which greatly reduces process cost.

The focus of this thesis is to study the chemistry, catalyst design, and process development of catalytic fast pyrolysis. The major challenge with CFP process is controlling the complicated homogeneous and heterogeneous chemistry. Several researchers have studied the chemistry both for pyrolysis of biomass and conversion of pyrolysis vapors into aromatics over zeolite catalysts, respectively [28-30]. Lin et al. [28] suggested a reaction pathway for pyrolysis of cellulose. The first step in this pathway is the depolymerization of solid cellulose to form levoglucosan (LGA). Then, LGA can undergo dehydration and isomerization reactions to form other anhydrosugars including levoglucosenone (LGO), 1,4:3,6-dianhydro-β-d-glucopyranose (DGP) and 1,6-anhydro-β-d-glucofuranose (AGF). The anhydrosugars can react further to form furans such as furfural and hydroxymethylfurfural (HMF) by dehydration reactions, or hydroxyacetone, glycolaldehyde, and glyceraldehyde by fragmentation and retroaldol condensation reactions. Char is formed from polymerization of the pyrolysis products. Cheng et al. [29] studied the chemistry of furan conversion into aromatics with HZSM-5. They identified a key reaction mechanism for aromatic formation in which furan molecules are converted to intermediate species such as allene by decarbonylation and benzofuran by Diels-Alder condensation, and aromatics are produced via alkylation, cyclization, and reactions between olefins and furan. In this thesis we will study the combined homogeneous and heterogeneous chemistry of CFP of glucose with HZSM-5 catalyst (Chapter 4). We will propose the reaction pathway of glucose conversion into aromatics. This study ultimately will help us control the undesired coke formation reaction.

Zeolite catalysts play a critical role in aromatic production from CFP of biomass. Several researchers have studied catalytic pyrolysis of biomass using zeolite catalysts [26, 31-37] . The earliest work was reported by Chen et al. in 1980s [31]. They first showed that glucose, xylose, starch, and sucrose could be converted to aromatic hydrocarbons over HZSM-4 with low yields of 8-18wt% of biomass feed. Since then, several studies have been performed using various zeolite catalysts for catalytic pyrolysis of biomass. Pattiya et al. [33] tested HZSM-5 and several mesoporous (Al-MCM-41, Al-MSU-F, alumina-stabilized ceria MI-575) catalysts for the catalytic pyrolysis of cassava rhizome in a pyroprobe GC/MS system. All catalysts produced aromatic hydrocarbons and also improved the resulting bio-oil quality. They reported that HZSM-5 (Si/Al=50) yielded the most aromatic hydrocarbons. Mihalcik et al. [36] tested several zeolite catalysts, including H-Mordenite, HZSM-5, H-Y, H-Beta, and H-Ferrierite for catalytic pyrolysis of various biomass feedstocks (oak, corn stover, switchgrass, cellulose, lignin) in a pyroprobe GC/MS system. All zeolite catalysts decreased the oxygenated species of the resulting pyrolysis vapors compared to non-catalytic pyrolysis. Among the tested catalysts, HZSM-5 (pore size of 0.52-0.55 nm) was the most effective catalyst for production of aromatic hydrocarbons and deoxygenation of vapors. Aho et al.[34] studied the influence of zeolite structure for catalytic pyrolysis of pine wood in a fluidized bed reactor with 4 different zeolite catalysts, including H-Beta, H-Y, HZSM-5, and H-Mordenite. They reported that the chemical compositions of the resulting bio-oils are influenced by the structure of zeolites. HZSM-5 produced less acids and alcohols and more polyaromatics and ketones than other zeolites. In this thesis we will systematically study the shape selectivity of zeolite catalysts for CFP of glucose using a range of zeolite catalysts having a variety of pore size and structure (Chapter 5). We will establish the fundamental relationship between the zeolite pore size/structure and glucose conversion into aromatics. The insights into the zeolite catalyst design for CFP of biomass will also be presented.

To date, HZSM-5 has been known to be the most effective catalyst for the conversion of biomass derived molecules into aromatics [37]. For this reason, several researchers have studied the catalytic pyrolysis of biomass using modified HZSM-5 catalysts [19, 36, 38-39]. Mihalcik et al. [36] used ZSM-5 catalysts with different silica-to-alumina ratio (SiO_2/Al_2O_3=23, 50, and 80) in the catalytic pyrolysis of biomass feedstocks. They reported that the H-ZSM-5 catalyst with SiO_2/Al_2O_3=23 produced the highest yield of aromatics among the tested ZSM-5 catalysts. They suggested that the increase of aromatic yield could be due to an increase in density of available acid sites in the catalyst with low silica-to-alumina ratio. Park et al. [19] used mesoporous ZSM-5 catalysts in the upgrading of pine sawdust derived bio-oil. They reported that using mesoporous ZSM-5 decreased the bio-oil yield but increased the selectivity for aromatics such as benzene, toluene, and xylenes compared to using non-mesoporous ZSM-5. French et al.[38] used metal-substituted ZSM-5 catalysts for the catalytic pyrolysis of wood. They showed that high hydrocarbon yields (16wt%, including 3.5wt% of toluene) could be produced from nickel, cobalt, iron, and gallium-substituted ZSM-5. In this thesis we will show how ZSM-5 catalyst properties can be tuned to optimize aromatic production in the CFP of biomass (Chapter 6). The effects of 1) changing silica-to-alumina ratio, 2) changing particle size, 3) creating mesoporous structure in ZSM-5, and 4) adding metal to ZSM-5 on biomass CFP will be studied in detail to develop a better ZSM-5 catalyst. As we will show in this thesis, we have discovered a promising catalyst, a bifunctional Ga/ZSM-5 that can produce 40% more aromatics than ZSM-5.

Fluidized bed reactors have been used for catalytic pyrolysis of biomass due to their excellent mass and heat transfer properties, and scalability [24, 27, 40-41]. Olazar et al. [40] studied the catalytic pyrolysis of sawdust in a conical spouted bed reactor using HZSM-5 catalysts. The bottom section of the reactor has a conical shape and high velocity stream of gas induces circulation within the catalyst bed. They reported that catalytic pyrolysis of sawdust produced more water and deoxygenated products (aromatic yield of 6.3 wt%) than non-catalytic pyrolysis. Lappas et al. [41] performed the catalytic pyrolysis of pine wood in a circulating fluid bed reactor using a commercial fluid catalytic cracking catalyst and a ZSM-5 additive. The reactor was a lab-scale FCC unit, consisting of riser reactor, fluid bed regenerator, and stripper. They reported that addition of catalysts increased the yields of coke and gaseous products (CO and CO_2) but decreased the oxygenated compounds in liquid products by improving the bio-oil quality. Carlson et al. [24] reported on the use of a lab- scale bubbling fluidized bed reactor for the catalytic pyrolysis of sawdust using a spray dried ZSM-5 catalysts. They produced the highest hydrocarbon yields of 14% carbon for aromatics and 5.4 % carbon for olefins, respectively, at a low biomass weight hourly space velocity (0.1 hr^{-1}) and temperature of 600°C. Zhang et al. [27] studied the catalytic pyrolysis of corncobs in a bubbling fluidized bed reactor (30mm in diameter and 400mm in height) using HZSM-5 catalysts. They investigated the effects of operating parameters (reaction temperature, gas flow rate, static bed height, and biomass particle size) on product yields. The highest liquid yield (56.8 wt%) weas obtained at a pyrolysis temperature of 550°C, gas flow rate of 3.4 L/min, static bed height of 10 cm, and particle size of 1.0-2.0 mm. In this thesis we will study the CFP of biomass in a process development unit to demonstrate CFP technology in terms of scalability and capability for long time operation (Chapter 7). The effects of process variables such as temperature, biomass weight hourly space velocity, catalyst to biomass ratio, gas flow rate, and static bed height will be studied in detail to determine the optimum process conditions required to maximize aromatic hydrocarbon yield. This will be the first demonstration scale study in which a CFP process can produce liter quantities of aromatic products directly from lignocellulosic biomass.

The main objective of this thesis is to advance CFP technology by studying the chemistry, catalyst design, and process development of CFP. This thesis has five main objectives including:

1. Estimate the potential of the pyrolysis/CFP process for biomass conversion in an integrated biorefinery (Chapter 3)
2. Study the chemistry for the conversion of biomass to aromatics over HZSM-5 catalyst (Chapter 4)
3. Investigate the shape selectivity of the zeolite catalysts for CFP of biomass (Chapter 5)
4. Optimize the ZSM-5 catalyst properties to maximize aromatic production in the CFP process (Chapter 6)

5. Demonstrate scalability and capability for continuous operation of CFP technology in a process development unit (Chapter 7)

CHAPTER 2

EXPERIMENTAL METHODS

2.1 Pyroprobe

Catalytic fast pyrolysis experiments were conducted using a model 2000 pyroprobe analytical pyrolizer (CDS Analytical Inc.). The probe is a computer controlled resistively heated element which holds an open ended quartz tube (pictured in Figure 2.1). Powdered samples are held in the tube with loose quartz wool packing; during pyrolysis vapors flow from the open ends of the quartz tube into a larger cavity (the pyrolysis interface) with a helium carrier gas stream.

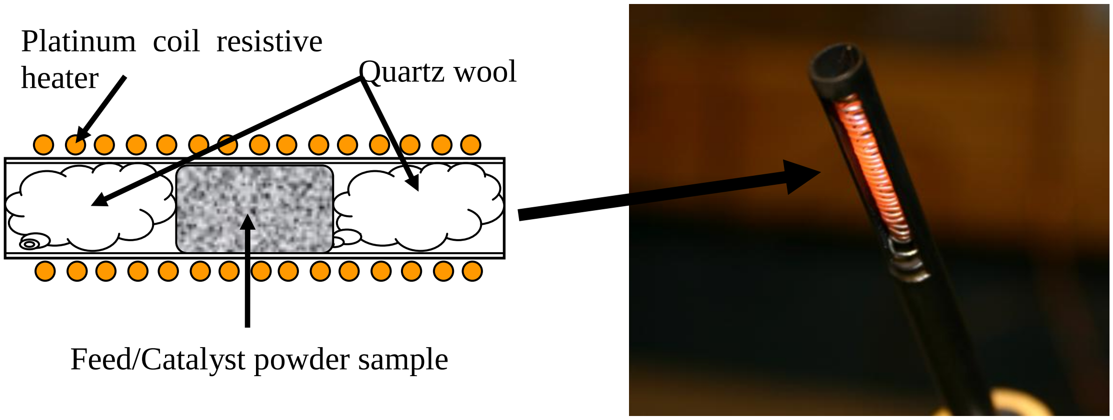

Figure 2.1 Diagram of the pyroprobe reactor setup. On the left a schematic cross-section of the prepared sample is pictured (not to scale). Powdered reactants and catalysts are held with loose quartz wool packing. Pictured on the right is the resistively heated element which holds the sample tube (2 mm x 25 mm). During reaction product vapors flow from the open ends of the sample tube into the GC/MS interface via a helium sweeper gas stream.

The carrier gas stream is routed to a model 5890 gas chromatograph (GC) interfaced with a Hewlett Packard model 5972A mass spectrometer (MS). The pyrolysis interface was held at 100 °C and the GC injector temperature used was 275 °C. Helium was used as the inert pyrolysis gas as well as the carrier gas for the GC/MS system. A 0.5

ml min^{-1} constant flow program was used for the GC capillary column (Restek Rtx-5sil MS). The GC oven was programmed with the following temperature regime: hold at 50 ℃ for 1 min, ramp to 200 ℃ at 10 ℃ min^{-1}, hold at 200 ℃ for 15 min. Products were quantified by injecting calibration standards into the GC/MS system. All yields are reported in terms of molar carbon yield where the moles of carbon in the product are divided by the moles of carbon in the reactant. The aromatic selectivity reported is defined as the moles of carbon in an aromatic species divided by the total moles aromatic species carbon. Similarly, the oxygenate selectivity is defined as the moles of carbon in an oxygenated species divided by the total moles oxygenated species carbon.

Powdered reactants were prepared by physically mixing the biomass feed and the catalyst. For a typical run 8-15 mg of reactant-catalyst mixture was used. Both the feed and the catalyst were sieved to <140 mesh before mixing. Carbon on the spent catalyst was quantified by elemental analysis (performed by Galbraith Laboratories using combustion, GLI method # ME-2).

For pure biomass pyrolysis experiments, an in-house designed trap was employed in the pyroprobe reactor to better quantify pyrolysis products (which are mostly thermally unstable). The trap consists of a 25 mL pyrex vial, a screw-tight frame with plug-valve controlled gas inlet and outlet, and the pyroprobe pyrolizer. A 1/4 inch channel allows the pyroprobe pyrolizer to be inserted from the top of frame into the center of vial. Prior to each trial, the vial was flushed with ultra-high purity helium at 50 mL min^{-1} flow rate for 10 minutes. After purging, the vial is made gastight by closing the outlet and inlet valves. The trap is then transferred in a dewar flask with a liquid nitrogen bath at 77 K, which allows rapid quenching of volatiles evolved during reaction. After reaction the condensed products on the walls of the vial are quantitatively removed with 1 mL of methanol. The methanol solution is then analyzed using a GC-MS (Shimadzu GC-2010 and QP2010S, analytes separated by Restek RTX-VMS). The carbon content of the condensed products was determined by Total Organic Carbon analyzer (TOC-V_{CPH}). For these measurements, the condensed products in the vial were dissolved with 20 ml of deionized water. The gaseous products such as CO and CO_2 were identified using the Py-GC-MS system. The weight of the final char was estimated by weighing the sample before and after pyrolysis using a Mettler Toledo microbalance with sensitivity of 0.001 mg. The carbon content of the final char was quantified by elemental analysis performed by Galbraith Laboratories.

2.2 Fixed Bed Reactor

Conversion of furan was carried out in a ½ inch diameter flow fixed bed reactor. Approximately 57 mg catalyst was loaded in the reactor. Prior to reaction, the catalyst bed was calcined in helium (Airgas, ultra-high purity) at 600˚C. Furan was fed via syringe pump (Fisher, KDS100) at a rate of 0.58 mL/h into 408 mL/min of helium, resulting in a furan partial pressure of 6 torr. The furan-containing stream was bypassed around the reactor for 30 min before switching to flow through the reactor. During reaction, the catalyst bed was maintained at 600 ℃ and ambient pressure. An air bath condenser was used to trap heavy products, and gas-phase products were collected in gas sampling bags. After 270 s of reaction, the flow of furan was stopped and the reactor was flushed with helium for 45 s. The spent catalyst was then treated in air at 600 ℃ to burn off accumulated coke. Any CO produced was further converted to CO_2 over a bed of CuO (Sigma-Aldrich) at 240 °C. The CO_2 was trapped by a CO_2 trap (Ascarite, Sigma-Aldrich).

Coke yield was calculated by measuring the weight change of the CO_2 trap. Gas-phase reaction products were analyzed by GC-FID (Shimadzu GC-2014). Gaseous species and coke deposited on the catalyst accounted for the vast majority of products. In our study, heavy products condensed in the liquid trap accounted for less than 0.05% of the total carbon fed through the reactor.

2.3 Lab Scale Fluidized Bed Reactor

A lab scale fluidized bed reactor is 2-in in diameter, 10-in in height and is made of 316 stainless steel. Inside the reactor, the catalyst bed was supported by a distributor plate made of stacked 316 stainless mesh (300 mesh). The solid biomass (pinewood) was introduced into the reactor from a sealed feed-hopper. Prior to the run, the pinewood was grinded and sieved to a particle size of 0.25 – 1 mm. During the reaction, the catalyst was fluidized by helium gas which was flowing at 800 mL/min to enable the reactor operates at bubbling fluidized bed flow regime. The hopper was continuously purged by helium at 200 mL/min to maintain an inert environment. Both the reactor and the inlet gas stream were heated to reaction temperature (550 °C). After the reactor the effluent flowed through a cyclone to remove particles. The effluent then flowed into 7 condensers in series to separate liquid and gas phase products. The first 3 condensers were placed in an ice-water bath with ethanol inside as a solvent, and the other 4 condensers were surrounded by a dry acetone bath (−55°C) without solvents. Finally, the uncondensed gas phase products were collected in air bags. The reaction time was 30 min. After reactions the reactor was purged by 1000 mL/min helium for 30 minutes to make sure that the only products remained inside the reactor was coke. Liquid products are extracted from condensers by ethanol.

Total volume of liquid is recorded. The catalyst was regenerated by air at 800 mL/min for 3 hours. During the regeneration, the effluent passed through a copper converter in which CO was converted into CO_2, and the CO_2 was trapped by a CO_2 trap. Gas phase products were analyzed by a GC-FID/TCD (Shimadzu 2014). Liquid samples were analyzed by a GC-FID (HP 7890). Coke yield was obtained by analyzing the weight change of the CO_2 trap.

2.4 Thermogravimetric Analysis with Mass Spectrometry (TGA-MS)

Thermogravimetric analysis was performed with a Q600 TGA system (TA Instruments). A quadruple mass spectrometer (Extorr XT 300) was coupled via a heated line to the TGA to measure the volatile species produced during pyrolysis. The heated transfer line was held at 250 ^{o}C to circumvent condensation of the product vapors. A low electron ionization voltage of 29 eV was used to suppress secondary fragmentation. The total pressure of ion source was 10^{-6} Torr. Ultra-high-purity helium (AirGas, NH) was used as the sweeper gas with a flow rate of 100 mL min^{-1}. For a typical run approximately 5 to 10 mg of biomass samples were used. Prior to all runs, samples were preheated to 110 ℃ for 30 minutes, under helium flow, to remove physically adsorbed water. Pyrolysis was then carried out from 50 ℃ to 600 ℃ with a designated heating rate (0.017, 0.25, or 2.5 ℃ s^{-1}).

2.5 NH_3 and IPA Temperature-Programmed Desorption (TPD)

A TGA-MS (Thermogravimetric Analysis-Mass Spectrometry) was used for the NH_3- and IPA-TPD study. About 30 mg of zeolite samples were placed in an alumina pan installed in a TGA (thermogravimetric analysis) chamber. The catalyst was pretreated at 600 °C under 100 mL/min air (Airgas, compressed air). The chamber then was cooled down to 35°C under 100 mL/min helium (Airgas, 99.999%). The temperature was kept at 35 °C under the helium flow for 2 h until the MS was stable. A 5% NH_3 (Airgas, helium balance) was fed into the TGA chamber from a side stream until the sample weight-curve was stable. After purging by 100mL/min helium for 40 min, the temperature was ramped to 700 °C at 10 °C/min. During the NH_3-TPD, the signal with m/z = 17 was monitored by MS. For IPA (isopropylamine, Sigma-Aldrich, 99%)-TPD, the same process was applied except that IPA was fed into the TGA chamber by using a bubbler surrounded by an ice-water bath. For IPA-TPD, signals with m/z = 41 (propylene) was monitored. In each TPD process we regenerated the catalyst at 600 °C and 100 mL/min air to obtain the weight of the clean catalyst (net weight). All spectra reported were normalized by the net weight.

2.6 Fourier-Transform Infrared (FTIR)

FTIR spectra were collected using a Bruker Equinox 55 infrared spectrometer. The KBr method was employed using spectroscopic grade KBr mixed with the zeolite/glucose obtained from the pyroprobe reactor in a 100: 5 weight ratio. An average of 50 scans at 4 cm^{-1} resolution were obtained for each KBr pellet. This method is as used by Bilba et al. [42] and Sharma et al.[43]. KBr pellet method was used due to the low quantity of samples prepared using the pyroprobe reactor.

The Brønsted to Lewis acid site ratio of the ZSM-5 catalyst was determined using ammonia as a probe molecule. Powder samples (~20 mg) were loaded into the DRIFTS cell and a spectrum of KBr (taken at ambient temperature before) was used as a background reference. Before the surface characterization was performed, the samples were activated by heating at 673 K for 2 h under helium (Airgas, UHP) flow of 20 mL min $^{-1}$, cooled down to 373 K, and saturated with ammonia (Airgas, anhydrous 99.99%) for 20–30 min. The gas flow was then switched back to helium (20 mL min $^{-1}$) to remove physically adsorbed ammonia, and the spectrum monitored until no change was observed (~30 min). The samples were then heated in helium flow (20 mL min $^{-1}$) to various temperatures. The spectra were recorded at each temperature up to 873 K. All of the spectra were obtained by subtraction of the corresponding background reference spectra. Data analysis and peak fitting were carried out using GRAMS/AI® software (ThermoScientific).

2.7 Powder X-ray Diffraction (XRD)

Powder X-ray diffraction was used to determine structures of the synthesized zeolite samples. A Philips X'Pert Pro diffractometer equipped with a X'Celerator detector was used to obtain X-ray patterns. An accelerating voltage of 45 kV was used at 40mA. Patterns were obtained at a scan rate of 0.1° (2θ) s $^{-1}$. Powder samples were compacted in an aluminum sample holder with the plane of the powder aligned with the holder surface.

2.8 Scanning Electron Microscopy (SEM)

Scanning Electron Microscopy (SEM, JEOL JEM-5400) was used to characterize the morphology and crystal size of zeolite catalysts. Samples were prepared by dispersing a small quantity of powder on an aluminum stub using a droplet of ethanol, followed by gold sputter coating.

2.9 Energy Dispersive X-ray Spectroscopy (EDS)

Energy Dispersive X-ray spectra of zeolite samples were collected using a JEOL JSM 7400F Scanning Electron Microscope to characterize bulk composition of zeolite samples. Samples were first coated with gold using a Denton Vacuum Desk IV sputtering system.

2.10 X-ray Photoelectron Spectroscopy (XPS)

X-ray photoelectron spectroscopy was used for surface chemical analysis of zeolite samples. X-ray photoelectron spectra recorded using a Physical Electronics XPS system equipped with an Al-anode X-ray generator and multi-channel hemispherical analyzer.

2.11 Nitrogen Adsorption

Nitrogen adsorption experiments was carried out at the normal boiling point of N_2 (-196 °C) for porosity measurements of the zeolite samples using an AUTOSORB® -1-MPC (Quantachrome Instruments; Boynton Beach, FL) gas adsorption system. Prior to the measurement, the samples were outgassed at 300 °C for 24 h under vacuum. Isotherms were analyzed using the t-plot method to calculate microporous volume and external surface area. The mesoporous volume and size distribution were calculated using the Barrett-Joyner-Halenda method on the adsorption branch of the isotherm.

2.12 Hydrolysis of Biomass

Hot water pretreatment (Extraction of cellulose and lignin) Tubular batch reactors (Hastelloy C-276, ½” O.D. × 0.035” wall thickness × 6” length) or a 1 L stirred Parr pressure reactor (Hastelloy C, Parr Instruments, Moline, IL) were used for pretreatment. The tube reactors were employed to test time-temperature combinations to optimize pretreatment for maximum hemicellulose release. The Parr reactor was then applied to treat larger quantities of biomass at the combination of time and temperature to give the highest sugar yields with the tubes. Both types of reactors were heated in 4 kW fluidized sand baths (Model SBL-2D, Techne Co., Princeton, NJ), and their internal temperature was monitored with a K type thermocouple probe (Omega CASS-18U-12, Omega Engineering Co., Stamford, CT). The heat-up time to the target temperature was about 3-4 min (not included in stated reaction times) [44].

The milled red maple was presoaked in water overnight at a solids loading of 10 wt% for use in both the tubular reactors and the Parr reactor. Temperatures of 160^{o}C, 180^{o}C, and 220^{o}C were tested at different pretreatment times. The reactor contents were quickly cooled at the end of the reaction time by immersing the reactors in a water bath, and the reactors cooled down to a temperature of 40℃ in about 40 seconds, with further hydrolysis stopping well before that. The maple residues were filtered, and the liquid fraction was collected. The pretreated solid fraction was thoroughly washed to remove solubles from the solid residues.

Enzymatic hydrolysis (Extraction of lignin) Washed pretreated maple solids were hydrolyzed at pH 4.8 and 50^{o}C in duplicates by following modified NREL LAP procedure [45]. Spezyme (SP) (activity 58.2 FPU/ml, protein content 116.0 mg/ml, Genencor, Rochester, NY) and Novozymes 188 (β-glucosidase, acitivity 665.0 CBU/ml, protein content 125.0 mg/ml, Franklinton, NC) were used at 2% biomass solids loadings, with the latter added to give a filter paper to beta-glucosidase activity ratio (FPU: CBU) of 1:4. A high enzyme loading of 60 FPU/g total glucan plus xylan in the pretreated solid was applied to determine the maximum possible sugar release. Samples were taken at selected time intervals.

Sugar Analysis Sugar monomers in the liquid portion were analyzed quantitatively by a Waters HPLC model 2695 system equipped with a 2414 refractive detector and a Waters 2695 autosampler using Millenium32 chromatography manager 3.2 software (Waters Co., Milford, MA). A Bio-Rad Aminex HPX-87P column (Bio-Rad Laboratories, Hercules, CA) was employed for separating the different sugars. The total xylose, glucose, galactose, arabinose, and mannose concentrations in the liquid fractions were measured after post-hydrolysis of each liquid sample with 4 wt% sulfuric acid at 121 °C for 1 h according to NREL Laboratory Analytical Procedure,[46-48] and concentrations of xylose oligomers in the liquid were calculated as the difference between the total xylose concentration after post hydrolysis and the monomeric xylose concentrations measured prior to post hydrolysis.

CHAPTER 3

DEPOLYMERIZATION OF LIGNOCELLULOSIC BIOMASS INTO FUEL PRECURSORS: MAXIMIZING CARBON EFFICIENCY BY COMBINING HYDROLYSIS WITH PYROLYSIS[1]

3.1 Introduction

The chief impediment to utilization of cellulosic biomass resources is overcoming the recalcitrant nature of the biomass[4]. The objective of this study is to study how hydrolysis and pyrolysis could be combined in an integrated biorefinery to help overcome this barrier. Cellulosic biomass is primarily composed of three polymeric components: cellulose, hemicellulose, and lignin [3]. Cellulose is a glucose polysaccharide whose long chains are arranged in a highly crystalline structure. Hemicelluloses are amorphous polysaccharides made up of 3 hexoses (galactose, glucose, and mannose), 2 pentoses (xylose and arabinose), and other compounds such as acetyl groups. Lignin is a complex network of different phenyl propane units (p-coumaryl alcohol, coniferyl alcohol, and sinapyl alcohol). All three of these biomass building blocks have different rates of depolymerization to release a complex mixture of sugars, degradation compounds, and other products, with the distribution depending on the reaction system applied.

We performed both fast pyrolysis and catalytic fast pyrolysis (CFP) on pure solid maple wood and solid maple wood samples after two different hydrolysis treatments. Thermochemical hydrolysis was employed in Stage 1 to remove most of the hemicellulose,

---

[1] The results in this chapter have been published in J.H. Jae, G.A. Tompsett, Y.C. Lin, T.R. Carlson, J.C. Shen, T.Y. Zhang, B. Yang, C.E. Wyman, W.C. Conner and G.W. Huber, Energy Environ. Sci. 2010, 3, 358-365.

while much of the remaining cellulose samples were removed in Stage 2 by enzymatic hydrolysis of the solids from Stage 1. We calculated material balances before and after each hydrolysis and pyrolysis treatment to track the fate of overall materials and carbon. The most efficient process will be the process that converts the highest percentage carbon of the biomass into usable fuel precursors.

3.2 Experimental

The experimental methods and materials used for this work are described in Sections 2.1, 2.4, and 2.12. The biomass feedstock used in these experiments was the red maple wood. The wood was ground to a small particle size (< 2mm) using a laboratory mill (model 4, Arthur H. Thomas Company, Philadelphia, PA) and an internal sieve. The composition (carbohydrates, lignin, and ash) of the raw maple wood was analyzed following NREL standard procedures, [46, 49-50] and the results are shown in Table 3.1. Prior to feeding to the reactor systems, the maple was stored in plastic bags in a freezer at -18^{o}C.

Table 3.1 Compositions of the red maple wood

	Klason lignin%	Glucan %	Xylan %	Arabinan %	Ash %	Moisture %
Maple	24.9 ± 0.2	41.9± 0.3	19.3± 0.1	0.81± 0.1	0.95±0.05	6.67±0.02

Zeolite used for catalytic fast pyrolysis experiments was a commercial ZSM-5 catalyst from WR Grace, with a silicon to aluminum ratio (Si/Al =15). The catalyst was calcined at 550˚C in air for 5 hours prior to the reaction.

3.3 Results

3.3.1 Hydrolysis of Biomass Feedstock

Pretreatment of biomass is needed to overcome the natural recalcitrance of the lignocellulosic biomass structure [51]. For example, use of just water, steam, or dilute acids will release sugars from hemicellulose. Pretreatment also alters the crystalline structure of cellulose and promotes access to enzymes for hydrolysis. In the present study, hot water alone was used to pretreat maple wood biomass and no other chemicals were added, thereby simplifying both pretreatment as well as the downstream neutralization and conditioning operations. The solid residues left after pretreatment were primarily comprised of cellulose and lignin as a result of the release of xylan, other sugars, and other compounds from hemicellulose into the liquid stream of the process. Then, cellulase and β-glucosidase enzymes could be applied to hydrolyze the cellulose in the remaining solids to glucose. The combination of the two steps, pretreatment and enzymatic hydrolysis, can provide high yields of sugars from hemicellulose and cellulose [52]. The residue obtained after pretreatment and enzymatic hydrolysis contains up to ~80wt% lignin.

It was determined that the optimal pretreatment conditions for maximum sugar recovery from maple wood was 200^{o}C and 10 minutes reaction time based on a series of experiments with raw maple using hot water at temperatures of 160^{o}C, 180^{o}C, and 220^{o}C and treatment times between 5 and 40 minutes. A high enzyme loading (60 FPU/ g total glucan plus xylan) was used in the enzymatic hydrolysis at known optimal digestion conditions of 50^{o}C and pH 4.8, to remove the glucan from the pretreated maple wood. The mass balances of each stream from pretreatment and enzymatic hydrolysis of maple wood are shown in Figure 3.1. The mass balances are adjusted to a basis of 100 kg of total maple feed (note: the glucan and xylan in the solid in Figure 3.1 have been converted into glucose and xylose with conversion factors of 0.90 and 0.88, respectively). Thus, 100 kg of maple wood would produce 17.54 kg of total xylose (mono-xylose plus xylo-oligomer, 17.54 kg/m^3 of total xylose concentration in stream 2), 0.96 kg total glucose (mono-glucose plus gluco-oligomer, 0.96 kg/m^3 of total glucose concentration in stream 2), and 68.9 kg of residual solid from the pretreatment step (stage one). The corresponding theoretical glucose and xylose yields expressed as a percent of the maximum amount that could be obtained from maple were 2.1% and 80.1%, respectively, in pretreatment.

It should be noted that we were not able to account for 12.6 kg of the solid biomass lost in water only pretreatment, and 17.42kg of the solid biomass lost in the combined pretreatment and enzymatic hydrolysis, which resulted in 5.9% and 11.8% deviations in the glucan and xylan closure calculations. These deviations might result from 3 factors. First, the solid particles could be lost in the suspension after hot water pretreatment because the filter paper used could not capture the finer particles in suspension after hot water pretreatment. Second, not all of the solid could be recovered after filtration as some solids were adsorbed in the filter paper and funnel wall of filtration. Third, some components of hemicellulose and cellulose were likely degraded into unknown compounds that could not be identified by HPLC. After pretreatment of 100 kg of maple wood in stage 1, enzymatic hydrolysis (stage 2) would produce 40.3 kg of glucose (11.7 kg/m^3 of glucose concentration) and 1.08 kg of xylose (0.32 kg/m^3 of xylose concentration) in the liquid stream 4, and 22.7 kg of solid, containing mostly lignin, in Stream 5, again as shown in Figure 3.1. The corresponding glucose and xylose yields as a percent of the theoretical maximum possible based on the composition of raw maple for the combined operations of pretreatment and enzymatic hydrolysis were 88.7% and 85.0%, respectively. In this second step only 4.82 kg of the original 100 kg of solid maple wood could not be accounted for as a result of the high selectivity of enzymes.

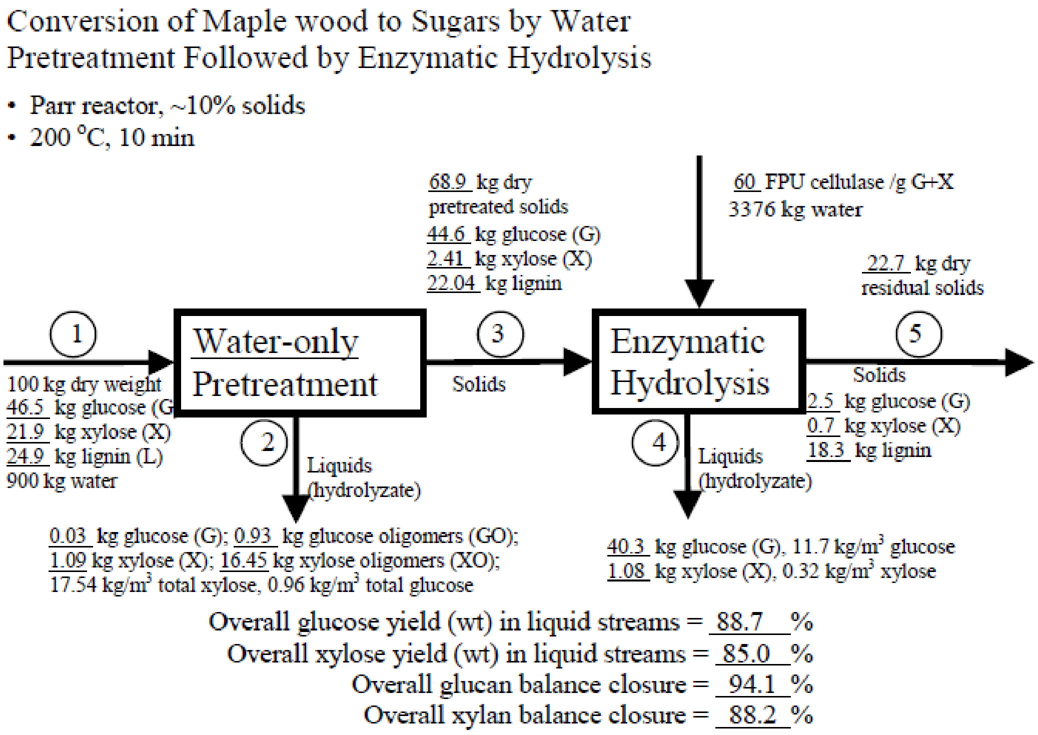

Figure 3.1 Mass balance of hydrolysis of maple wood with water pretreatment and enzymatic hydrolysis adjusted to a basis of 100 kg of dry maple wood feed.

3.3.2 Pyrolysis of Biomass Samples : TGA results

The pyrolysis characteristics, both thermogravimetric (TG, in wt.%) and differential thermogravimetric (DTG, in wt.%/˚C) curves of the raw maple wood, hemicellulose removed maple wood, and lignin residue are shown in Figure 3.2. We were able to volatilize over 95 wt% of both the raw maple wood and the maple wood after hemicelluloses extraction. However, we were only able to volatilize 70 wt% of the lignin residue. This indicates that the lignin residue most likely undergoes repolymerization reactions during the hydrolysis steps. These repolymerization reactions make it harder to volatilize the raw lignin forming “hard coke”.

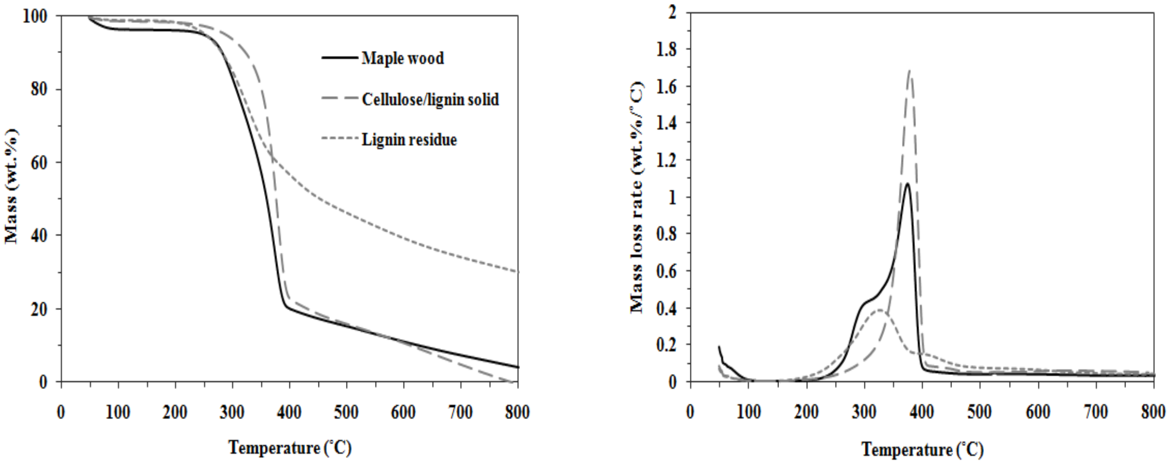

Figure 3.2 TGA and DTG curves of raw maple wood (black), solid residue after hemicellulose extraction (Cellulose/lignin solid, red), and solid residue after hemicellulose and cellulose extraction (Lignin residue, blue) with heating rate of 15˚C/min from 50˚C to 800˚C.

From the DTG curves, it can be seen that the maple wood undergoes decomposition processes at several different temperatures. The maple wood first starts to decompose at a temperature of 250-300^{o}C. Once the hemicelluloses fraction is removed from the maple wood this low temperature peak is no longer present. This indicates that this low temperature peak from 250-300^{o}C is most likely from the hemicelluloses fraction of the biomass. It has been reported that DTG peaks for hemicelluose and cellulose occur at around 268˚C and 355˚C, respectively [53]. The majority of the maple wood and the hemicelluloses removed maple wood sample decomposes at a temperature range from 300-400^{o}C. Pure cellulose decomposes in this same temperature range [54]. This peak in the

300-400˚C range is due to cellulose pyrolysis. This is the largest peak and most abundant species present in the maple wood.

The solid lignin residue shows three major temperature regimes for pyrolysis including: a first peak from 250-350^{o}C, a second peak from 350-450^{o}C, and a broad peak from 350- 800^{o}C. About 40 wt% of the lignin decomposes in this first temperature regime from 250-350^{o}C. The lignin residue only contains 10 wt% sugars so this first temperature peak has to contain lignin compounds. These results suggest that the lignin residue contains at least three different structures that decompose at significantly different temperature. This is consistent with results which indicate that lignin has no specific structure and is formed from free radical polymerization reactions. [3] This also indicates that it is difficult to convert the lignin residue into fuels or chemicals because it does not have a well-defined structure. Based on the results presented in Figure 3.2 this lignin structure most likely undergoes changes during the hydrolysis processing of the biomass.

3.3.3 Pyrolysis of Biomass Samples: Pyroprobe Results

Table 3.2 shows the weight and carbon yield of gases, bio-oil, and char from the pyrolysis of biomass fractions at 600°C for 4 min with heating rate of 1000˚C/s in the pyroprobe reactor. Pyrolysis in the pyroprobe reactor typically produces more coke than pyrolysis in the TGA system. This is because higher concentrations of vapors are present in the pyroprobe reactor. On a weight yield basis, the yield of condensable liquids or bio-oil is around 67 wt% for both maple wood and cellulose/lignin solid. For the lignin residue the yield of the bio-oil is only 45 wt%. All three samples have similar gas yields of 20-23 wt%. However, the lignin residue produces significantly higher amounts of coke than the other two samples. These results are consistent with the TGA results. The amount of bio-oil produced is known to be a function of the reactor, reaction conditions, and feedstock [11, 55-56]. It has been reported that fast pyrolysis processes of woody biomass typically produce yields of 60-75 wt % of liquid bio-oil [57-58]. This indicates that the yields obtained from our pyroprobe reactor are similar to yields in other types of fast pyrolysis reactors. Also in Table 3.2 we report the carbon yields of the various products. The estimated carbon contents of the bio-oils were 45 wt% for maple wood, 48 wt% for cellulose/lignin solid and 53 wt% for the lignin residue. We have higher CO and CO_2 yields than have been obtained in a fluidized sand bed reactor [11, 57]. Piskorz and Scott reported that 4.83 wt% yield of CO and 5.36 wt% yield of CO_2 were obtained from red maple wood pyrolysis with 67.3 wt% yield of bio-oil at reaction temperature 530˚C. We produced 9.9 and 13.4 wt% yield of CO and CO_2 from maple wood. The difference in the CO and CO_2 yield is probably due to the longer vapor residence time in the pyroprobe reactor. It is known that long vapor residence times cause secondary cracking of primary products and favors gaseous products [59-60].

Table 3.2 Pyrolysis yields for maple wood, hemicelluloses removed maple wood, and lignin residue in the pyroprobe reactor. Reaction conditions: nominal heating rate 1000℃ s^{-1}, final reaction temperature 600 ℃, and reaction time 240 s.

Pyrolysis products	Maple Wood		Cellulose/lignin solid		Lignin residue	
	Wt%	Carbon%	Wt%	Carbon%	Wt%	Carbon %
CO	9.9	9.3	11.8	10.4	7.0	7.5
CO_2	13.4	8.0	11.8	6.6	13.8	9.4
Bio-oil*	66.7	65.6	66.6	65.6	44.8	58.8
Char	10.0	4.5	9.8	1.8	34.4	19.5
Unidentified	-	12.6	-	15.6	-	4.7

* Bio-oils carbon content: 45 wt% for bio-oils from maple wood, 48 wt% for bio-oils from cellulose/lignin solid, and 53 wt% for bio-oils from lignin residue. Unidentified fraction includes missing carbon.

We attempted to identify the products present in the bio-oil samples. Table 3.3 shows the detailed chemical composition of the bio-oils from the three biomass samples. We were able to identify approximately 20% of the carbon present in these various samples. It should be noted that almost 80% of the carbon in bio-oils were unidentified fractions of the bio-oils which include unidentified peaks in the GC-MS and high molecular weight species (nonvolatile compounds). In fact, bio-oil is a complex liquid composed of over 400 compounds including char particles. However, this analysis shows a clear distinction between the composition of products from the three feedstocks.

The identified chemical species in bio-oils can be classified into the following 4 categories:

(1) retro-aldol species (acetic acid, d-glyceraldehyde, hydroxyacetone, and hydroxyacetaldehyde),

(2) furfural,

(3) Sugars and anhyhdrosugars (primarily levoglucosan)

(4) phenolic compounds (catechol, guaiacol, syringol, isoeugenol, and other methoxy benzene compounds).

The major species of bio-oil from maple wood are retro-aldol species and levoglucosan while bio-oil from cellulose/lignin solid showed primarily levoglucosan rather than retro-aldol species. The bio-oil from lignin residue mainly consists of phenolic compounds, as expected.

Table 3.3 Carbon molar percentage (%) of products present in the bio-oils.

Compound	Formula	Maple wood	Cellulose/lignin solid	Lignin residue
acetic acid	$C_2H_4O_2$	7.5	2.0	2.1
hydroxy acetaldehyde	$C_2H_4O_2$	1.2	0.7	0.3
hydroxy-acetone	$C_3H_6O_2$	1.8	-	-
d-glyceraldehyde	$C_3H_6O_3$	7.6	1.7	-
Furfural	$C_5H_4O_2$	0.3	0.5	0.2
Catechol	$C_6H_6O_2$	0.3	-	0.5
Guaiacol	$C_7H_8O_2$	-	0.3	3.5
3-methoxy-1,2-benzenediol	$C_7H_8O_3$	-	-	1.1
4-methyl guaiacol	$C_8H_{10}O_2$	-	0.5	1.2
syringol	$C_8H_{10}O_3$	0.8	0.7	6.6
2-methoxy-4-vinylphenol	$C_9H_{10}O_2$	-	-	1.9
1,2,4-trimethoxy benznene	$C_9H_{10}O_3$	0.7	1.6	2.0
isoeugenol	$C_{10}H_{10}O_2$	0.6	-	1.3
6-Methoxyeugenol	$C_{11}H_{14}O_3$	1.1	-	0.8
Levoglucosan	$C_6H_{10}O_5$	1.6	9.0	-
Unidentified fraction*		76.4	83.1	78.7

All numbers are in molar carbon yield %.
*include unidentified organic carbon

3.3.4 Catalytic Fast Pyrolysis of Biomass Samples: Pyroprobe Results

Table 3.4 shows the weight and carbon yields of gases, aromatics, and coke from catalytic fast pyrolysis of the three solid biomass samples. The same reaction conditions as used in pyrolysis were employed, namely at 600°C for 4 min with heating rate of 1000˚C/s. Aromatic carbon yields of 37.9% and 31.5% were achieved from raw maple wood and the cellulose/lignin solid, respectively while only 23.2% carbon was produced from the lignin residues. Lignin produced the highest amount of coke (~58.8 % carbon). The yields of gases were high in all the samples (18.2-39.6 wt %). In CFP, the oxygen in the biomass is removed by dehydration, decarbonylation and decarboxylation reactions to produce the aromatic hydrocarbon products. The overall reaction converts the biomass into a mixture of aromatics, CO, CO_2 and water.

Table 3.4 Carbon yields for catalytic fast pyrolysis of maple wood, hemicelluloses-extracted maple wood, and lignin residue. Reaction conditions: ZSM-5 catalyst, nominal heating rate 1000℃ s^{-1}, final reaction temperature 600 ℃, catalyst to biomass ratio 19, and reaction time 240 s.

	Maple wood		Cellulose/lignin solid		Lignin residue	
	Wt%	Carbon %	Wt%	Carbon %	Wt%	Carbon %
CO	32.4	30.3	27.6	24.3	11.7	12.5
CO_2	15.6	9.3	11.9	6.6	8.3	5.7
Aromatics	18.8	37.9	16.6	31.5	10.1	23.2
Coke[a]+H_2O	33.2	23.1	44.0	37.6	69.9	58.8

[a] Coke is the amorphous carbon produced from either homogeneous gas phase thermal decomposition reaction or heterogeneous reaction on the catalyst.

Figure 3.3 shows the aromatic selectivities on a molar carbon basis for CFP of the three solid samples. The aromatic distributions are similar to each other regardless of the feedstock. The major aromatic species were naphthalene >> xylene > toluene > benzene.

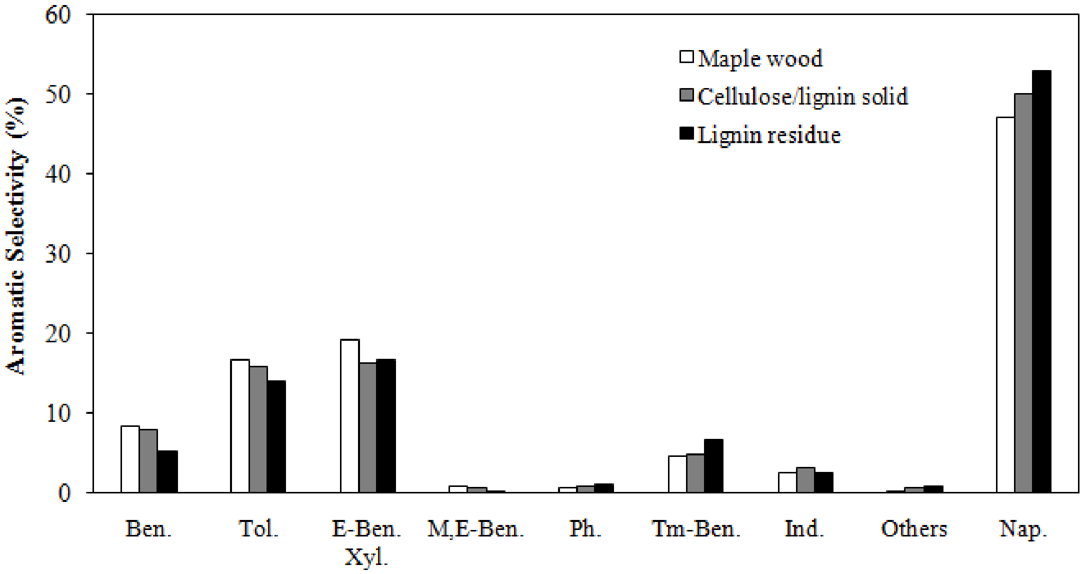

Figure 3.3 Aromatic selectivities from CFP of maple wood, cellulose/lignin solid, and lignin residue. Key- Maple wood (white), Cellulose/lignin solid (grey) and Lignin residue (black). Aromtics quantified include: Ben. benzene, Tol. toluene, E-Ben., Xyl. xylenes, ethyl-benzene, M,E-Ben. methyl-ethyl-benzene, Ph. Phenols, Tm-Ben. trimethylbenzene, Ind. indanes, Nap. naphthalenes. Others include ethyl-dimethyl-benzene and tetramethylbenzene.

3.4 Discussion

As shown in Figure 3.4, there are three potential options for combining pyrolysis with hydrolysis to deconstruct biomass. Option 1 is the pyrolysis/CFP of dried maple wood biomass, with the products including: (1) a bio-oil or an aromatics stream, (2) a solid char stream, and (3) a gaseous stream containing CO and CO_2. Option 2 first applies thermal hydrolysis to extract hemicellulose followed by pyrolysis/CFP of the cellulose/lignin rich solid left after hemicellulose hydrolysis. The products for option 2 include similar products to Option 1 plus an aqueous hemicellulose sugar stream rich in C5 sugars and C5 sugar oligomers, plus acetic acid and a small amount of C6 sugars. Option 3 applies thermal hydrolysis of hemicelluose followed by enzymatic removal of most of the cellulose and remaining hemicellulse and then pyrolysis/CFP of the lignin residue. The products from Option 3 are thus similar to the products from Option 2 plus an additional aqueous glucose stream.

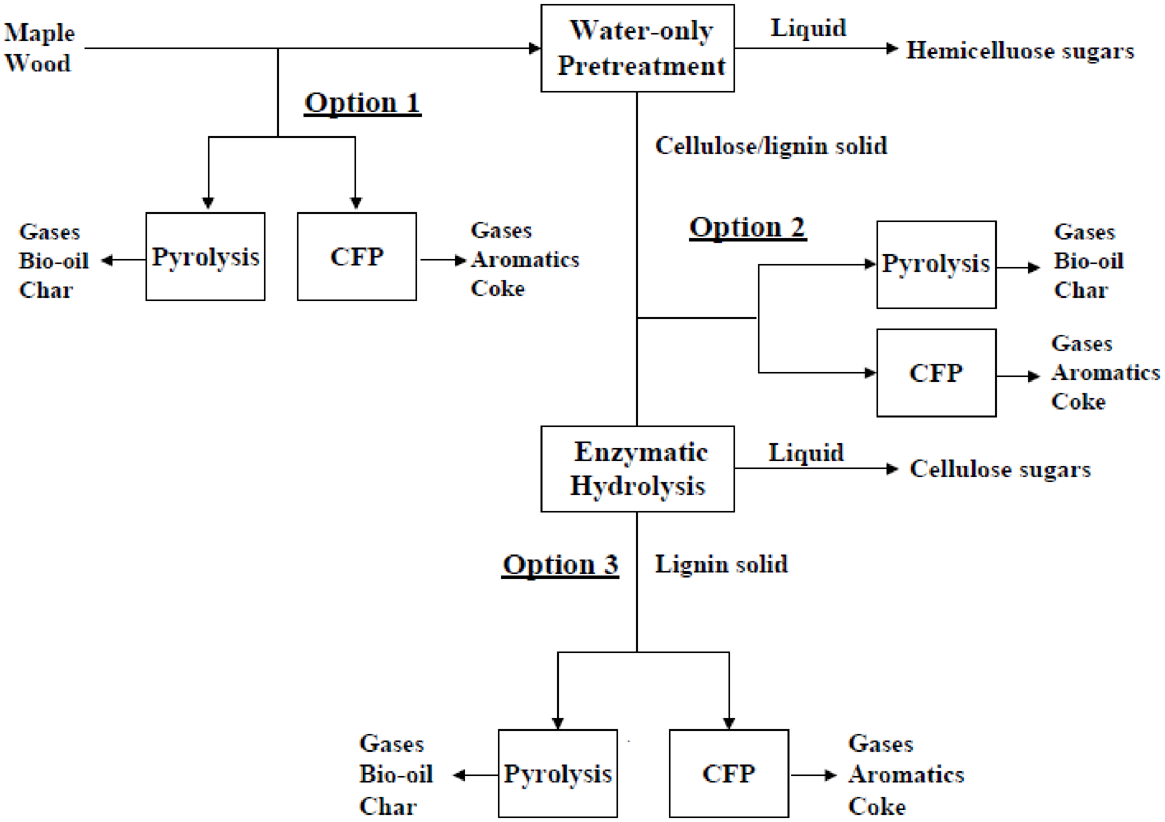

Figure 3.4 Integrated process scheme by combining hydrolysis with pyrolysis, including three main routes

As expected, the amount of bio-oil produced decreased as the number of hydrolysis steps increased. Option 3 produced the largest amount of aqueous sugars, and Option 1 did not produce any sugars. It should be noted that the conversion of sugars into fuels by fermentation is already commercially established, whereas technologies for bio-oil conversion into transportation fuels are not yet commercially available [61]. These bio-oil conversion technologies however are moving towards commercial application.

The ideal process will decompose the maximum amount of biomass to products that can be easily upgraded by fermentation,[62-64] aqueous phase processing,[6, 65-66] hydrodeoxygenation,[67] or standard petroleum conversion technologies,[61, 68] with preservation of the energy content of the feedstock most critical when fuels are desired. We calculated mass and carbon balances as well as the products obtained for each option as shown in Table 3.5, with the overall mass and carbon efficiencies assuming that sugars, bio-oil and aromatics are useful products that can easily be upgraded. Char and gases are less valuable products because they are more expensive to convert into fuels and chemicals.

Option 1, 2 and 3 all have similar overall carbon yields of between 66-70%. Thus, 66-70% of the carbon of the biomass was converted into products that are easily upgraded. The energy in the products from these three options ranges from 1209 to 1323 MJ per 100 kg of maple wood. Thus, combining hydrolysis with pyrolysis does not produce significantly more usable carbon than pyrolysis alone, for this feedstock. The different options do however produce significantly different reaction intermediates. Therefore, the choice of technology for biomass deconstruction will likely depend on the options available for upgrading these intermediates to products, the capital and operating costs of the overall biomass refining operations, and market preferences.

Combing CFP with hydrolysis produces more sugars and less aromatics as shown in Table 3.5. The carbon yield decreased from 65.6 to 37.9 % for pyrolysis and CFP of pure maple wood (Option 1 in Table 3.5), and the carbon yield decreased for all three options using CFP rather than pyrolysis of the biomass. However, the advantage of CFP is in producing a product that can fit into the existing infrastructure which does not require any further upgrading. The overall energy output however for CFP is half that of pyrolysis, and less aromatics are produced by CFP after hydrolysis of the biomass. However, combining CFP with hydrolysis allows for the production of sugars along with aromatics, and in this study we show that CFP is effective for lignin conversion, with the result that CFP can be combined with fermentation technologies to utilize a waste stream to produce aromatics.

As shown in this study, many options are possible for biomass deconstruction, and many more can be added on for conversion of the intermediates produced into fuels and chemicals. Although we have provided material balances for maple wood deconstruction to reactive intermediates, more research in the areas of both homogeneous and heterogeneous catalysis combined with process design is needed to optimize the different pathways for converting these intermediates to products and integrate production of the intermediates with downstream operations.

Table 3.5 Mass and carbon balances for the three options of combining hydrolysis with pyrolysis

	Option 1		Option 2		Option 3	
	Wt%	Carbon%	Wt%	Carbon%	Wt%	Carbon%
Hydrolysis						
Glucose			0.04	0.03	42.34	37.0
Xylose			3.08	2.69	6.05	5.29
Glucose oligomer			1.1	1.06	1.1	1.06
Xylose oligomer			15.05	14.48	15.05	14.48
Pyrolysis						
Bio-oil	66.7	65.6	45.9	48.2	10.2	11.7
Gases	23.3	17.3	16.3	12.5	4.7	3.3
Char	10	4.5	6.8	1.3	7.8	3.9
CFP						
Aromatics	18.8	37.9	11.4	23.1	2.3	4.6
Gases	48.0	39.7	27.1	22.7	4.5	3.6
Coke	33.2	23.1	30.3	27.6	15.9	11.6
Overall mass and carbon Balances						
Pyrolysis+Hydrolysis (Sugar+Bio-oil)	66.7	65.6	65.2	66.4	74.7	69.5
CFP+Hydrolysis (Sugar+Aromatics)	18.8	37.9	30.7	41.4	66.8	62.4
Energy output						
Pyrolysis+ Hydrolysis (MJ/100 kg of maple wood)	1267		1209		1323	
CFP+ Hydrolsysis (MJ/100 kg of maple wood)	620		715		1205	

*Energy output calculation based on higher heating value
Glucose and xylose : 17.5 MJ/kg, bio-oil : 19MJ/kg, and aromatics : 33MJ/kg

3.5 Conclusions

The first step in any biomass refinery is the deconstruction of the solid biomass to reactive intermediates, with hydrolysis and pyrolysis providing two options, and in this study, we developed material balances for application of these two operations to maple wood to release intermediates that can be used for production of fuels and chemicals.

Material and carbon balances were developed for three possible options for integration of hydrolysis with pyrolysis: Option 1 was the pyrolysis/CFP of raw maple wood, Option 2 was to combine hemicellulose extraction by hydrolysis with pyrolysis/CFP of hemicelluose extracted maple wood, and Option 3 combined two step hydrolysis for hemicelluloses and cellulose sugars extraction with pyrolysis/CFP of the lignin residue. Pyrolysis of maple wood produced 67 wt% of condensable liquid products (or bio-oils). The bio-oil produced was a mixture of compounds including sugars, water, phenolics, aldehydes, and acids. Pyrolysis of hemicelluose extracted maple wood (the solid product after pretreatment of maple wood) showed a similar bio-oil yield and composition to the raw maple wood while the pyrolysis of lignin residue (the final solid product of enzymatic hydrolysis) produced only 44.8 wt% of bio-oil. The bio-oil from the lignin residue was mostly composed of phenolic compounds. Catalytic fast pyrolysis (CFP) of maple wood, hemicelluloses extracted maple wood, and lignin residue produced 18.8, 16.6 and 10.1 wt% aromatic products. Two step hydrolysis of maple wood through pretreatment and enzymatic hydrolysis, achieved a 93.4 wt% yield of glucose and 96.3 wt% yield of xylose in the liquid stream from the combined streams. The residue obtained after hydrolysis was 80 wt% lignin. Thus, Options 1, 2, and 3 all were shown to have similar overall carbon yields for sugars and bio-oils of between 66 and 70%, implying that combining hydrolysis with pyrolysis does not produce significantly more useable carbon than pyrolysis alone. However, it should be noted that conversion of sugars to fuels by fermentation processes is already commercial whereas bio-oil upgrading process is still in development. CFP showed a lower carbon yield than pyrolysis in all three options, but CFP produces aromatics that can be directly used for gasoline or chemicals. Further advances in homogeneous and heterogeneous catalysis combined with process design and process integration are expected to offer economical pathways for biomass conversion into fuels and chemicals.

CHAPTER 4

CHEMISTRY OF CATALYTIC FAST PYROLYSIS OF GLUCOSE[2]

4.1 Introduction

The chief challenge with CFP of biomass is controlling the complicated homogeneous and heterogeneous chemistry. The objective of this study is to elucidate the combined homogeneous and heterogeneous reaction mechanism that occurs during catalytic fast pyrolysis of glucose with HZSM-5. We have chosen glucose as a cellulose model compound. The pyrolytic behavior of glucose is known to be different from that of cellulose. Pyrolysis of glucose yields a higher amount of furans (such as furfural and 5-hydroxy-methylfurfural) and lower percentage of levoglucosan than that of cellulose[69]. The difference of reactivity between cellulose and glucose could be due to the fact that cellulose has the fixed polymer chains whereas glucose has acylic of open ring forms[69]. However, catalytic fast pyrolysis of cellulose and glucose shows similar product yield and selectivity [25], suggesting that both glucose and cellulose decomposed to common intermediates. Therefore the mechanistic conclusions from this study could be applicable to cellulosic type feedstocks.

In this study, we will propose the overall reaction pathway for the conversion of glucose to aromatics. The initial thermal decomposition of pure glucose and glucose in the presence of ZSM-5 will be studied with TG/DTG, ex situ FTIR and visual observation.

---

[2] The results in this chapter have been published in T.R. Carlson, J. Jae, Y.C. Lin, G.A. Tompsett and G.W. Huber, *J. Catal.* **2010**, *270*, 110-124; T.R. Carlson, J. Jae and G.W. Huber, *ChemCatChem* **2009**, *1*, 107-110.

The pyroprobe reactor will be used to study how product yield and selectivity changes with different reaction conditions. We will study the evolution of coked samples as a function of time and temperature with FTIR to determine which species are involved in the undesired coke formation reactions. The mechanism for aromatic formation will be studied in detail by performing isotopic labeling experiments with ^{13}C glucose feed and conversion of intermediates in the pyroprobe GC/MS system. Furthermore, nitrogen adsorption will be used to determine whether these undesired reactions occur on the surface or within the pores of the catalyst. This study will provide us for insight into how we might control zeolite chemistry for the conversion of biomass into aromatics.

4.2 Experimental

The experimental methods and materials used for this work are described in Sections 2.1, 2.4, 2.6, and 2.11. Zeolite used for catalytic fast pyrolysis experiments was a commercial ZSM-5 catalyst from Zeolyst International, with a silicon to aluminum ratio (Si/Al =15). The catalyst was calcined at 550˚C in air for 5 hours prior to the reaction.

4.3 Results

4.3.1 Thermal Decomposition of Glucose

4.3.1.1 Pyroprobe Results

Figure 4.1 shows the detailed quantification of glucose pyrolysis with 1000, 2.5, and 0.25 ℃ s^{-1} heating rates carried out with the in-house designed trap. The dehydration product levoglucosan (LGA, 1,6-anhydro-β-D-glucopyranose, $C_6H_{10}O_5$) was found to be the most abundant product. Other anhydrosugars such as; levoglucosanone (LGO, 6,8-dioxabicyclo[3.2.1]oct-2-en-4-one, $C_6H_6O_3$), 1,4:3,6-dianhydro-β-D-glucopyranose (DGP, $C_6H_8O_4$), and 1,6-anhydro-β-d-glucofuranose (AGF, $C_6H_{10}O_5$) were present in lower amounts. Products that are likely formed from the retro-aldol condensation of glucose such as d-glyceraldehyde, hydroxyacetone and hydroxyacetaldehyde were also observed. The selectivity for coke ranges from 30 to 40 carbon %. As the pyrolysis rate increases the LGA yield increases while the coke yield is suppressed. A lower heating rate increases the amount of dehydration reactions, with greater DGP, LGO, and coke.

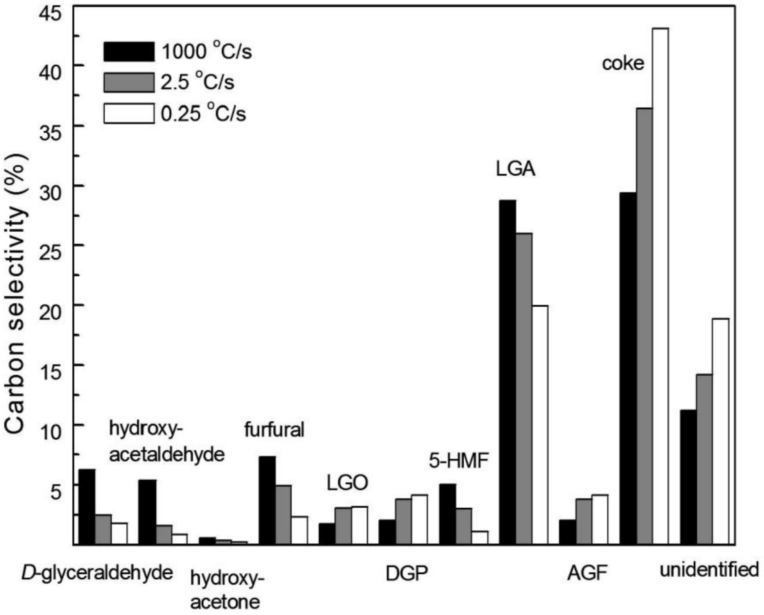

Figure 4.1 Product distribution pattern of glucose pyrolysis in a pyroprobe reactor with 1000, 2.5, and 0.25°C s^{-1} heating rates; final temperature at 600 °C with reaction time for 240 seconds.

4.3.1.2 Themogravimetric Analysis with Mass Spectrometry (TGA-MS)

Table 4.1 summarizes the approximate and elemental analysis of glucose pyrolysis products after a 2.5 °C s^{-1} heating rate. Around 89 wt% of glucose can be volatilized, with 11% of fixed carbon and trace ash. Water, CO, and CO_2 are the major species identified by the TGA-MS. The CO and CO_2 are formed from degradation of the primary pyrolysis products (e.g. levoglucosan, hydroxyacetaldehyde), which occurs in the line leading from the TGA to the MS. Only small amounts of these primary pyrolysis products are observed in our TGA-MS system. These primary pyrolysis products can only be observed if they are quickly condensed out, as with the liquid nitrogen trap in Section 4.3.1.1.

Table 4.1 Proximate and elemental analysis of glucose pyrolysis.

Proximate analysis (wt%)			Elemental analysis (wt%)		
Volatile	Fixed C.	Ash	C	H	O[a]
89.0	10.9	0.1	42.9	6.5	50.6

[a] By balance.

Figure 4.2 (a) shows the DTG of pure glucose pyrolysis with 0.017, 0.25, and 2.5 ℃ s^{-1} heating rates. Glucose pyrolysis initiates at 150, 200, and 250 ^oC, respectively. The DTG curves of all pyrolysis rates are composed of two major peaks. For a heating rate of 0.017 ℃ s^{-1} the peaks are located at 198 and 290 ^oC, with almost equivalent intensity of the two peaks. For 0.25 ℃ s^{-1}, the first peak is at 228 ^oC; the second, 312^oC. For 2.5 ℃ s^{-1}, the first peak is at 282 ^oC; the second, 369 ^oC. The intensity of the first DTG peak diminishes as the heating rate is increased. Figure 4.2 (b) shows the corresponded MS responses at a 2.5 ^oC s^{-1} heating rate. The ion fragments, including hydrogen (*m/z*=2), methane (*m/z*=16), water (*m/z*=18), carbon monoxide/ethylene (*m/z*=28) and carbon dioxide (*m/z*=44) were recorded with time. From the 28 m/z and 44 m/z signals it is seen that decarboxylation and water removal begins around 200 ^oC while decarbonylation, methane production and hydrogen production do not initiate until above 250 ^oC. Water is removed during two separate reactions the first taking place at ~300 ^oC and the second at ~410 ^oC. The water MS signal corresponds to the two separate DTG peaks indicating both of these reactions involve the removal of water. In Figure 4.2 (c), the DTG curves for the pyrolysis of glucose with ZSM-5 (19:1 catalyst to glucose wt. ratio) are shown. The DTG responses for different heating rates show similar peaks to the non-catalyzed pyrolysis, however, the two peaks shift to lower temperature. For the heating rates of 0.017, 0.25, and 2.5 $^{o}C\ s^{-1}$ the first DTG peak shifts to 154, 171, and 206 ^{o}C, respectively. The second DTG peaks also shift downward to 275, 282, and 312 ^{o}C for the 0.017, 0.25, and 2.5 $^{o}C\ s^{-1}$ heating rates, respectively. When glucose was pyrolized in the presence of ZSM-5 a third peak appears. This new peak is located at 327, 363, and 402 ^{o}C for the 0.017, 0.25, and 2.5 $^{o}C\ s^{-1}$ heating rates, respectively. In Figure 4.2 (d), the MS responses for the pyrolysis of glucose with ZSM-5 at a heating rate of 2.5 $^{o}C\ s^{-1}$ are shown. Compared to pure glucose pyrolysis, the MS signals initiate at a lower temperature (m/z=28 at 50 ^{o}C; m/z=18 at 100 ^{o}C). At around 350 ^{o}C, where the newly formed third DTG peak is located, m/z=78 (benzene) and m/z=91 (toluene) signals are observed. The response of m/z=28 shows a second peak around the same temperature. The second m/z=28 peak is most likely from ethylene. It is well documented in the literature for the methanol to hydrocarbons process with ZSM-5 catalyst that ethylene is formed concurrently with benzene and toluene [70]. Comparing both trials, almost all the MS ions in Figure 4.2 (d) show significant higher responses and greater areas in the MS peaks than those in Figure 4.2 (b), except m/z=16 (methane). This is because for pyrolysis without catalyst, the major products are oxygenates that are not shown in the MS response. For pyrolysis with catalyst, the oxygenates are converted to water, CO, CO_2, and aromatics. These product ions are shown in the MS response, which leads to an increase in the total ions measured.

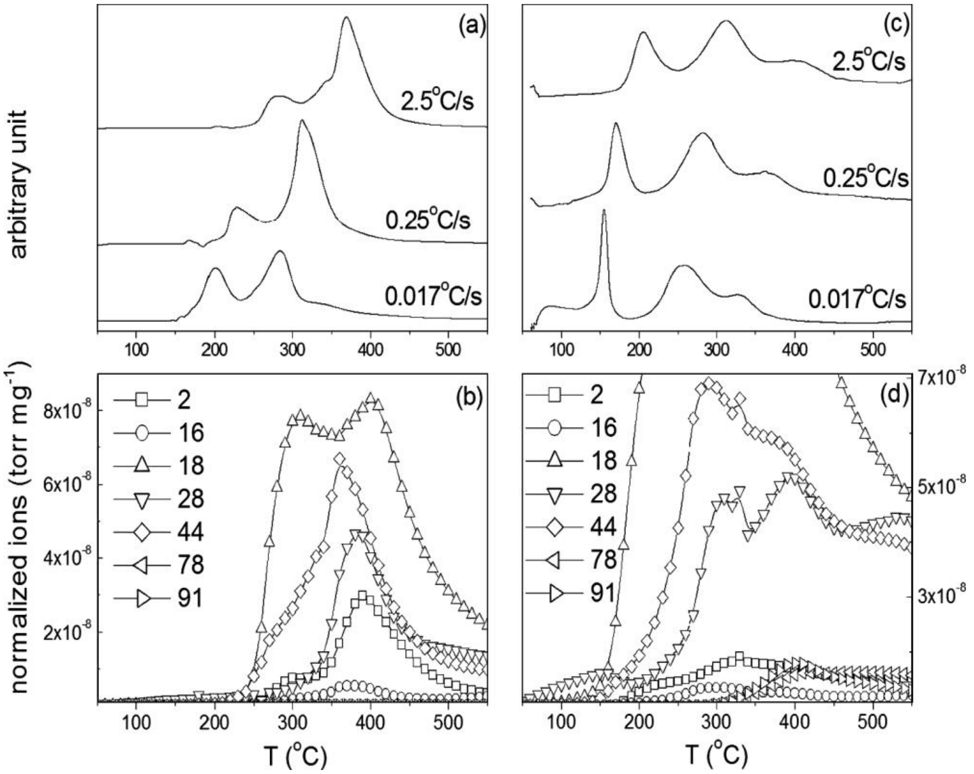

Figure 4.2 (a) DTG signals of glucose pyrolysis; (b) MS responses of selected ions of glucose pyrolysis at a 2.5 ^{o}C s^{-1} heating rate; (c) DTG signals of glucose pyrolysis with ZSM-5; (d) MS responses of selected ions of glucose pyrolysis with ZSM-5 at a 2.5 ^{o}C s^{-1} heating rate.

The two separate peaks in the DTG response for glucose pyrolysis imply two separate decomposition reactions. To identify the species that are present for each peak separate pyrolysis runs were carried out using identical reaction conditions, however, the temperature ramp was stopped at the onset of the peak of interest. At this designated temperature the reaction was rapidly quenched by cooling the furnace to room temperature with flowing air. The quenched reaction residue was then quantitatively dissolved in methanol and analyzed by GC/MS. For low-temperature products, the final temperatures were 180, 200 and 250 ^{o}C for the 0.017, 0.25 and 2.5 ^{o}C s^{-1} heating rate runs, respectively. At these temperatures, the residues of all samples are ~98% of the initial sample mass. Figure 4.3 shows the distribution of the species within the methanol-dissolved residue for the three different heating rates. The primary products observed for the low temperature peak were hydroxyl-acetaldehyde, hydroxyl acetone, and dihydroxyacetone. These products are likely from retro-aldol and Grob fragmentation of glucose [71-72]. As shown in Figure 4.3, the unidentified carbon is quite high for the lowest heating rate (2.5 °C s^{-1}). This missing carbon could be attributed to other reactions other than retro-aldol and Grob fragmentation. For the high-temperature peak, the final temperatures were 280, 300 and 380 °C for the 0.017, 0.25 and 2.5 °C s^{-1} heating rate runs, respectively. At these temperatures only non-dissolvable coke and tar remained in the crucible.

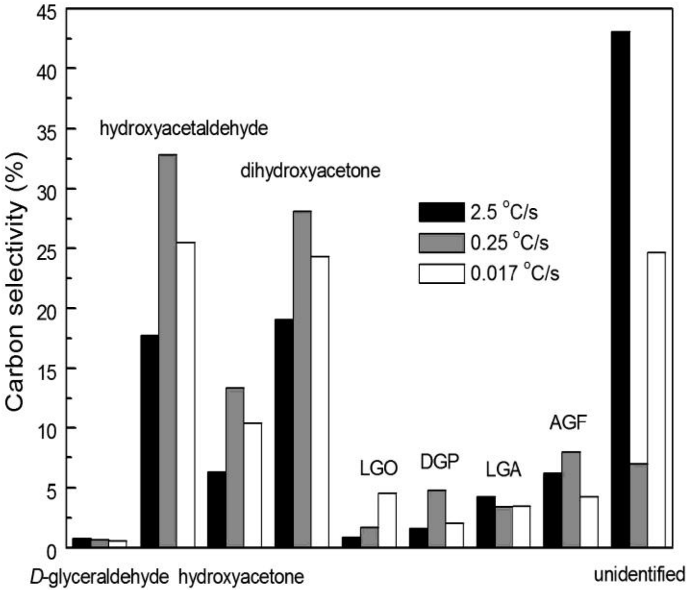

Figure 4.3 Carbon yields of glucose pyrolysis with three pyrolysis rates, final temperatures at 180 (0.017°C s^{-1}), 200 (0.25°C s^{-1}), and 250°C (2.5 °C s^{-1}), respectively.

4.3.1.3 Visual Observations

To provide a clear view of glucose fast pyrolysis and catalytic fast pyrolysis, a series of snapshots of these experiments are shown in Figure 4.4. Both trials were carried out in the pyrex trap with a 1000 °C s^{-1} heating rate and final temperature at 600 °C. The pyrex vial was set on the bench top and filmed with a video camera at room temperature. Figure 4.4 shows the solid pure glucose (a) and glucose-ZSM-5 mixture (e) at room temperature before reaction. Figure 4.4 (b) and (f) show snapshots at ~ 210 ^{o}C during pyrolysis of the glucose and glucose-ZSM-5 mixture, respectively. At 210 ^{o}C glucose transforms into a transparent liquid phase because such a pyrolysis temperature surpasses the boiling point (~145 ^{o}C) [73]. As seen in Figure 4.4 (f) at 210 ^{o}C black spots (coke) were clearly visible. At this same temperature no coke was observed when the catalyst is not present during pyrolysis. This indicates that coke forms at a lower temperature when catalysts are present. At a temperature of 600 ^{o}C (Figure 4.4 (c) and (g)), vapors can be seen coming from the ends of the quartz tube. At 600 ^{o}C the coke formation becomes more severe for the glucose/ ZSM-5 sample (Figure 4.4 (g)). After 5 seconds at the final temperature the residual of glucose inside the reactor turns into coke for both cases in (Figure 4.4 (d) and (h)).

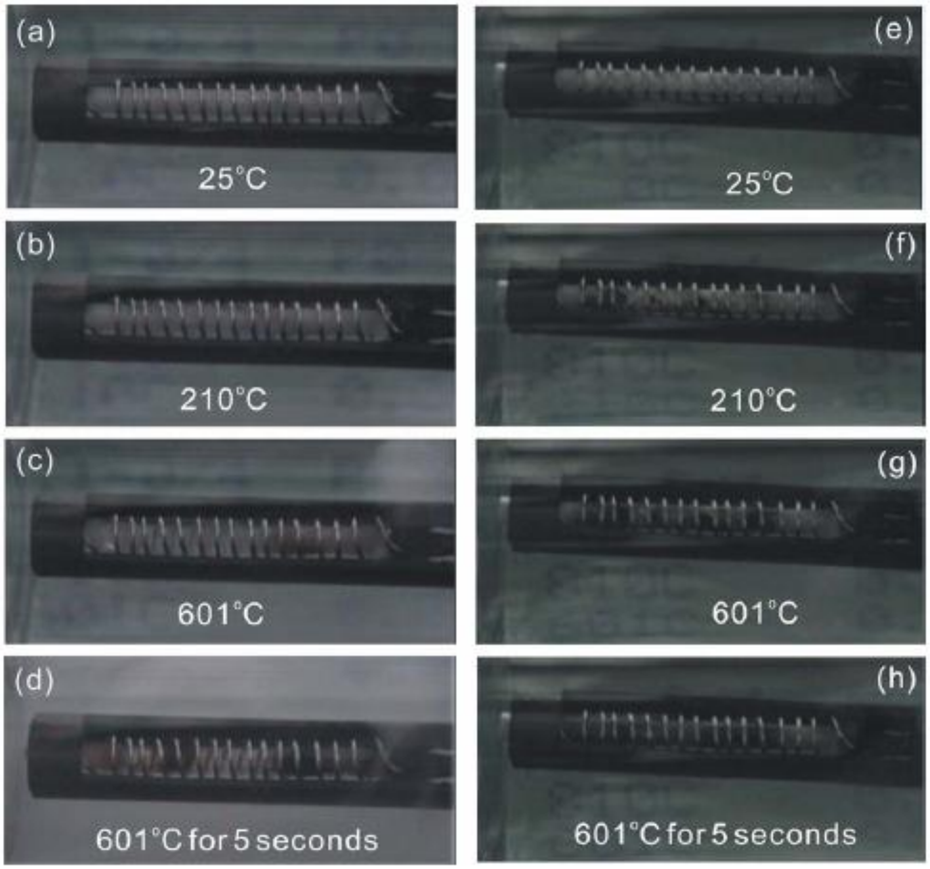

Figure 4.4 Comparison of glucose fast pyrolysis (a, b, c, and d) and glucose/ZSM-5 pyrolysis (e, f, g, and h; catalyst to feed ratio = 19).

4.3.1.4 FTIR Results

To further investigate the thermal decomposition of glucose in the presence of ZSM-5, ex-situ FTIR was performed at various temperature steps. Glucose with ZSM-5 (catalyst : feed ratio = 1.5) was pyrolyized with a heating rate of 100 ℃ s^{-1} to various final temperatures. Upon reaching the final reaction temperature the probe was quenched with room temperature helium flow. FTIR was performed on the residues left in the quartz reactor. Figure 4.5 (I) shows the infrared spectra (1200-2000 cm^{-1} region) of the reaction mixture obtained at various temperatures. Figure 4.5 (II) shows the CH stretching region

(2700-4000 cm^{-1}) of the same spectra. Ramping to a final temperature of 100 or 200 ℃ does not alter the glucose composition significantly as the CH_2 bending modes are of similar intensity. However, it can be seen from the disappearance of the C-H bending modes of glucose at 1340, 1379 and 1460 cm^{-1} (Figure 4.5 (I)) that the glucose decomposes between 200 and 300 ℃. Similarly, in Figure 4.5 (II) the three aliphatic C-H modes at 2890, 2914 and 2945 cm^{-1} are lost between 200 and 300 ℃.

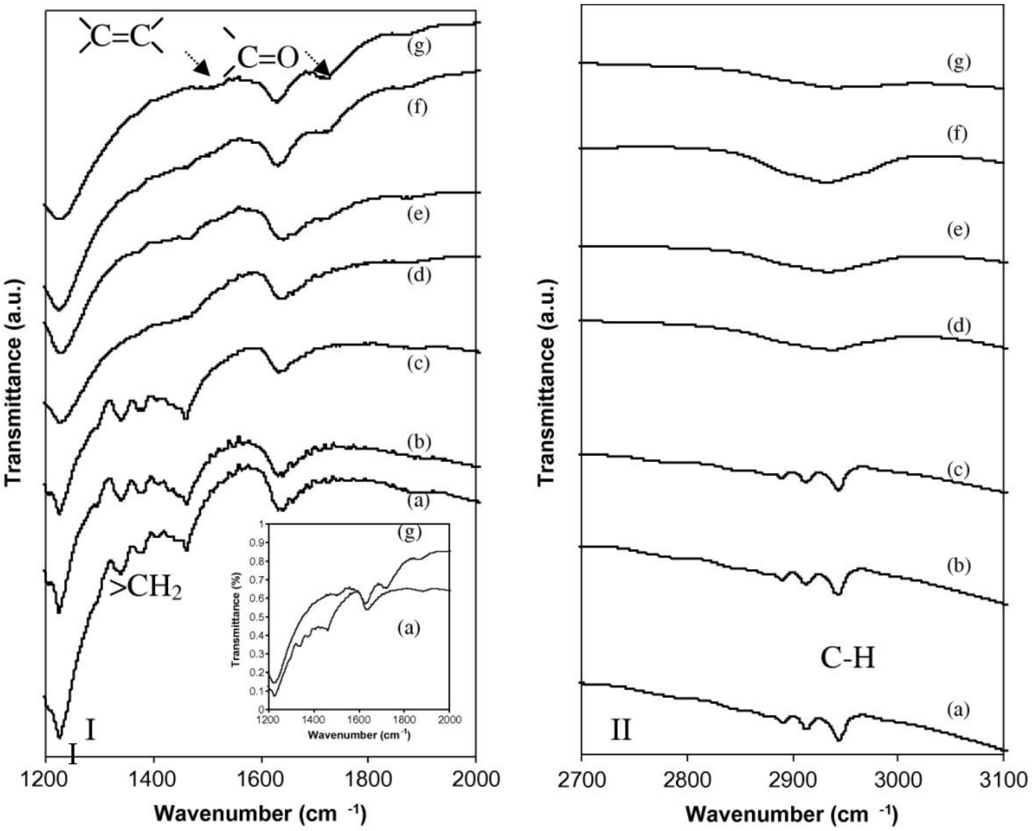

Figure 4.5 IR spectra for glucose pyrolysis in the presence of ZSM-5 (catalyst to feed ratio = 1.5) at 100 ˚C s^{-1} to a final temperature of: (a) unreacted (b) 100˚C, (c) 200˚C, (d) 300˚C, (e) 400˚C, (f) 500˚C, (g) and 600˚C. (I) 1200-2000 cm^{-1} region and (II) 2700-3100 cm^{-1} region. Spectra are off-set to show the bands.

From Figure 4.5 (I) it can be seen that there is a new composition formed at temperatures above 400℃ from the new peaks at 1492 and 1706 cm^{-1}. At 600 ˚C, the presence of C=C bonds (C=C vibrations at ca. 1500 cm^{-1}) and carbonyl groups (C=O, ca. 1700 cm^{-1}) are evident. Sarbak et al. [74] who studied coke formation on HX zeolite attributes the bands at 1500 and 1589 cm^{-1} to presence of naphthalenes. Band positions for these spectra in Figure 4.5 are assigned in Table 4. 2 [75-77].

Table 4.2 Infrared band positions (cm^{-1}) and assignments for the fast pyrolysis of glucose with ZSM-5 (catalyst:feed ratio = 1.5) at various temperatures.

glucose	**100˚C**	**200˚C**	**300˚C**	**400˚C**	**500˚C**	**600˚C**	**Assignment[75-77]**
433	445	442	436	437	439	439	Si-O-Si external deformation (ZSM-5)
553	541	540	536	539	539	538	Si-O-Si internal deformation (ZSM-5)
	612	611	606				D6R ring mode (ZSM-5)
621							
647	641	632	699				
727	730	725					
775	775	774	779	782	781	786	Si-O sym stretch (ZSM-5)
	790	793					Si-O sym stretch (ZSM-5)
838	834	836					
914	912	912	897				
996							C-O
1023		1022					
1052		1046					
1080	1071	1068	1068	1072	1068	1072	Si-O anti-sym stretch (ZSM-5)
1111		1094					C-O
1148		1138					Ring mode (glucose)
1202	1216	1194					
1225		1217	1215	1217	1216	1216	Si-O anti-sym stretch (ZSM-5)
1295		1284					
1340	1334	1328					CH bend
1379	1363	1365	1355	1352			Sym CH bend
1460	1453	1449	1453	1457	1455		Asym. CH bend
					1492	1492	C=C
	1631	1628	1629		1625	1618	HOH bend (adsorbed water)
			1703h	1703	1706	1706	C=O (acid carboxyl)
	1869	1866	1858	1858	1854	1858	
2890	2886	2887					CH aliphatic (glucose)
2914	2908	2910	2917	2917b	2917b	2922b	CH aliphatic
2945	2935	2941					CH aliphatic (glucose)
3356							OH (glucose)
3412							OH (glucose)

4.3.2 Effect of Temperature on Catalytic Fast Pyrolysis

4.3.2.1 Pyroprobe Results

To investigate the effect of temperature on catalytic fast pyrolysis of glucose final reaction temperatures of 400 ℃, 500 ℃, 600 ℃, 700 ℃ and 800 ℃ were tested. A catalyst to feed ratio of 19:1 and heating rate of 1000 ˚C s^{-1} were used. These reaction conditions were previously determined to maximize the aromatic yield [25] at 600 ^{o}C. It can be seen in Figure 4.6 that increasing reaction temperature from 400 to 800 ℃ increases aromatic yield up to 30% at 600 ℃. At temperatures higher than 600 ℃ there is little change in aromatic yield. Coke yield significantly decreases from 400 to 800 ℃. The yield of carbon monoxide and carbon dioxide increase slightly over the temperature range tested. Aromatic production and coke formation vary inversely, suggesting they are competing reactions.

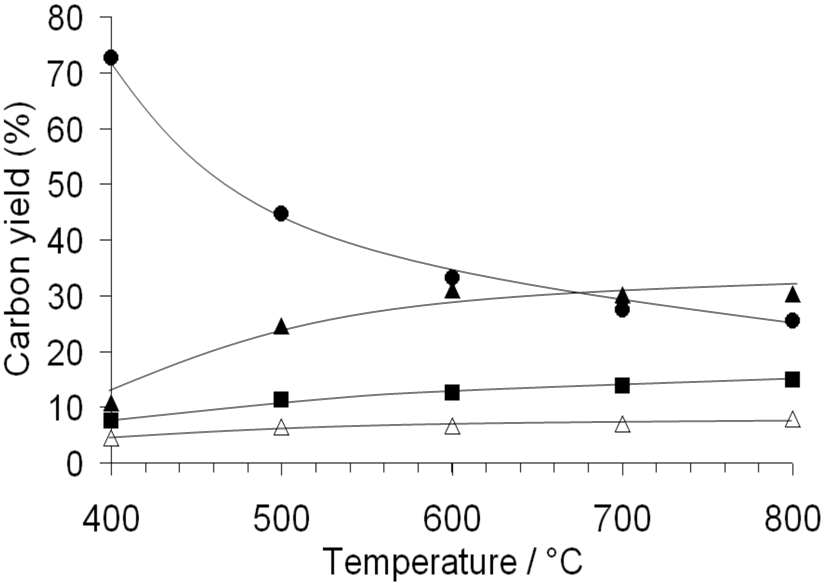

Figure 4.6 Carbon yield as a function of reaction temperature for catalytic fast pyrolysis of glucose with ZSM-5. Reaction conditions: catalyst to feed weight ratio = 19; catalyst ZSM-5 (Si/Al = 15), nominal heating rate 1000 ℃ s^{-1}, reaction time 240 s. Key: ■: carbon monoxide ▲: aromatics Δ: carbon dioxide ●: coke □: total carbon.

Figure 4.7 shows the effect of temperature on the aromatic species selectivity. For simplicity similar aromatic species are grouped together, for example, naphthalenes include: naphthalene, methyl-naphthalenes and ethyl-naphthalenes. As the temperature is increased from 400 to 800 °C, the selectivity to benzene increases from 10 to 30% carbon, while the selectivity for xylene and naphthalene decreases only a small amount. Changing the reaction temperature has little effect on the selectivity for toluene and the C_9 aromatics.

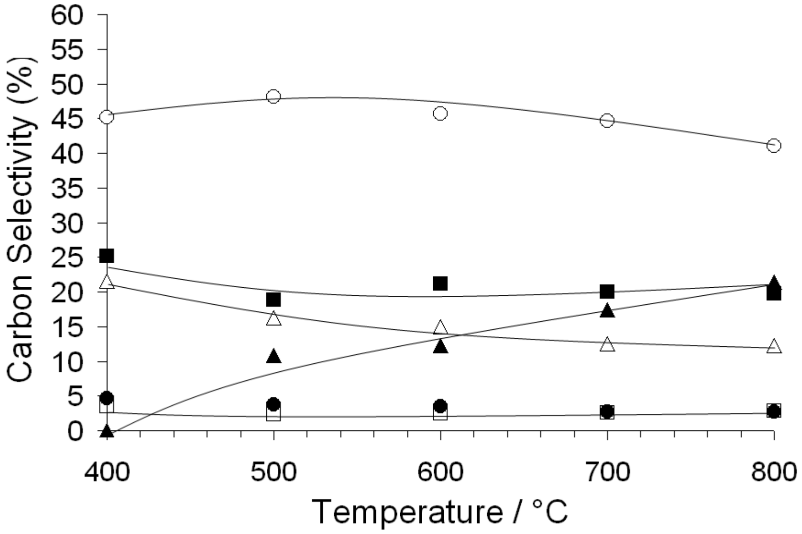

Figure 4.7 Aromatic selectivity as a function of reaction temperature for catalytic fast pyrolysis of glucose with ZSM-5. Reaction conditions: catalyst to feed weight ratio = 19; catalyst ZSM-5 (Si/Al = 15), nominal heating rate 1000 °C s^{-1}, reaction time 240 s. Key: ■: toluene ▲: benzene Δ: xylenes and ethyl-benzene ●: methyl-ethyl-benzene and trimethyl-benzene □: indanes ○: naphthalenes.

Table 4.3 shows the complete list of aromatics produced from catalytic fast pyrolysis of glucose in the presence of ZSM-5 at 600 °C. It can be seen that the primary aromatics produced include benzene, toluene, 1,3-dimethyl-benzene, naphthalene, 1-methyl- naphthalene and 1,5-dimethyl- Naphthalene. Very large molecules such as methyl-phenanthrene are observed only in trace amounts. Naphthalenes are the largest molecules produced in significant quantities, which may be due to the size selectivity of the zeolite catalyst. Naphthalene has a kinetic diameter of ~6.0 Å [78] which is similar to the ZSM-5 pore size of ~6.2 Å (Norman radii adjusted[79]).

Table 4.3 Carbon yields of aromatics produced from catalytic fast pyrolysis of glucose with ZSM-5. Reaction conditions: catalyst to feed weight ratio = 19; catalyst ZSM-5 (Si/Al = 15), nominal heating rate 1000 ℃ s^{-1}, reaction temperature 600 ℃, reaction time 240 s.

Aromatic Component	Yield (% carbon)	Selectivity (% carbon)
Benzene	4.07	12.59
Toluene	7.53	23.29
Ethylbenzene	0.18	0.57
Benzene, dimethyl-(m,o or p)	3.72	11.50
Benzene, dimethyl-(m, o or p)	1.17	3.61
Benzene, (1-methylethyl-)	0.20	0.61
Benzene, 1-ethyl-3-methyl-	0.11	0.35
1,2,4-Trimethylbenzene	0.48	1.47
Benzene, 1-ethyl-3-methyl-	0.03	0.11
Indane	0.14	0.44
Indene	0.10	0.30
Indane, 1-methyl-	0.10	0.31
1H-Indene, 1-methyl	0.07	0.22
Naphthalene	4.28	13.23
Naphthalene, 1-methyl-(m,p)	4.25	13.15
Naphthalene, 1-methyl-(m,p)	2.13	6.58
Naphthalene, 1-ethyl-	0.22	0.67
Naphthalene, 1,5-dimethyl-(m,p)	1.05	3.24
Naphthalene, 1,5-dimethyl-(m,p)	0.73	2.24
Naphthalene, 1,5-dimethyl-(m,p)	0.55	1.71
Naphthalene, 1,3-dimethyl-	0.21	0.64
Naphthalene, 1,4,6-trimethyl-	0.12	0.36
Dibenzofuran	0.06	0.18
Naphthalene, 2,3,6-trimethyl-	0.05	0.15
Naphthalene, 1,4,6-trimethyl-	0.04	0.12
Naphthalene, 1,3,6-trimethyl-	0.03	0.08
Naphthalene, 1,3,6-trimethyl-(m,p)	0.03	0.08
Fluorene	0.10	0.30
9H-Fluorene, 4-methyl-	0.03	0.10
Anthracene	0.06	0.19
Phenanthrene	0.25	0.76
Anthracene, 2-methyl-	0.02	0.07
Phenanthrene, 3-methyl-	0.13	0.39
Phenanthrene, 2-methyl-	0.12	0.37

4.3.3 Effect of Reaction Time on Catalytic Fast Pyrolysis

4.3.3.1 Pyroprobe Results

To investigate the effect of reaction time on the yield of the catalytic fast pyrolysis products, the carbon yield of aromatics, CO and CO_2 were measured at various total reaction times from 1 and 240 s at 600 ℃. Figure 4.8 shows the carbon yield as a function of reaction time for the optimized reaction conditions. Initially, after 1 s of reaction, CO and CO_2 comprise the main products and increase little throughout the reaction. After 3 s reaction, the aromatic yield is higher than CO or CO_2 and increases rapidly as the reaction proceeds. After 240 s, the aromatic yield appears to be level off at a maximum carbon yield of 32%. Reaction times as little as 2 min give aromatic yields in excess of 30carbon%.

The aromatic selectivity as a function of reaction time for CFP of glucose with ZSM-5 is shown in Figure 4.9. Apart from the yield of naphthalenes and indane, the selectivity of all other aromatics decreases between 1 and 3 seconds of reaction time at 600 ℃. During this same period, the naphthalenes' selectivity dramatically increases from 18 to 40%. Naphthalenes are the major products between 3 and 240 s, and there is little selectivity change for reaction greater than 3 s.

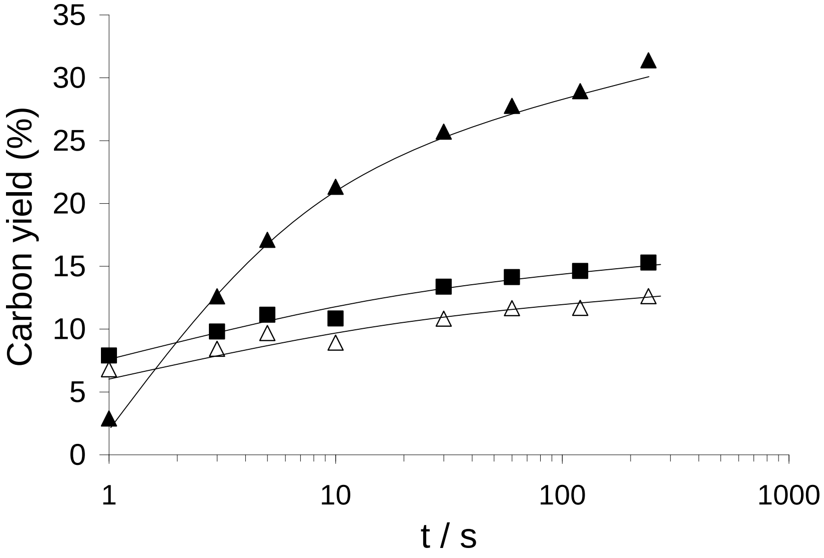

Figure 4.8 Carbon yield as a function of reaction time for catalytic fast pyrolysis of glucose with ZSM-5. Reaction conditions: catalyst to feed weight ratio = 19; catalyst ZSM-5 (Si/Al = 15), nominal heating rate 1000 ℃ s^{-1}, reaction temperature 600 °C. Key: ■: carbon monoxide ▲: aromatics Δ: carbon dioxide.

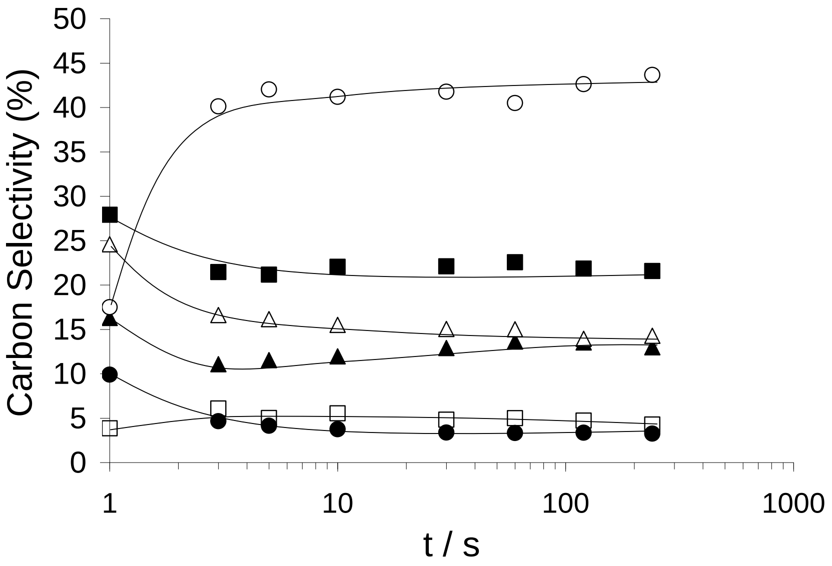

Figure 4.9 Aromatic selectivity as a function of reaction time for catalytic fast pyrolysis of glucose with ZSM-5. Reaction conditions: catalyst to feed weight ratio = 19; catalyst ZSM-5 (Si/Al = 15), nominal heating rate 1000 °C s^{-1}, reaction temperature 600 °C. Key: ■: toluene ▲: benzene Δ: xylenes, ethyl-benzene ●: methyl-ethyl-benzene trimethyl-benzene □: indanes ○: naphthalenes

4.3.3.2 FTIR Results

Figure 4.10 shows the infrared spectra of pure glucose after pyrolysis at 600 °C for 1 s and 120 s compared to unreacted glucose. The peak assignments are given in Table 4.4 [74, 77]. After 1 s reaction time, the CH_2 deformation modes of glucose are no longer present indicating that little unreacted glucose remains. Furthermore, the loss of the band at 1148 cm^{-1} shows that the 6-carbon ring mode is not present after 1 s reaction. The new band that appears at 1703 cm^{-1} after 1 s is characteristic of C=O stretching vibration. Therefore, the decomposition of glucose appears to go through a compound with carboxyl character [74]. For C=O stretching vibrations, 1703 cm^{-1} is in the carboxylic acid range. After even the short time of 1 s, there is very little material left in the pyroprobe reactor, only a residue film.

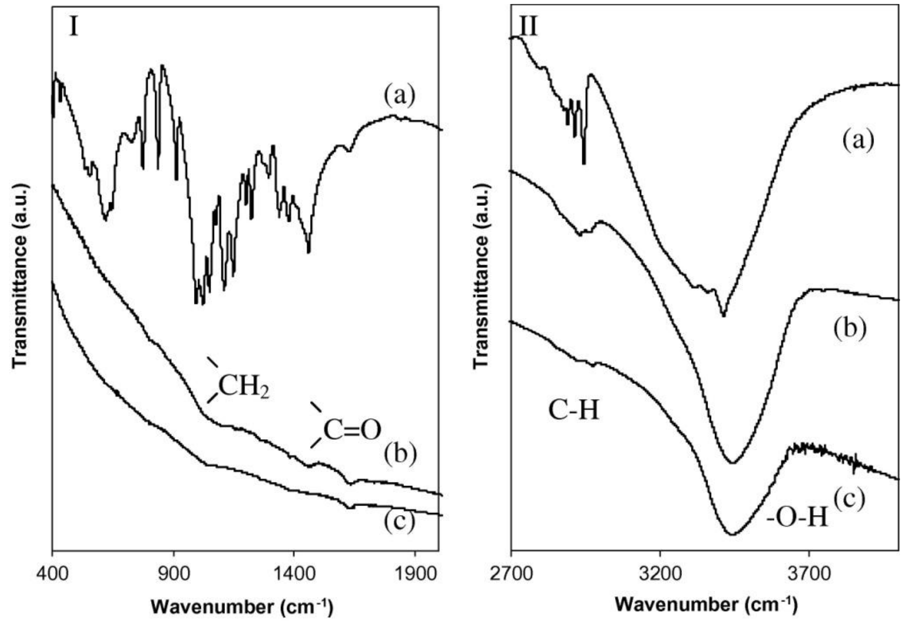

Figure 4.10 FTIR spectra of pure glucose (a) unreacted and pyrolyzed at 600 ℃ for (b) 1 s and (c) 120 s. (I, region 400-2000 cm^{-1} and II, CH and OH stretching region 2700-4000 cm^{-1}).

Table 4.4 Infrared band positions (cm^{-1}) and assignments for the fast pyrolysis of glucose 600 ˚C.

Glucose	1 s	120 s	Assignment[74, 77]
433			Framework mode (glucose)
553			Framework mode (glucose)
621			C-C, C-O stretch (glucose)
647			C-C, C-O stretch (glucose)
727			C-C, C-O stretch (glucose)
775			CH deformation (glucose)
	797	787	CH deformation
838			CH2CH deformation (glucose)
	873		
914			C-OH and CH deformation (glucose)
996			
1023	1021	1027	C-OH deformation (glucose)
1052			CH deformation (glucose)
1080			CH, COH deformation (glucose)
1111			CH, COH bend (glucose)
1148			Ring mode (glucose)
1202			C-O (glucose)
1225	1257		CH2 (glucose)
1295	1374	1374	CH2 bend, C-OH (glucose)
1340			CH bending (glucose)
1379			CH bending (glucose)
1460	1443		CH2 bend, COH (glucose)
	1620	1621	HOH bend (adsorbed water)
	1703		C=O stretch (carboxylic)
2890	2841		CH stretch (glucose)
2914	2910	2910	CH stretch (glucose)
2945	2951	2957	CH stretch (glucose)
3356			OH stretch (glucose)
3412			OH stretch (glucose)

Figure 4.11 (I) and (II) show the infrared spectra of glucose-ZSM-5 at a low catalyst to feed ratio (1.5) reacted at 600 ℃ for various time periods between 1 and 120 s. After 3 s reaction, the bands from the glucose (including, 1460, 2890, 2914 and 2945 cm^{-1}) have completely disappeared indicating the decomposition of glucose. A longer reaction time 3 s (compared to 1 s) is required to fully decompose the glucose, which is likely due to the larger mass of glucose present. The infrared spectra of the sample after 3s reaction at 600 ℃ shows two new bands at 1571 and 1711 cm^{-1} along with a broad band in the C-H stretching regions centered at 2950 cm^{-1}. The former two bands are assigned to C=C stretch and C=O stretch. The C=O stretch is in the characteristic wave number region for the diketonics present in furfuryl alcohol resins[80], while the C=C stretch may be from aromatics. A comparison of the peaks to those of furfuryl alcohol resins is given in Table 4.5 [75-77, 80]. Therefore, the coke present after 3 s reaction has aromatic and ketone characteristics. The broad band in the C-H region indicates a broad range of organic compounds/compositions present. With further reaction time up to 120 s, these bands decrease until 120 s sample indicating these intermediates have been decomposed.

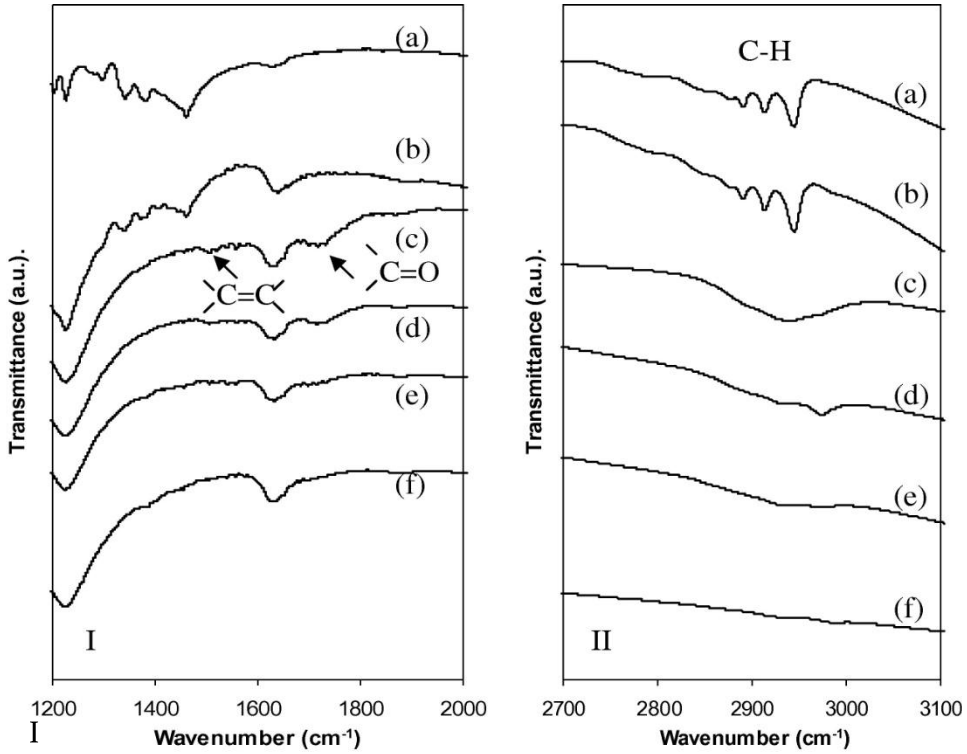

Figure 4.11 Infrared spectra of (a) pure glucose and glucose with ZSM-5 (catalyst : feed ratio = 1.5) and reacted at 600 ℃ for various times (b) unreacted (c) 1 s, (d) 3 s, (e) 5 s and (f) 120 s. (I) 400-2000 cm^{-1} region and (II) CH stretching region (2700-3100 cm^{-1}) .

Table 4.5 Infrared band positions (cm^{-1}) and assignments for the fast pyrolysis of glucose with ZSM-5 (catalyst : feed ratio = 1.5) at various temperatures compared to polyfurfuryl alcohol.

glucose	Polyfurfuryl alcohol on HY zeolite [80]	Assignment	Polyfurfuryl alcohol on HY zeolite heated to 673K[80]	Assignment	Glucose on ZSM-5 heated to 600˚C for 1s	Glucose on ZSM-5 heated to 600˚C for 3s	Glucose on ZSM-5 heated to 600˚C for 120s	Assignment[75-77]
1225					1216			Si-O anti-sym stretch (ZSM-5)
1295							1284	
1340								CH bend
1379	1375	CH bend	1350	C=C carbon			1381	Sym CH bend
1460	1422	CH bend						Asym. CH bend
	1487	Oligomeric C=C			1492			C=C
	1575	Oligomeric C=C				1571	1589	
	1628	HOH bend and carbon C=C	1630	C=C carbon	1618			HOH bend (adsorbed water)
	1710	Diketonic C=O			1706	1711		C=O (carbonyl)
	~2500				1858			
2890						2885	2912	CH (glucose)
2914	2924	C-H			2922b	2912		CH
2945						2962	2971	CH (glucose)
	3120	C-H						
3356								OH (glucose)
3412								OH (glucose)

4.3.4 Effect of ZSM-5 to Glucose Ratio on Catalytic Fast Pyrolysis

4.3.4.1 Pyroprobe Results

Figure 4.12 shows the effect of catalyst to glucose ratio on the carbon yield of products at the optimal reaction conditions. Using a catalyst to feed ratio 19 produces the highest aromatic yield and lowest coke yield. The yield of partially deoxygenated species decreases from 15% to ~0% with increasing catalyst to feed ratio from 1.5 to 19. The oxygenates include the following: furan, 2-methyl furan, furfural, 4-methyl-furfural, furan-2-methanol, hydroxyacetylaldehyde, and acetic acid. Trace amounts of anhydrosugars were also observed. The distribution of the partially deoxygenated species as a function of catalyst to glucose ratio for catalytic fast pyrolysis is shown in Figure 4.13.

The aromatic selectivity is not a strong function of the catalyst to glucose ratio as shown in Figure 4.14. Increasing the catalyst to feed ratio slightly increases the selectivity for toluene, xylenes, and ethyl-benzene, while slightly decreasing the selectivity for benzene, methyl-ethyl-benzene, trimethyl-benzene, indanes and naphthalenes. The largest change in selectivity is for the decrease of indanes from 12 to 4% and the increase of toluene from 13 to 22%.

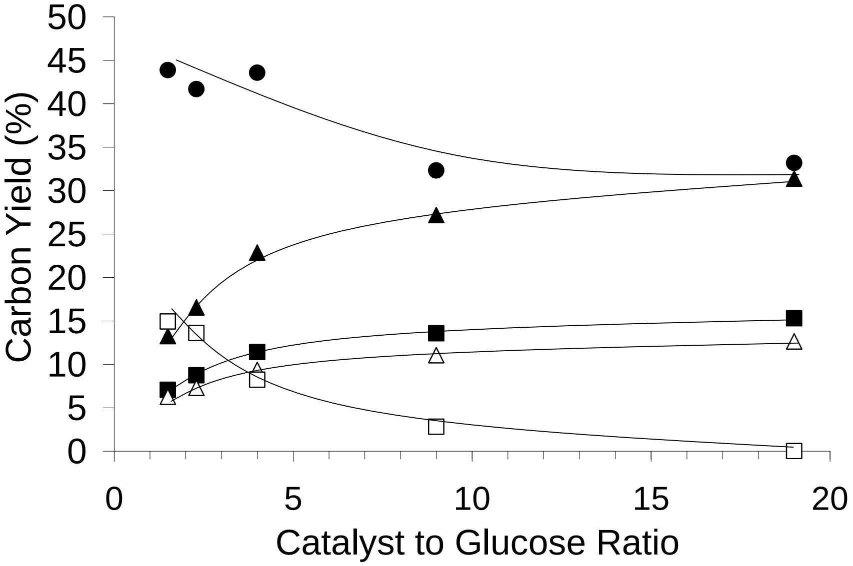

Figure 4.12 Carbon yield as a function of catalyst to glucose ratio. Reaction conditions: nominal heating rate 1000 ℃ s-1, final reaction temperature 600 ℃, reaction time 240 s. Key: ■: carbon monoxide ▲: aromatics Δ: carbon dioxide □: partially deoxygenated species ●: coke.

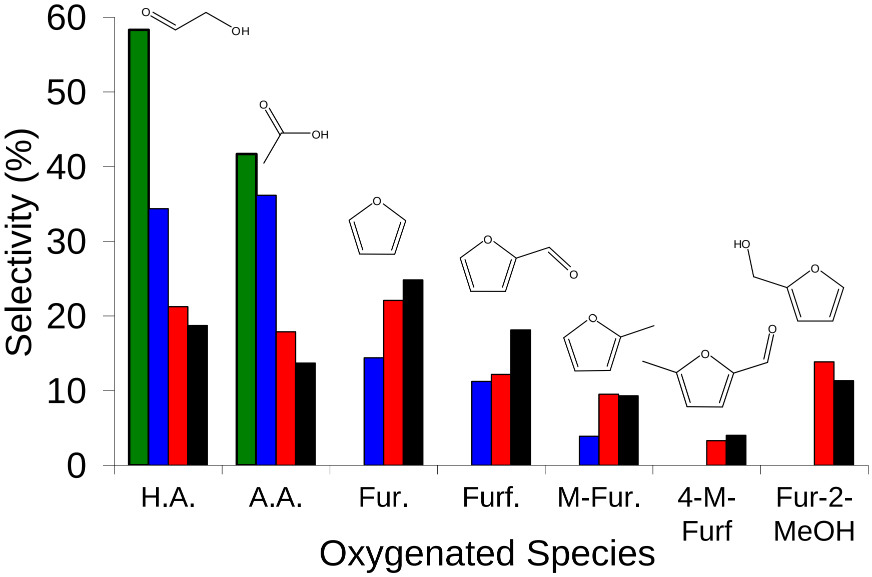

Figure 4.13 Distribution of partially deoxygenated species as a function of catalyst to glucose ratio for catalytic fast pyrolysis. Reaction conditions: nominal heating rate 1000 ℃ s^{-1}, final reaction temperature 600 ℃, reaction time 240 s. Key: catalyst:glucose ratio = 9 (green), catalyst:glucose ratio = 4 (blue), catalyst:glucose ratio = 2.3 (red), catalyst:glucose ratio = 1.5 (black). The species quantified include: (H.A.) hydroxyacetylaldehyde, (A.A.) acetic acid, (Fur.) furan, (Furf) furfural, (M-Fur) methyl furan, (4-M-Furf) 4-methyl furfural, (Fur-2-MeoH) furan-2-methanol.

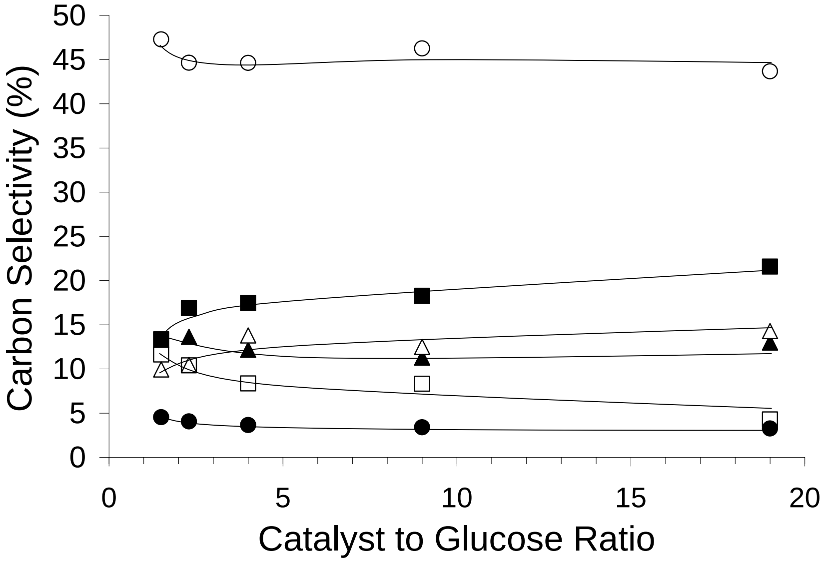

Figure 4.14 Distribution of aromatic species as a function of catalyst to glucose ratio for catalytic fast pyrolysis. Reaction conditions: nominal heating rate 1000 °C s^{-1}, final reaction temperature 600 °C, reaction time 240 s. Key: ■: toluene ▲: benzene Δ: xylenes, ethyl-benzene ●: methyl-ethyl-benzene trimethyl-benzene □: indanes ○: naphthalenes

4.3.5 Conversion of Oxygenated Intermediates by Catalytic Fast Pyrolysis

Using low (1.5) catalyst-to-feed ratio, mainly furan-based oxygenates are produced. The partially deoxygenated species detected are likely intermediates in the formation of aromatics, since at low catalyst-to-feed ratios, the high quantities of oxygenates leave the reactor before they can react further to form aromatics. Using these oxygenates as feedstocks at the same reaction conditions as glucose CFP may shed light on the heterogeneous chemistry in glucose conversion to aromatics. The oxygenated intermediates; acetic acid, furan, furfural and methyl-furan were chosen as feedstocks for this study. These represent the dominant products observed at low (1.5) catalyst-to-feed ratios.

4.3.5.1 Pyroprobe Results

Figure 4.15 shows the products yields of catalytic pyrolysis of acetic acid, furan, furfural, methyl-furan and furfuryl alcohol. A catalyst-to-feed ratio of 19, 240 s reaction time, and 600 ℃ final reaction temperature were used in this set of experiments. As shown in Figure 4.15, the oxygenates form a range of aromatics, CO and CO_2. Acetic acid produces mainly CO_2 through decarboxylation, however, almost all of the remaining carbon goes to aromatics (~30% carbon yield). In the case of furan-based feedstocks, it is shown in Figures 4.15 and 4.16 that similar yields (between 35 and 50%) and selectivity of aromatics were produced from furfural, furfuryl alcohol, furan and 2-methyl furan. The yields of gases were also similar for the furans with the exception being the increased amount of decarbonylation with the furfural feed.

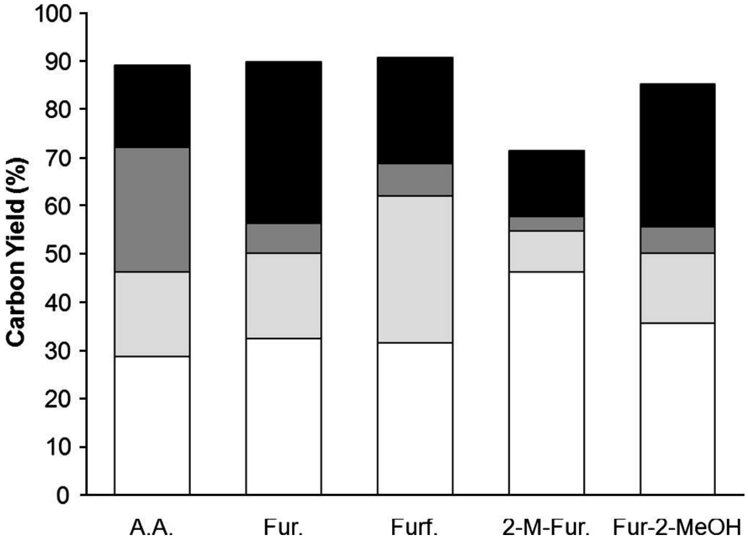

Figure 4.15 Distribution of product yields as a function of intermediate compounds reacted using catalytic fast pyrolysis. Reaction conditions: nominal heating rate 1000 ℃ s-1, final reaction temperature 600 ℃, reaction time 240 s. Key : aromatics (white), carbon monoxide (light grey), carbon dioxide (dark grey), and coke (black). Abbreviations for the intermediate species are: acetic acid (A.A.), furan (Fur.), furfural (Furf.), 2-methyl furan (2-M-Fur.) and furan 2-methanol (Fur-2-MeOH).

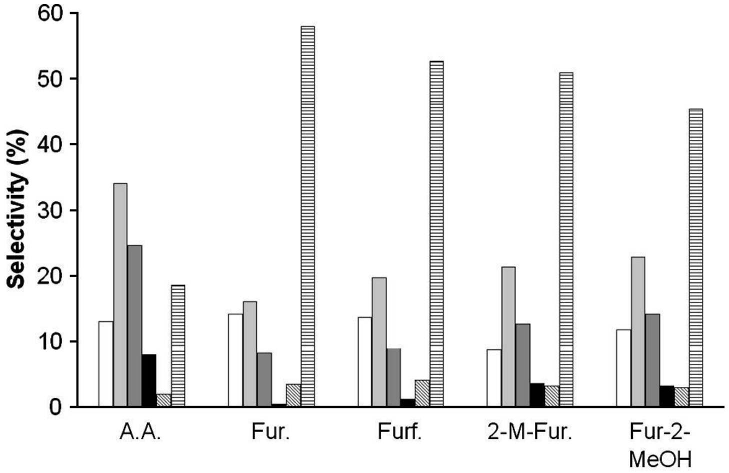

Figure 4.16 Selectivity of conversion of intermediate compounds reacted using catalytic fast pyrolysis. Reaction conditions: nominal heating rate 1000℃ s-1, final reaction temperature 600 ℃, reaction time 240 s. Key: benzene (white), toluene (light grey), xylene and ethyl-benzene (dark grey), methyl-ethyl-benzene and trimethyl-benzene (black), indanes and indenes (diagonal lines), and naphthalenes (horizontal lines). Abbreviations for the intermediate species are: acetic acid (A.A.), furan (Fur.), furfural (Furf.), 2-methyl furan (2-M-Fur.) and furan 2-methanol (Fur-2-MeOH).

4.3.6 Isotopic Labeling of Glucose Feeds

In the first set of experiments a 1:1 wt% mixture of pure ^{12}C and ^{13}C glucose was pyrolyzed at two different catalyst to feed ratios (2.3 and 19 catalyst to feed weight ratio). In a second set of experiments a 1:1 wt% mixture of ^{12}C benzene and ^{13}C glucose was pyrolyzed in order to determine the role of single ring aromatics in the formation of polycyclic aromatics. In the last set of experiments, a 1:1 wt% mixture of ^{12}C naphthalene and ^{13}C glucose was pyrolyzed to determine whether naphthalene is susceptible to alkylation reactions.

When mixtures of ^{12}C and ^{13}C glucose were reacted at a low catalyst to feed ratio (2.3 of ZSM-5 to glucose ratio), the non-aromatic products produced including: CO, CO_2, and the previously mentioned dehydrated species (i.e. anhydrosugars, furans, acids) were all monoisotopic (all ^{12}C or all ^{13}C). This indicates that no C-C bonds were formed on non-aromatic products in this reaction. However, the aromatic products were all intramolecular mixtures of ^{13}C and ^{12}C for reactions of ^{13}C and ^{12}C glucose as shown in Figure 4.17. The relative amounts of ^{13}C and ^{12}C in the single ring aromatic species (Figure 4.17 a-c) are normally distributed with the maximum abundance corresponding to a 1:1 isotopic mix. This suggests that the single ring aromatics are formed from a random mixture or hydrocarbon pool that exists within the zeolite formed from the dehydrated species. Inside this hydrocarbon pool, oxygen is removed from the dehydrated species as a combination of CO, CO_2 and H_2O. The reported carbon scrambling is similar with previously reported reactions of isotopically labeled propane[81-82] and methanol[70, 83-84] on ZSM-5.

In contrast, the isotopic distribution for naphthalene (Figure 4.17 d) is composed of two distinct groups of peaks, suggesting that naphthalene is formed through another route. The bimodal distribution indicates that a molecule with a random distribution (e.g. benzene) oligomerized with a monoisotopic molecule to form naphthalene. Furthermore the center of each of the groups (m/z =130 and 134) are separated by four suggesting the monoisotopic reactant is four carbons.

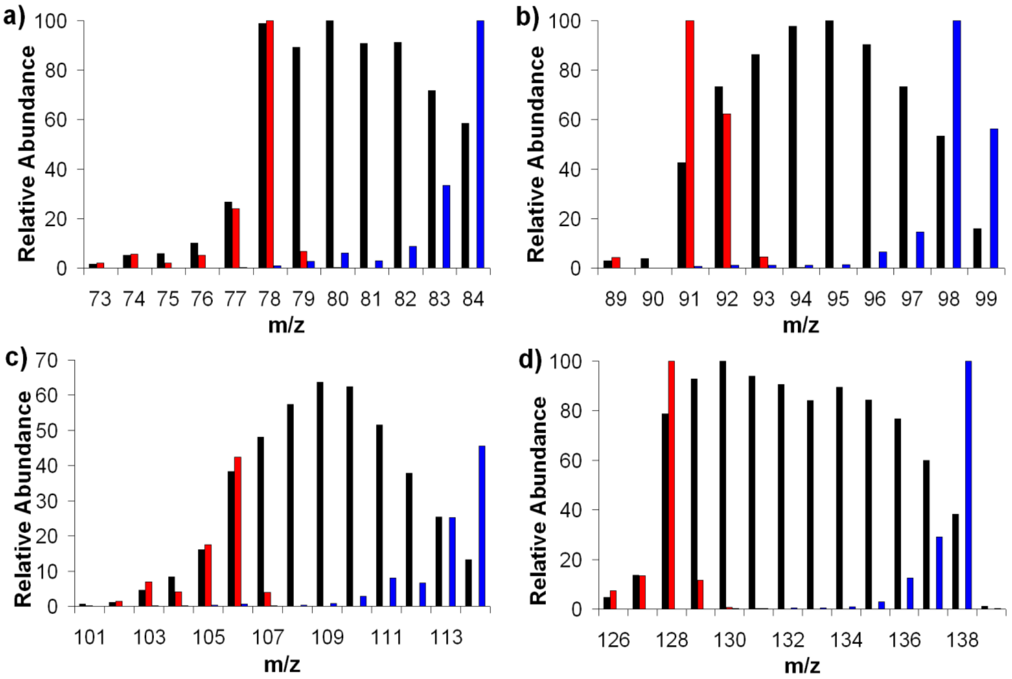

Figure 4.17 The isotopic distributions for: a) benzene, b) toluene, c) xylene and d) naphthalene from the pyrolysis of a 1:1 wt% mix of ^{12}C glucose and ^{13}C glucose. Pure ^{12}C and ^{13}C spectrums for the given molecule are shown in red and blue, respectively. Reaction conditions: catalyst to feed weight ratio = 19; catalyst ZSM-5 (Si/Al = 15), nominal heating rate 1000℃ s-1, reaction temperature 600℃, reaction time 240 s.

To further investigate how naphthalene is formed, we performed experiments with ^{12}C benzene and ^{13}C glucose. As shown in Figure 4.18a two different types of naphthalene are formed in this reaction. One naphthalene is formed from the ^{13}C glucose. The other naphthalene is a mixture of ^{12}C and ^{13}C. The ratio of the naphthalene from glucose compared to the naphthalene from benzene and glucose is 10 to 5.5. Similar results were obtained for the methyl and dimethyl-naphthalene (Figure 4.18b-c).

In contrast, only small amounts of the single ring aromatics are formed by alkylation of the benzene. Over 90 % of the toluene and xylenes are formed from the ^{13}C glucose as shown in Figures 4.18d-e. The relative intensity of mixed xylene is lower than the relative intensity of mixed toluene. This is because xylene has to be alkylated twice as opposed to one alkylation for toluene. However, as seen in Figure 4.18f, the relative intensity for mixed isotope ethyl-benzene compared to the pure ^{13}C species is much higher meaning alkylation of benzene is an important route for the formation of ethyl benzene.

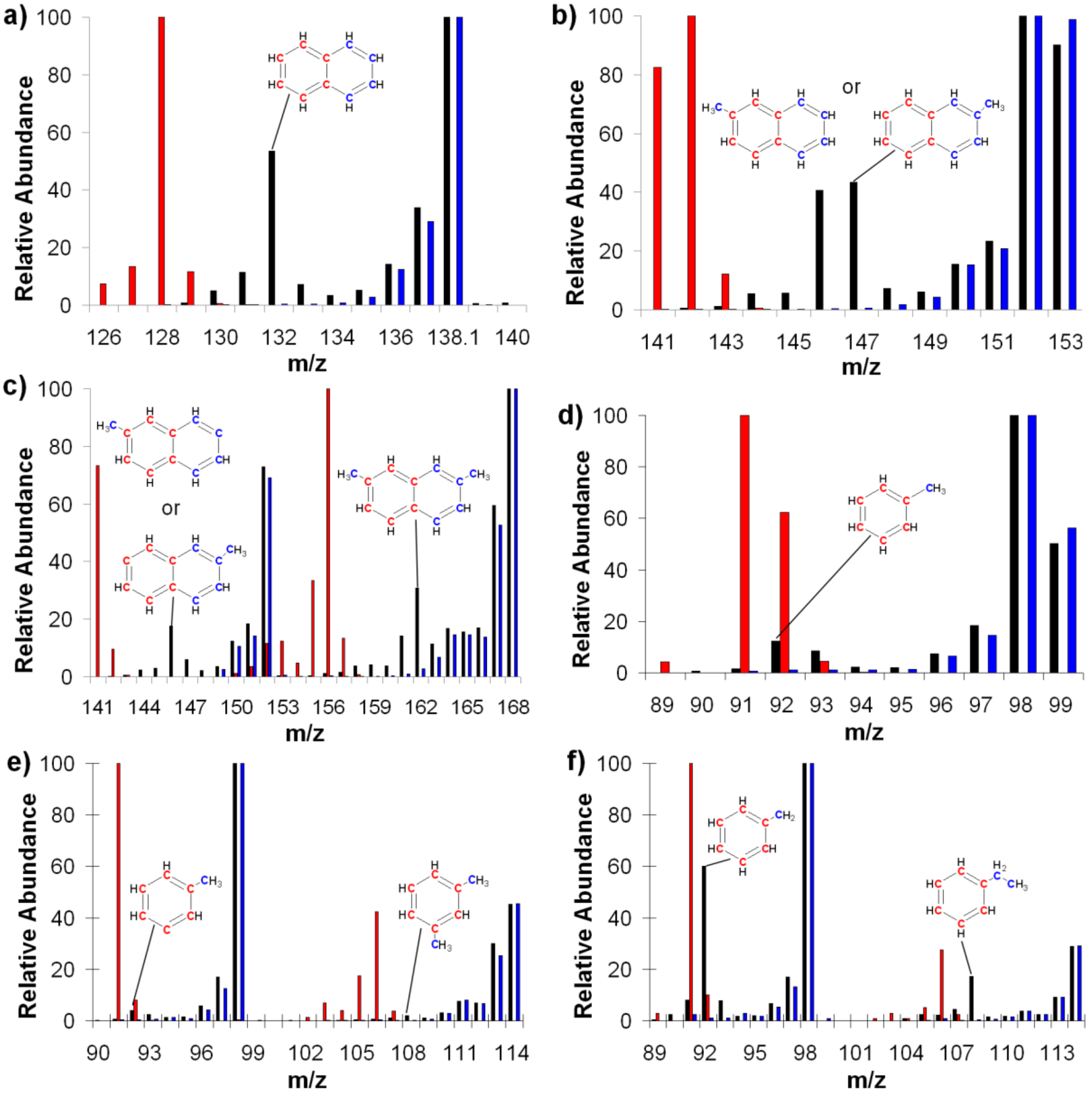

Figure 4.18 The isotopic distributions for: a) naphthalene, b) methyl-naphthalene, c) dimethyl-naphthalene, d) toluene, e) xylene and f) ethyl-benzene from the pyrolysis of a 1:1 wt% mix of 12C benzene and ^{13}C glucose. Blue and red labeled carbons represent ^{13}C and ^{12}C carbons, respectively. Pure ^{12}C, and ^{13}C spectrums for the given molecule are shown in red and blue, respectively. Reaction conditions: catalyst to feed weight ratio = 19; catalyst ZSM-5 (Si/Al = 15), nominal heating rate 1000℃ s-1, reaction temperature 600℃, reaction time 240 s.

We studied catalytic fast pyrolysis of ^{12}C naphthalene with ^{13}C glucose to study the rate of alkylation of naphthalene. The spectrum of methyl-naphthalene, dimethly-naphthalene and trimethyl-naphthalene are shown in Figure 4.19. As shown in these figures, the relative intensity of the methyl naphthalene formed from the ^{12}C naphthalene reacting with the oxygenate is 40% compared to the ^{13}C methyl-naphthalene from the oxygenate. This suggests that naphthalene can be formed first in this reaction and then undergo alkylation from a species in the hydrocarbon pool.

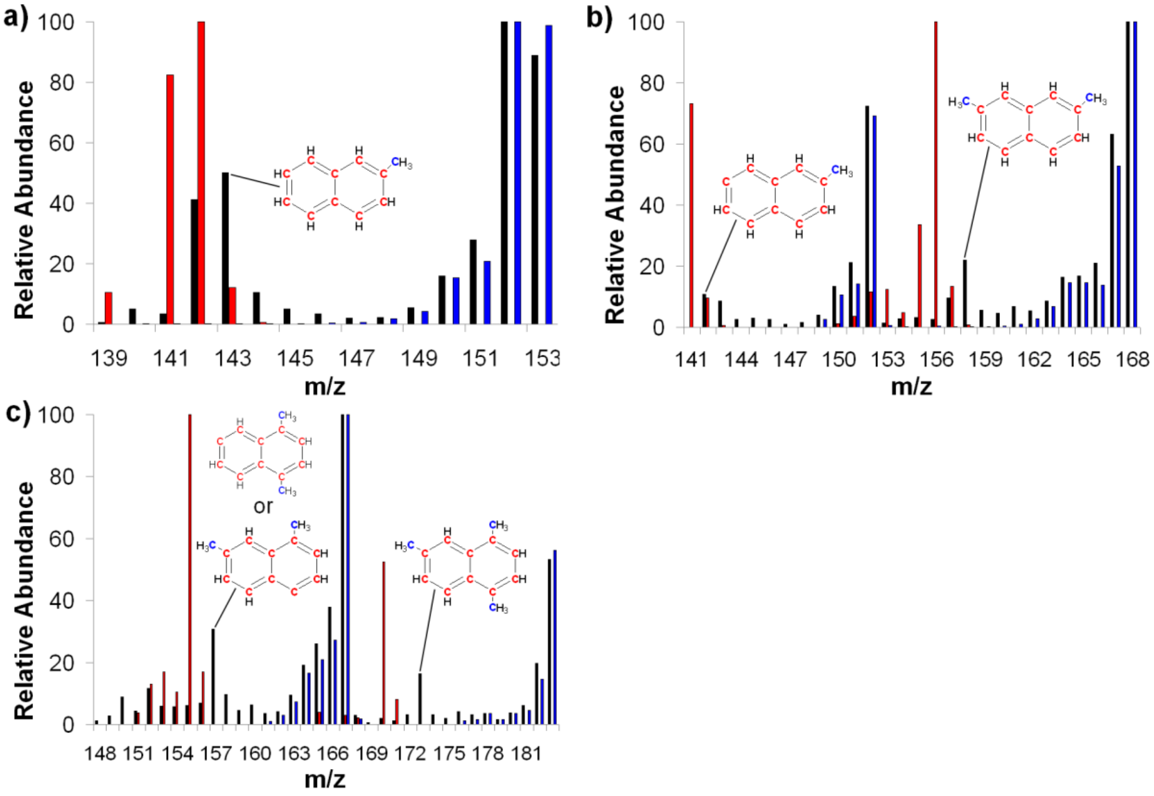

Figure 4.19 The isotopic distributions for a) methyl-naphthalene, b) dimethyl-naphthalene, c) trimethyl-naphthalene from the pyrolysis of a 1:1 wt% mix of ^{12}C naphthalene and ^{13}C glucose. Blue and red labeled carbons represent 13C and 12C carbons, respectively. Pure ^{12}C and ^{13}C spectrums for the given molecule are shown in red and blue, respectively. Reaction conditions: catalyst to feed weight ratio = 19; catalyst ZSM-5 (Si/Al = 15), nominal heating rate 1000℃ s-1, reaction temperature 600℃, reaction time 240 s.

4.3.7 Effect of Coke on Catalytic Activity

4.3.7.1 Pyroprobe Results

To investigate the effect of coke on the activity of ZSM-5 for the conversion of glucose the spent catalyst was recycled and pyrolized again with fresh glucose. As shown in Figure 4.20, the aromatic yield does not decrease with the repeated use of coked ZSM-5, indicating that the active sites of ZSM-5 remain despite of the coke on the catalyst phase. In fact, the aromatic yield slightly increases with subsequent cycles. It appears that the coke deposited on the catalyst has the active form which can be an intermediate for aromatic production. The aromatic selectivity observed for the coked catalyst after 1 and 2 times reuse is shown in Figure 4.20. There is a small decrease in the selectivity for benzene and toluene and a small increase indenes and naphthalenes with increasing coke content. The ethyl benzenes and methyl, ethyl benzenes are unaffected by the increase in coke level.

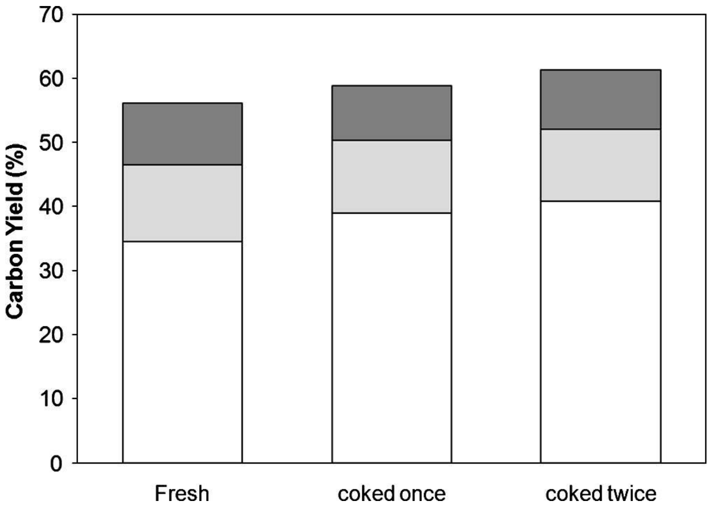

Figure 4.20 Product yields in the conversion of glucose with spent catalysts at 600 ℃ and a catalyst to feed ratio of 19. Key: aromatics (white), carbon monoxide (light grey), and carbon dioxide (dark grey)

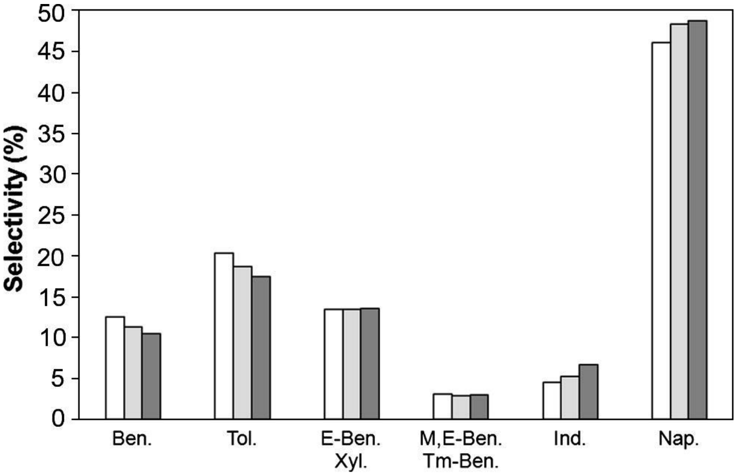

Figure 4.21 Selectivity of conversion of glucose with spent catalysts at 600 °C and a catalyst to feed ratio of 19. Key: Fresh ZSM-5 (white), 1 time coked ZSM-5 (light grey), and 2 times coked ZSM-5 (dark grey)

4.3.7.2 N_2 Adsorption of ZSM-5 Before and After Reaction

Coke is the major product in the conversion of glucose over ZSM-5. The yield of coke is 33% at a catalyst-to-feed ratio of 19 (600 ˚C for 240 s) and increases with decreasing catalyst concentration. To ascertain whether the coke is deposited on the outer surface of the catalyst particles and/or within the pores of ZSM-5, nitrogen adsorption was performed on ZSM-5 before reaction, after reaction at 19:1 catalyst-to-feed ratio and after reaction at 1.5:1 catalyst-to-feed ratio. Figure 4.22 shows the high resolution adsorption isotherm of fresh and coked ZSM-5. The surface area and pore volume calculated from isotherms are summarized in Table 4.6. It can be seen that, compared to fresh ZSM-5, the amount of adsorbed nitrogen (micropore volume) decreases from 0.12 to 0.067 cm^3g^{-1} as the coke level increases from zero to 0.7 wt% carbon, indicating that some coke is deposited inside the zeolite pores. Further, increasing the amount of coke from 0.7 to 5 wt% does not significantly reduce the micropore volume, which suggests further coking may take place outside of the pores on the catalyst surface. Interestingly, the external surface area does not change greatly between fresh and coked samples. This could be due to the low total quantity of coke on the catalyst. The BET surface area decreases with increasing weight percent of coke, indicating that higher coke levels decrease micropore surface area. It should be noted however, that the BET theory is not strictly valid for microporous materials and hence the C_{BET} constants are negative.

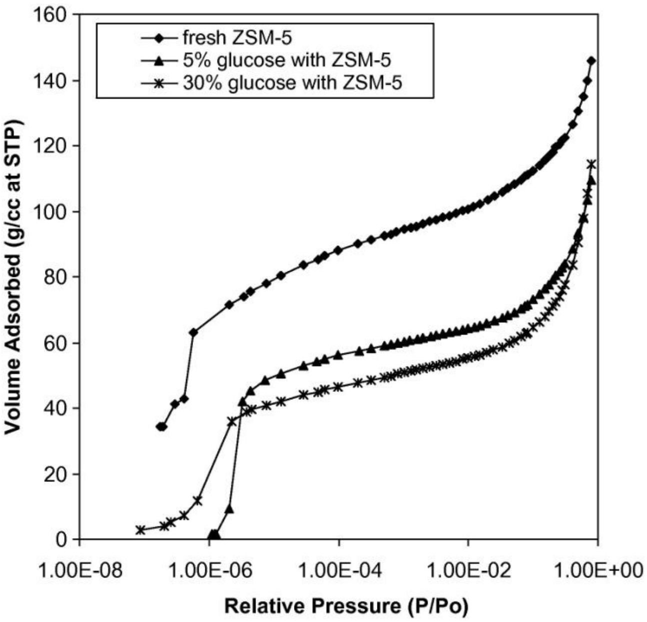

Figure 4.22 High resolution adsorption isotherms (N_2 at 77 K) of fresh ZSM-5 and coked ZSM-5 at the catalyst to feed weight ratio of 19 and 2.3.

Table 4.6 External surface area and micropore volume for the fresh and coked ZSM-5.

Catalyst	**BET Surface area and Constant (C_{BET}) (m^2g^{-1})**	**External surface area (m^2g^{-1})[a]**	**Micro pore volume (cm^3g^{-1})[b]**	**Carbon content (ICP analysis) (wt%)[c]**
ZSM-5 (Si/Al=15)	372, -62	140	0.120	-
Coked ZSM-5 (from 5wt% glucose at 600˚C, reacted 1x)	255, -81	125	0.067	0.69
Coked ZSM-5 (from 30wt% glucose at 600˚C)	236, -151	138	0.049	5

[a] calculated based on the t-method

[b] calculated using the t-method

[c] From ICP analysis. Calculation assumes organic component is primarily carbon.

4.4 Discussion

4.4.1 Chemistry of Glucose Pyrolysis

Figure 4.23 shows the reaction pathways that occur during catalytic fast pyrolysis of glucose. As we discovered in this study, there are two pathways for the thermal decomposition of glucose. Both pathways occur very rapidly with complete glucose decomposition in about one second at 600 °C. At low temperatures, glucose decomposes via retro-aldol and Grob fragmentation reactions to form small oxygenates such as hydroxyacetaldehyde, hydroxyacetone, dihydroxyacetone and d-glyceraldehyde. Other researchers have also shown that these small oxygenates are formed from pyrolysis of carbohydrates [30, 71-72].

At high temperatures, dehydration of glucose is favored. First, glucose is dehydrated to anhydrosugars with levoglucosan as the major product. These anhydrosugars are further dehydrated to furans such as furfural, furfuryl alcohol, furan and 2-methyl furan. Both of these decomposition pathways can occur either homogenously or on acid sites of ZSM-5. From the FTIR results (Figure 4.5), there are carboxylic acids present during decomposition, which could homogeneously catalyze dehydration. In the literature, it has been shown that furfuryl aldehyde, furfuryl alcohol, and 5-hydroxymethyl furfural are prominent dehydration products from the fast pyrolysis of glucose, cellulose and hemicelluloses [30, 85]. In addition, Lourvanij et al. [86] reported that aqueous glucose can be dehydrated with acidic zeolites to yield 5-hydroxymethyl furfural.

Williams and Besler [87] also showed that glucose has two thermal decomposition peaks between 200 and 400°C using thermogravimetric analysis. However, these workers concluded glucose decomposes to a polymeric intermediate which then undergoes secondary degradation. Hence, two transitions are observed in the DTG at ~260 and 360 °C (for a heating rate of 40 °Cmin^{-1}). Further, Ramos-Sanchez et al. [88] reported the TGA in air of sugars including glucose. Glucose showed an onset temperature in the TGA at 192 °C with two weight losses at 227 and 321 °C.

When ZSM-5 is added to the reactor the temperatures at which the thermal decomposition reactions occur are lowered. From the visual observations, it can be seen that coke can be formed at low temperatures (<210°C) from the retro-aldol/Grob fragmentation products as well as at high temperatures from the dehydration products. However, coke formation is more favorable at low temperature since for pure glucose pyrolysis (Figure 4.1) as well as catalytic fast pyrolysis of glucose [25] coke yield is higher at low heating rates.

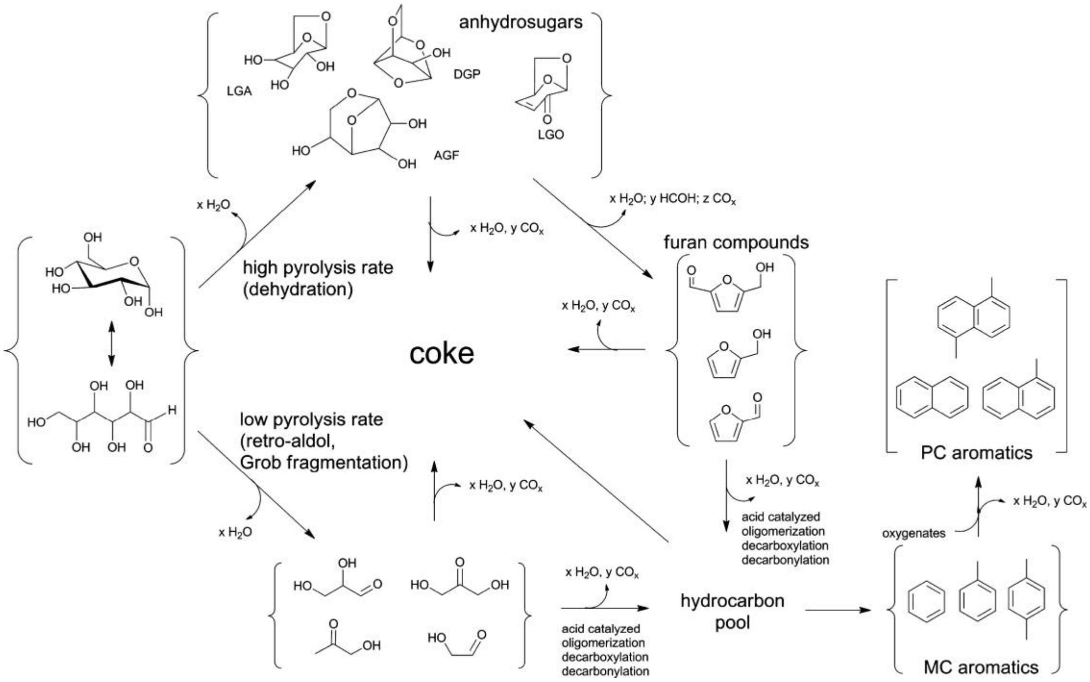

Figure 4.23 Reaction chemistry for the catalytic fast pyrolysis of glucose with ZSM-5.

4.4.2 Chemistry of Glucose Conversion to Aromatics

In this study, we showed that oxygenates produced from the thermal decomposition of glucose are intermediates in the conversion of glucose to aromatics. Furan, furfural, methyl-furan and furfuryl alcohol as well as acetic acid, are all converted to aromatics with similar selectivity under the same pyrolysis conditions (600 ℃ for 240 s). The pathway for conversion of the intermediate oxygenates to aromatics is shown in Figure 4.23. From the FTIR and pyroprobe reaction time results (Figures 4.8, 4.10 and 4.11), it can be seen that the formation of aromatics is the slow step in the reaction pathway. Glucose decomposes quickly in less than one second, while aromatic formation takes 2 min. To form aromatics, oxygenates diffuse into the ZSM-5 pores and through a series of decarbonylation, decarboxylation, dehydration, and oligomerization reactions form aromatics. It has been proposed that, for the conversion of methanol to aromatics with ZSM-5, the reaction proceeds through a common intermediate or "hydrocarbon pool" within the zeolite framework [70, 83-84, 89]. The methanol enters this hydrocarbon pool where it reacts with other hydrocarbons to form aromatics and olefins. The exact nature of this hydrocarbon pool has been the subject of much debate [89], but it is thought that the active species inside the hydrocarbon pool is a polymethylbenzene [70, 83-84]. The isotopic labeling studies (Section 4.3.6) suggest that similar hydrocarbon pool chemistry occurs during glucose conversion to aromatics over ZSM-5 [90].

The aromatic product selectivity (Figure 4.9) shifts from monocyclic aromatics to naphthalenes with increasing reaction time indicating that naphthalenes are probably formed from monocyclic aromatics in second series reaction. Monocyclic aromatics from the hydrocarbon pool can either leave the reactor as products or further react with another oxygenate to form polycyclic aromatics (Section 4.3.6).

The major competing reaction to the formation of aromatics is the formation of coke. It is likely that during CFP of glucose the intermediate furans polymerize to form resins, which further decompose to form coke on the catalyst. The acid-catalyzed dehydration polymerization of furfuryl alcohol has been well documented in the literature [80, 91-92]. The FTIR reaction time data (Figure 4.11, Table 4.5) shows at 3 s carbonyl species (band at 1711 cm^{-1}) are present. Various groups have identified 1710-1715 cm^{-1} as the characteristic band of the diketonic carbonyl present in furfuryl alcohol resins [80, 91-92].

These furan resins are probably coke precursors as the band at 1711 cm^{-1} is no longer present at long reaction times. Bertarione et al.[80] reported that the furfuryl alcohol resin is decomposed on the acidic zeolite HY when heated to 400 °C to form amorphous carbon. Our FTIR results also show that unsaturated carbon is present at long reaction times (bands at 1492, 1571 and 1589 cm^{-1}).

When compared to fresh catalyst, the coked catalyst pore volume is decreased significantly; however, with increasing coke levels there is no additional change in the pore volume. This initial decrease in pore volume is likely due to the formation of the hydrocarbon pool within the zeolite framework. Once the hydrocarbon pool is formed, additional carbon is deposited on the surface not within the pores. Several researchers studying the conversion of methanol to hydrocarbons (MTH) over ZSM-5 have reported that catalyst deactivation occurs from highly unsaturated coke on the external surface of the catalyst and not from large species within the pores [70, 93-94]. In contrast, larger caged zeolites such as HY and β-zeolite are mainly deactivated by the formation of polyaromatic species within the pore systems [83, 95]. The results herein suggest that the primary coking mechanism is the formation of oxygenate resins on the surface of the catalyst which ultimately decompose to unsaturated coke. However, from the results shown in Figure 4.20 and 21, the level of coke on the catalyst is not sufficiently high enough to cause deactivation as the aromatic yield increases with increasing coke level. Aho et al.[34] have shown for the pyrolysis of pine wood in the presence of ZSM-5 that further increasing the coke level on the catalyst to 16.3 wt.% leads to a significant decrease in catalytic activity.

4.5 Conclusions

The catalytic fast pyrolysis of glucose involves two steps. The first step involves the rapid thermal decomposition of glucose. Glucose decomposes through two different pathways. At low temperatures, glucose is decomposed to small oxygenates through retro-aldol condensation reactions. At high temperatures, glucose is dehydrated to form anhydrosugars and furans. Both decomposition pathways can occur homogenously or on catalyst active sites. Addition of ZSM-5 to the reactor lowers the temperature at which both the decomposition reactions occur. The second step in CFP is the formation of aromatics within the pores of the zeolite. This reaction step is far slower than the preceding thermal decomposition reactions. The oxygenates produced from thermal decomposition are likely the intermediates in the formation of aromatics because furans and acetic acid produce similar aromatic products under the same pyrolysis conditions (600 ℃ for 240 s). Isotopic labeling studies suggest three important routes for aromatic formation: 1) the monocyclic aromatic compounds are formed from random hydrocarbon fragments which are most likely produced from a hydrocarbon pool within the zeolite structure; 2) naphthalene is produced from two different steps with one step involving the combination of monocyclic aromatics with oxygenated fragments; 3) both benzene and naphthalene are susceptible to alkylation from the hydrocarbon pool, but the rate of alkylation of naphthalene is high and the rate of alkylation of benzene is low. The selectivity for the aromatic products is correlated to temperature and catalyst to feed ratio. The main competing reaction with aromatic production is the formation of unsaturated coke on the surface of the catalyst. Coke is formed through intermediate furan polymers, which ultimately decompose to unsaturated coke. To achieve maximum aromatic yields, pyrolysis should proceed with rapid decomposition of glucose to oxygenates to react with the catalyst. The concentration of oxygenates should remain low to avoid formation of coke and less desirable polycyclic aromatics.

CHAPTER 5

INVESTIGATION INTO THE SHAPE SELECTIVITY OF ZEOLITE CATALYSTS IN CATALYTIC FAST PYROLYSIS OF BIOMASS[3]

5.1 Introduction

Zeolites are solid acid catalysts having well defined microporous crystalline structures. Structurally, they consist of tetrahedral of silica where one oxygen of a given tetrahedron is shared with one of four others [96]. Acidity can be generated by isomorphic substitution of silicon with trivalent aluminum. To date, 180 structural types of zeolites, having different pore size, shape, dimensionality, and direction are available [97]. Due to the microporous nature of zeolites ranging from 5 Å to 12 Å, similar to molecular dimensions, they can act as shape selective catalysts [98]. For example, certain reactant molecules are excluded based on size relative to the zeolite pore size. Zeolites micropore shape selectivity and strong acidity allow them to be widely used as catalysts in many reactions in the petrochemical industry such as fluid catalytic cracking (FCC) and alkylation [99].

Shape selectivity is classically defined as being caused by either mass transfer [98, 100] or transition state effects [98, 101-102]. The different pore window size of zeolites ranging from 5 Å to 12 Å cause a mass transfer effect excluding certain reactant molecules based on size relative to the zeolite pore window size. In the similar manner, the zeolites limit the formation of larger products (i.e. high mass-transfer-limited products) than the

---

[3] The results in this chapter have been published in J. Jae, G.A. Tompsett, A.J. Foster, K.D. Hammond, S.M. Auerbach, R.F. Lobo and G.W. Huber, *J. Catal.* **2011**, *279*, 257-268.

pore size of them. Shape selectivity is also related to confined spaces within the pores (i.e. pore intersections). Such a confined space restricts certain transition states and influences the course of reaction. Zeolite chemistry can also be further complicated due to reactions on the exterior of the zeolite surface [103-104]. In addition zeolites can cause a “confinement effect”[105-106] or “solvent effect”[107] where the concentration of different reactants is higher inside the zeolite pores than in the gas phase.

To date, several researchers have studied zeolite catalysts for conversion of biomass into aromatics [20, 23, 25-26, 31, 33-35, 40, 108-116]. A range of zeolites have been tested including ZSM-5, Beta, Y-zeolite, mordenite, silicoaluminophosphate, and several mesoporous materials (Al-MCM-41, Al-MSU-F, and alumnia stabilized ceria MI-575) using a range of different feedstocks including bio-oils, glycerol, sorbitol, glucose, xylose, and biomass feedstocks. In general, these studies showed that addition of zeolites into the pyrolysis reactor could increase the formation of aromatics. Coke and CO were also formed during this process. The majority of these studies concluded that ZSM-5 was the catalyst that gave the highest yield of aromatics.

Although previous studies have tested a range of zeolites for biomass conversion the detailed relationship of the biomass molecular dimensions to zeolite pore size is not well understood. The role of pore size and shape on the catalytic chemistry must be better understood if improved zeolites are to be designed for biomass conversion. The objective of this study is to examine the influence of zeolite pore size and structure on the conversion of glucose to aromatics by catalytic fast pyrolysis. A range of zeolites, including small pore zeolites (ZK-5 and SAPO-34), medium pore zeolites (Ferrierite, ZSM-23, MCM-22, SSZ-20, ZSM-11, ZSM-5, IM-5, and TNU-9), and large pore zeolites(SSZ-55, beta, Y zeolite), were synthesized, characterized, and tested for catalytic fast pyrolysis of glucose. The kinetic diameters for the products and reactants were estimated from properties of the fluid at the critical point to determine whether the reactions occur inside the pores or on the external surface. The constraint index of zeolites is also used to compare the results with the different zeolite catalysts. The results from this study can be used to help understand if zeolite conversion of biomass derived molecules is caused by mass transfer effects, transitions state effects or external surface catalyzed reactions.

5.2 Experimental

The experimental methods and materials used for this work are described in Sections 2.1, 2.7, 2.8, and 2.11.

5.2.1 Zeolite Synthesis

ZSM-5 samples were synthesized using the organic free method reported by Kim et al. [117]. A precursor gel of colloidal silica, sodium aluminate, sodium hydroxide, and deionized water was prepared with composition (in terms of molar oxide ratios) of 10 Na_2O : 100 SiO_2 : 3.3 Al_2O_3 : 3000 H_2O. The precursor was stirred for 2 hr at room temperature, and then crystallized under autogenous pressure in a Parr Teflon-lined autoclave at 190℃ for 3 days.

MCM-22 samples were synthesized using the method reported by Corma et al. [118]. A precursor gel composed of fumed silica, sodium aluminate, sodium hydroxide, distilled water, and hexamethyleneimine (HME) with molar oxide composition of 8.9

Na_2O : 100 SiO_2 : 3.3 Al_2O_3: 4500 H_2O : 50 HME. The precursor solution stirred for 2 hours at room temperature followed by autoclaving at 150 ℃ for 7 days to crystallize the MCM-22 particles.

TNU-9 and IM-5 were synthesized using previously reported methods [119-120]. The 1,4 bis(N-methyl pyrrolidine) butane (MPB) structure directing agent was synthesized by the reaction of 1,4 dibromobutane with 1-methyl pyrrolidine in acetone. Similarly, 1,5 bis(N-methyl pyrrolidine) pentane (MPP) was synthesized via reaction of 1,5 dibromopentane with 1-methyl pyrrolidine in acetone. The purity of the products crystallized from this reactions was confirmed by ^1H and ^{13}C NMR performed on a Bruker AV400 spectrometer. Precursor solutions for the TNU-9 particles were prepared with a composition 37 Na_2O : 100 SiO_2 : 2.5 Al_2O_3 : 4000 H_2O : 15 MPB. The IM-5 precursor solution was prepared with a composition of 37 Na_2O : 100 SiO_2 : 2.5 Al_2O_3 : 4000 H_2O : 15 MPP. TNU-9 and IM-5 particles were crystallized by autoclaving their respective precursor solutions for 14 days at 160 ℃.

ZSM-11 was synthesized using tetrabutyl ammonium (TBA) as a structure-directing agent [121]. Potassium hydroxide was used in this synthesis to further suppress the formation of ZSM-5 intergrowths [122]. ZSM-11 precursor gels were prepared with molar oxide composition of 6.6 K_2O : 3.3 Na_2O : 100 SiO_2 : 3.3 Al_2O_3 : 4200 H_2O : 30 TBA. After stirring for 2 hr at room temperature, the precursor gels were autoclaved at 150 ℃ for 3 days to crystallize the ZSM-11 samples.

SAPO-34 was synthesized following protocols reported in the literature[123]. A precursor solution was prepared using 0.29 g of silica sol (Ludox HS-40, 40 wt.%, Aldrich), 0.36 g of phosphoric acid (85 wt.%, Aldrich), 0.28 g of a hydrated aluminum oxide (a pseudo-boehmite, 74.2 wt.% Al_2O_3, 25.8 wt.% H_2O), 0.69 g of triethylamine (TEA) (99.5 %, Aldrich), and 1.45 g of water. The composition of the final reaction mixture in molar oxide ratios was: 1.0 Al_2O_3 : 0.8 P_2O_5 : 1.0 SiO_2 : 3.5 TEA : 50 H_2O. The reaction mixture was crystallized at 180 ˚C under autogenous pressure for 24 h in the autoclave.

After synthesis, zeolite samples were washed with water and dried at 80 ℃. Samples were then calcined in air at 550 ℃ for 6 h to remove occluded organic molecules. Zeolite samples were ion-exchanged to the H^+ form by treatment in 0.1M NH_4NO_3 at 70 ℃ for 24 h followed by filtration, drying at 80 ℃, overnight and calcination under air at 550 ℃. ZK-5, ZSM-23, SSZ-20, and SSZ-55 samples were supplied by Stacey Zones, Chevron Research and Technology Company, Richmond, California, USA. Ferrierite (CP914C), zeolite Y (CBV 600), and zeolite Beta (CP 814C) were purchased from Zeolyst International, Conshohocken, PA.

Table 5.1 Physico-chemical properties of zeolites used in this study from the International Zeolite Association [97].

Zeolite	IZA code	SiO_2/Al_2O_3	Pore Dimension	Ring Size(Å)	Pore Size (Å)	CI index
ZK-5	KFI	5.5	3	8	3.9x3.9	>30[b]
SAPO-34	CHA	0.56[a]	3	8	4.3	33[124]
Ferririte	FER	20	2	8,10	3.5x4.8 4.2x5.4	4.5[125]
ZSM-23	MTT	160	1	10	4.5x5.2	10.6[126]
MCM-22	MWW	30	2	10	4.0x5.5 4.1x5.1	1.8[124]
SSZ-20	TON	90	1	10	4.6x5.7	6.9[126]
ZSM-11	MEL	30	3	10	5.3x5.4	8.7[127]
ZSM-5	MFI	30	3	10	5.1x5.5 5.3x5.6	6.9[126]
IM -5	IMF	40	3	10	5.5x5.6 5.3x5.4 5.3x5.9	1.8[128]
TNU-9	TUN	40	3	10	5.6x5.5 5.4x5.5	1.0-2.0[c]
β-zeolite	BEA	38	3	12	6.6x6.7 5.6x5.6	0.6-2.0 [129]
SSZ-55	ATS	54	1	12	6.5x7.25	1.0-2.0[d]
Y-zeolite	FAU	5.2	3	12	7.4x7.4	0.4[129]

[a] $SiO_2/(Al_2O_3+P_2O_5)$ in reactant gel
[b] Estimated from isomerization of n-butene to isobutene [130]
[c] Estimated from isomerization and disproportionation of *m*-xylene [119]
[d] Estimated from isomerization and disproportionation of *m*-xylene [131]

5.2.2 Characterization

Zeolite structures were characterized by powder X-ray diffraction as shown in Fig. 5.1. The intensity and peak positions of all of the zeolite samples are in good agreement with previously reported spectra [97, 118-120, 123]. However, TNU-9 shows some impurities and SAPO-34 shows weak peak intensity, indicating that it is less crystalline.

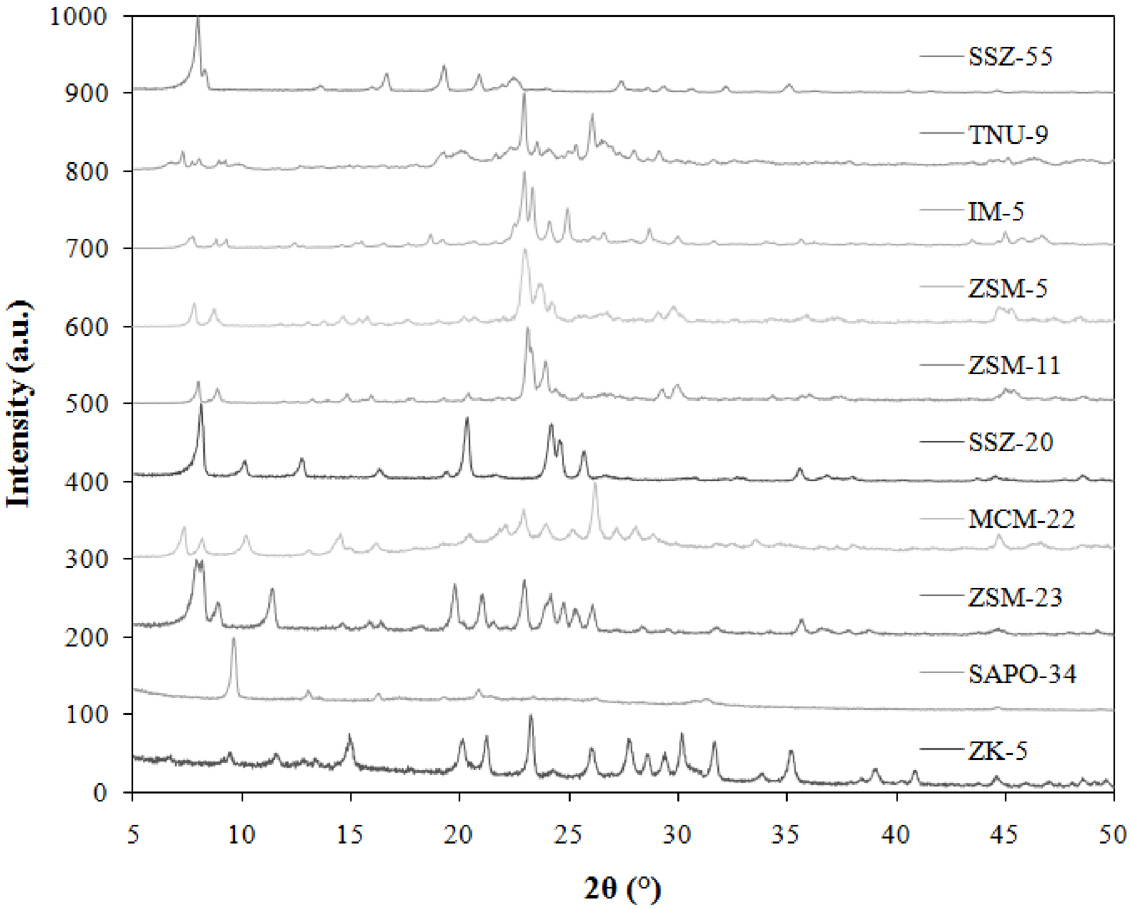

Figure 5.1 X-ray diffraction patterns of the zeolites used in this study

Scanning electron microscopy (SEM) was employed to characterize the morphology and crystal size of zeolite catalysts. The SEM images of each zeolite catalyst are shown in Fig. 5.2. ZK-5 and ZSM-23 have spherical crystals of ~ 0.4 µm while SSZ-20 and SSZ-55 have rod-like crystals of > 1µm. SAPO-34 has a well-defined cubic morphology with a relatively large crystal size of > 10µm. ZSM-5, IM-5, and TNU-9 all have rod-like crystals of < 0.5µm whereas MCM-22 and ZSM-11 have needle-like and rod-like crystal, respectively, with the broad range of crystal size (<1µm).

Physisorption experiments to characterize the porosity of the zeolites were performed. Fig. 5.3 shows N_2 adsorption-desorption isotherms for selected zeolite samples. For MCM-22, IM-5, and TNU-9, significant increase of adsorption in the range $p/p_0 > 0.8$ and hysteresis loops in the desorption branch were observed, indicating the presence of mesopores. Table 5.2 shows the calculated micropore and mesopore volumes, respectively, for selected zeolite samples. Significant mesopore volumes were observed for MCM-22, IM-5, and TNU-9.

The silica to alumina ratios (SAR) of the zeolites were determined by inductively coupled plasma (ICP) analysis performed by Galbraith Laboratories (Knoxville, TN). Most of the zeolites have the similar silica to alumina ratio between 20 and 50, as shown in Table 1. However, ZSM-23 (SiO_2/Al_2O_3=160) and SSZ-20 (SiO_2/Al_2O_3=90) were high-silica zeolites while ZK-5 (SiO_2/Al_2O_3=5.5) and Y zeolite (SiO_2/Al_2O_3=5.2) were high-alumina zeolites.

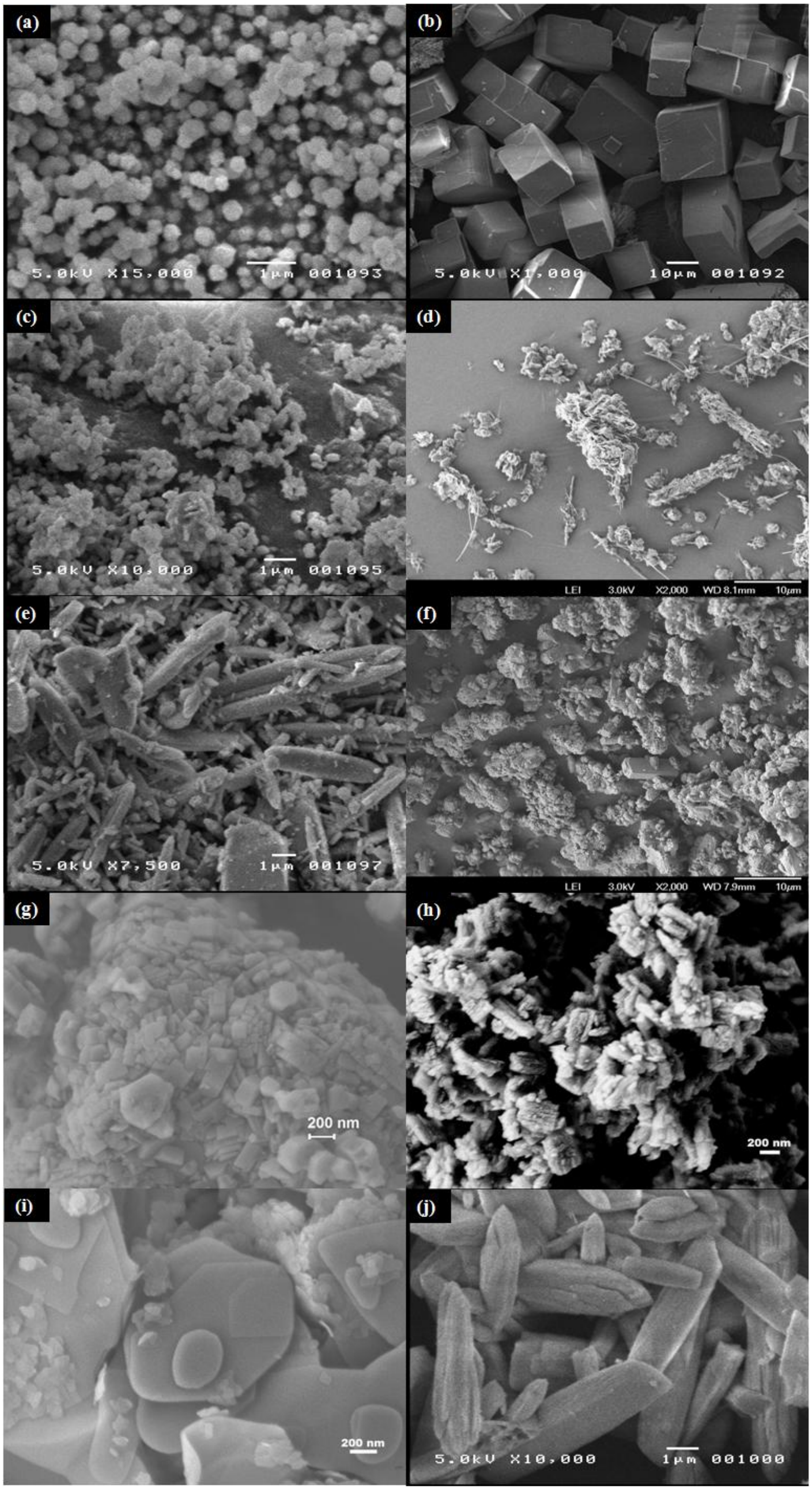

Figure 5.2 Scanning electron microscopy images of a) ZK-5, b) SAPO-34, C) ZSM-23, d) MCM-22, e) SSZ-20, f) ZSM-11, g) ZSM-5, h) IM-5, i) TNU-9, and j) SSZ-55.

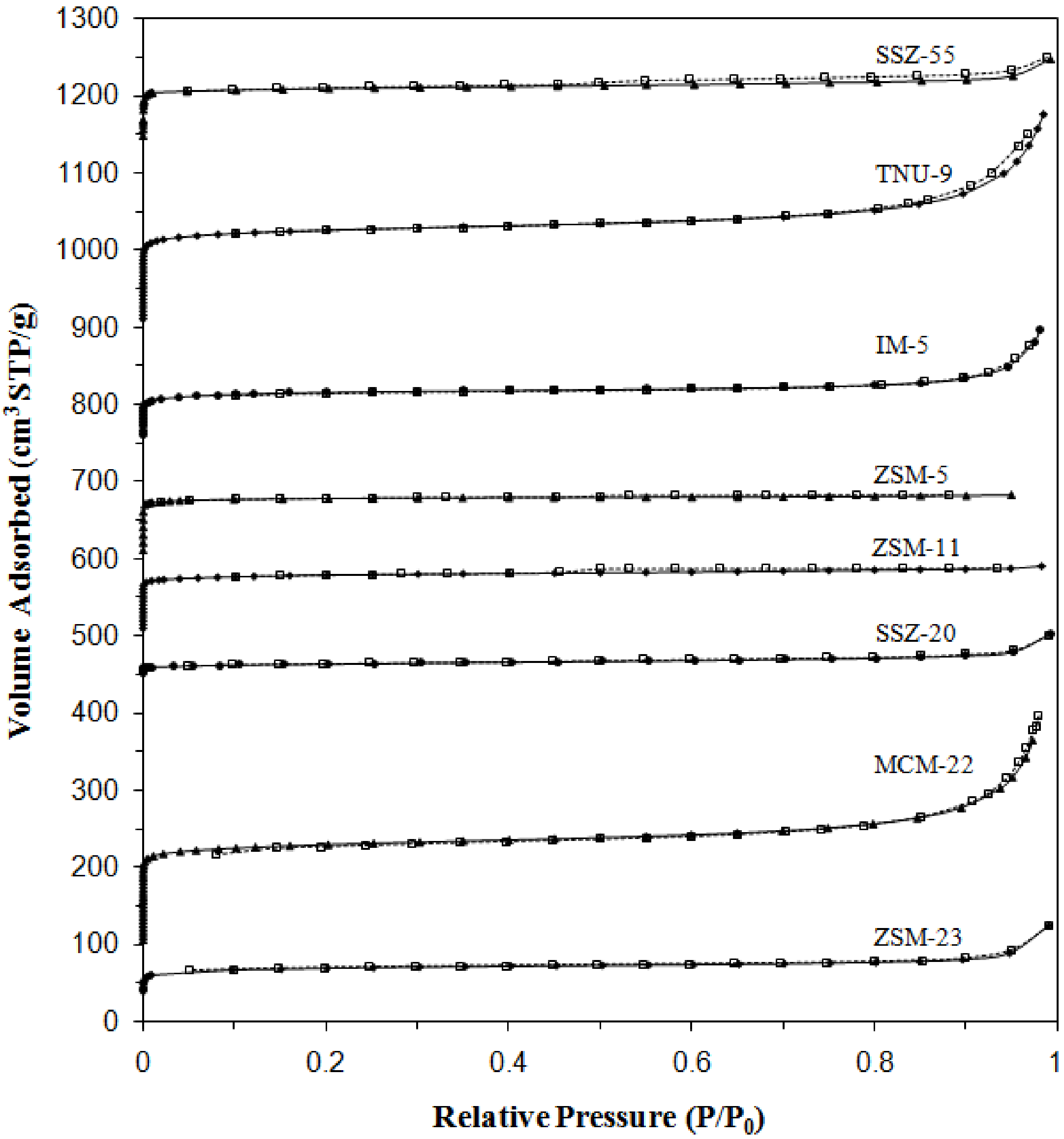

Figure 5.3 Nitrogen adsorption-desorption isotherms of selected zeolite catalysts.

Table 5.2 Micropore and mesopore volumes for the zeolites used in this study.

Zeolite	**V_{micro} (cm^3/g)**	**V_{meso} (cm^3/g)**
ZSM-23	0.086	0.09
MCM-22	0.16	0.31
SSZ-20	0.085	0.06
ZSM-11	0.12	0.07
ZSM-5	0.12	0.04
IM-5	0.16	0.15
TNU-9	0.15	0.28
SSZ-55	0.16	0.06

5.2.3 Determination of Kinetic Diameter of Selected Molecules

We define the critical diameter as the diameter of the smallest cylinder inside which the molecule will fit. The maximum diameter is defined as the longest dimension of the molecule. The kinetic diameter (σ) is estimated from the properties of the fluid at the critical point (c), shown in Eqs. (1) and (2) according to Bird et al. [132]:

$$\sigma = 0.841 V_c^{1/3} \qquad \text{Eq. (1)}$$

$$\sigma = 2.44 (T_c/p_c)^{1/3} \qquad \text{Eq. (2)}$$

where V_c is the critical volume in $cm^3 mol^{-1}$, T_c is the critical temperature in Kelvins and p_c is the critical pressure in atmospheres. Critical point data were obtained from the CRC Handbook [133], Yaws et al. [134], NIST [135] and Wang et al. [136].

The kinetic diameter has also been correlated with the molecular weight using Eq. (3) for aromatic hydrocarbons [136].

$$\sigma = 1.234 (M_W)^{1/3} \qquad \text{Eq. (3)}$$

where M_W is the molecular weight in g mol^{-1}. This kinetic diameter estimation assumes a spherical molecule, and hence the critical mass is related to the size of the sphere [136].

Molecular calculations in this article were performed with Gaussian ’03 [137] using density functional theory. Molecule geometries were optimized with the default (eigenvalue-following) optimization algorithm using the B3LYP hybrid functional [138-140] and the 6-31+G(*d*,*p*) basis set [141-144] to compute the energy. Critical diameters were computed as the internuclear distance between the two nuclei that intersected the surface of the smallest possible cylinder containing all nuclei plus an estimate of the van der Waals radii of the hydrogen (1.2 Å) or oxygen (1.52 Å) atoms involved. Molecule “lengths” were calculated as the distance between the two farthest-apart atoms along a line orthogonal to the critical diameter, plus an estimate of the atoms’ radii.

5.3 Results and Discussion

5.3.1 Kinetic Diameter vs Zeolite Pore Size

We have calculated the critical diameter (width), maximum diameter (length), and kinetic diameter of the biomass feedstocks, oxygenates, and aromatic products from catalytic fast pyrolysis of glucose as shown in Table 5.3. The data in Table 5.3 were determined from four sources: the literature, calculation from critical point data using Eqs. (1) and (2), estimation from the molecular weight correlation (Eq. (3)), and molecular calculation. The diameters can differ greatly depending on the source of the information and the calculation used. In general, the common literature values were used. Those calculated using Eqs. (1) and (2) were used when the literature values are not available. Eq.

(3) was used when critical point data are not available. Kinetic diameters calculated using the critical volume (Eq. (1)) can differ significantly from Eq. (2). For example, the kinetic diameter for formic acid is either 5.4 Å from critical temperature and pressure data or 4.0 Å using the critical volume. Formic acid forms dimers and this may contribute to the difference [145]. We have used the smaller diameter for the kinetic diameter of the organic acid products for this reason.

Table 5.3 Dimensions of lignocellulosic feedstocks and products from catalytic fast pyrolysis.

Molecule	Critical diameter (width) (Å)	Ref.	Maximum diameter (length) (Å)	Ref.	Kinetic diameter, σ (Å)	Ref.
Feedstocks						
α-D-glucose	8.417	[146]	8.583	[146]	8.6	[147]
β-D-glucose	8.503	[146]	8.615	[146]	8.6	[147]
Cellulose	~100 (microfibril)	[148]			8.6[a]	
Cellubiose	8.5[a]				8.6[a]	
Xylitol					6.6	Eqn. 3
Oxygenate Products (Catalyst-to-feed 1.5:1)						
Water	1.89	[135]			3.0, cluster >6.0	[149]
Carbon monoxide	3.28	[135]	3.339	[135]	3.59	[132]
Carbon dioxide	3.189	[135]	3.339	[135]	3.996	[132]
Acetic Acid	3.35	[135]			4.4	[149]
5-hydroxymethyl furfural (HMF)	5.9	[86]	9.3	[86]	6.2	Eqn. 3
	5.25 trans	Calc.[b]	8.64	Calc.[b]		
	5.48 cis	Calc.[b]	8.64	Calc.[b]		
Formic acid	4.6	[86]	4.6	[86]	4.0	Eqn. 1
Hydroxy Acetylaldehyde	3.88	[135]			4.8	Eqn. 3
furfural	4.56	Calc.[b]	5.99	Calc.[b]	5.5	Eqn. 2
2-methyl furan					5.3	Eqn. 1
Furan	4.27	[135]			5.1	Eqn. 1
4-methyl furfural					5.9	Eqn. 3
furan-2-methanol					5.7	Eqn. 3
Levoglucosan					6.7	Eqn. 3
Hydrocarbon Products (Catalyst-to-feed 19:1)						
Toluene	6.7	[150]	8.7	[150]	5.85	[151]
Benzene	6.7	[78]	7.4	[78]	5.85	[151]
Indane	6.8[c]				6.3	Eqn. 2
Indene					5.96	[136]
Trimethylbenzene	8.35	[78]	8.62	[78]		
1,3,5-TMB and	8.178	[152]			8.6	[153]
1,2,4-TMB	7.251	[152]			7.6	[154]
1,2,3-TMB	7.635	[152]			6.6	Eqn. 2
Ethyl benzene	6.7	[150]	9.2	[150]	6.0	[151] , Eqn. 1
2- Ethyl, toluene					6.6	Eqn. 2
3- Ethyl, toluene					6.6	Eqn. 2
4- Ethyl, toluene					6.6	Eqn. 2
p-Xylene	6.7	[150]	9.9	[150]	5.85	[151]
m-Xylene	7.4	[150]	9.2	[150]	6.80	[151]
o-Xylene	7.4	[150]	8.7	[150]	6.80	[151]
Naphthalene	6.8	[78]	9.1	[78]	6.2	[136], Eqn. 1
1-methyl naphthalene	7.65	[155]			6.8	Eqn. 2
1,5-dimethylnaphthalene					7.7	[156]
1,6-dimethylnaphthalene					7.7	[156]
2,6-dimethylnaphthalene					7.2	[156]
anthracene	6.8	[78]	12.1	[78]	6.96	[136]
pyrene	7.36	[157]	9.80	[157]	7.24	[136]
phenanthrene					6.96	[136]

[a] Estimated from glucose

[b] From Gaussian Calculation

[c] Estimated from naphthalene

The correlation between kinetic diameter and molecular weight is plotted in Figure 5.4. The curve from the empirical relationship in Eq. (3) is also plotted in Figure 5.4 for comparison to the literature values for oxygenates. In general, there is good agreement

(<2% average difference) between the literature values of kinetic diameter and the empirical correlation determined by Wang et al. [136] (Eq. (3)), particularly for furan derivatives. This suggests that using this approximation method for the kinetic diameters of oxygenate molecules which do not have critical properties in the literature is reasonable. The molecular weight does not, however, give any indication of the structure of the molecule, and this correlation may differ for different types of structures such as carbohydrates.

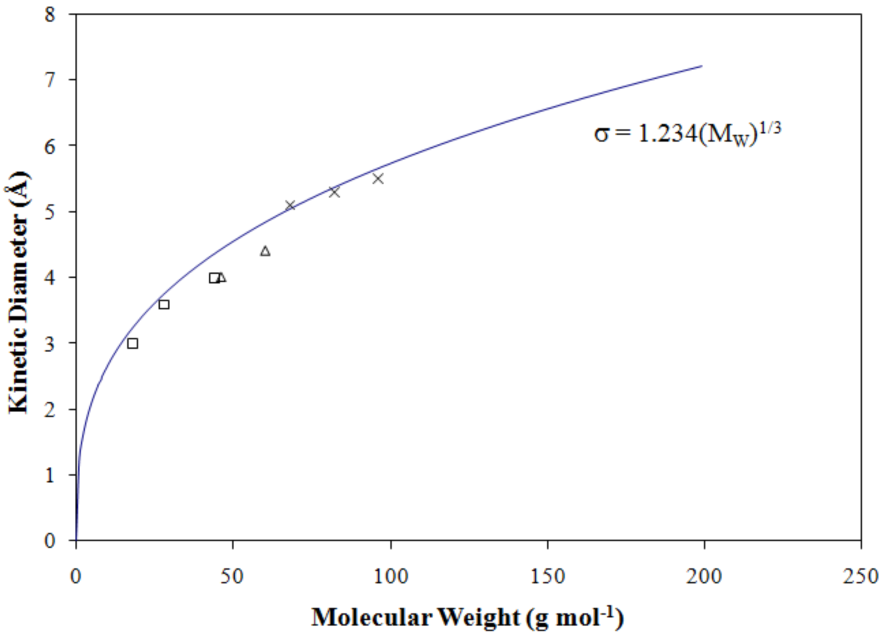

Figure 5.4 Correlation between kinetic diameter and molecular weight for oxygenate molecules. □: small molecules; H_2O, CO and CO_2, Δ: organic acids; formic acid and acetic acid, and x: furan derivatives; furan, methyl furan and furfural. The solid curve is a fit using Eq. (3).

The pore sizes of zeolite catalysts are typically given as the crystallographic diameters based on atomic radii, e.g., 5.5—5.6 Å for ZSM-5. Cook and Conner [79] have shown, however, that pore diameters calculated using Norman radii for the Si and O atoms are 0.7 Å larger than those calculated with atomic radii, consistent with the diffusion of molecules of larger diameter than the crystallographic diameter reported, such as cyclohexane diffusion in silicalite. The maximum pore diameters of different zeolites, using atomic radii and the Norman radii corrections, are shown in Table 5.4.

Table 5.4 Maximum pore diameters for different zeolites [97].

Zeolites	Maximum Pore Diameter (Atomic Radii) d_A (Å)	Maximum Pore Diameter (Norman Radii) d_N (Å)
SAPO-34	4.3	5.0
MCM-22	5.5	6.2
ZSM-5	5.5 and 5.6	6.2 and 6.3
Beta	6.7 and 5.6	7.4 and 6.3
Y zeolite	7.4	8.1

Figure 5.5 shows the kinetic diameters of the feedstock (glucose), the oxygenated products, and aromatic products from catalytic fast pyrolysis of glucose on the same scale as the zeolite pore sizes. The Norman radii adjusted pore sizes are used in this figure to adequately compare the zeolite pore size with the kinetic diameter of the molecules. In the case of zeolites with two different pore sizes, the larger pore sizes were chosen. As shown on this figure, glucose is significantly larger than the maximum pore size of ZSM-5 (6.3 Å); it therefore would not be expected to diffuse into the zeolite before decomposition. However, the decomposition of glucose occurs very rapidly (<1 s) at 600°C [158] and therefore the diffuse of the pyrolysis products is of more relevance. The pyrolysis products of glucose include levoglucosan, hydroxyacetaldehyde, and glyceraldehyde. These pyrolysis products, with the exception of levoglucosan, are significantly smaller than the ZSM-5 pore. Levoglucosan can also undergo dehydration reaction to produce smaller products than the pore size of ZSM-5. This suggests that these products can easily diffuse into the zeolite pores and suggests that reactions of these molecules within the ZSM-5 are reactions within the zeolite pores.

Aromatic hydrocarbons are the predominant products along with CO, CO_2, and coke, from the catalytic fast pyrolysis of glucose. From Figure 5.5 it can be seen that, benzene, toluene, naphthalene, indene, indane, ethylbenzene and *p*-xylenes are sufficiently small to diffuse into the ZSM-5 pores. The larger aromatic product molecules including 1,5-dimethylnaphthalene and 1,3,5-trimethyl benzene are most likely formed on the catalyst surface, either directly or by processes such as secondary alkylation of the smaller aromatics.

Naphthalene is the aromatic molecule made in the highest yield from catalytic fast pyrolysis of glucose in the pyroprobe reactor [26]. It is known that this polyaromatics has very slow diffusion in ZSM-5 [26] and it might be speculated that naphthalene is not formed within the pores. Indeed, naphthalene has a kinetic diameter (~6.2 Å [78]) very close to the pore diameter of ZSM-5 (~6.3 Å with Norman radii adjustment [79]). However, at the elevated reaction temperature (600˚C), the energetic barrier to diffusion is likely to be decreased making the zeolites more flexible. Hence, it is possible that naphthalene is formed within the pores as well as on the surface.

Figure 5.5 also suggests that zeolites with pore size diameters smaller than 5 Å (8MR ring zeolite, small pore) will predominantly have surface reactions. Larger pore zeolites with pore diameters larger than 7.2 Å (12MR ring zeolite, large pore) will allow all the oxygenates to easily diffuse into the zeolite. These large pore zeolites will primarily have pore reactions.

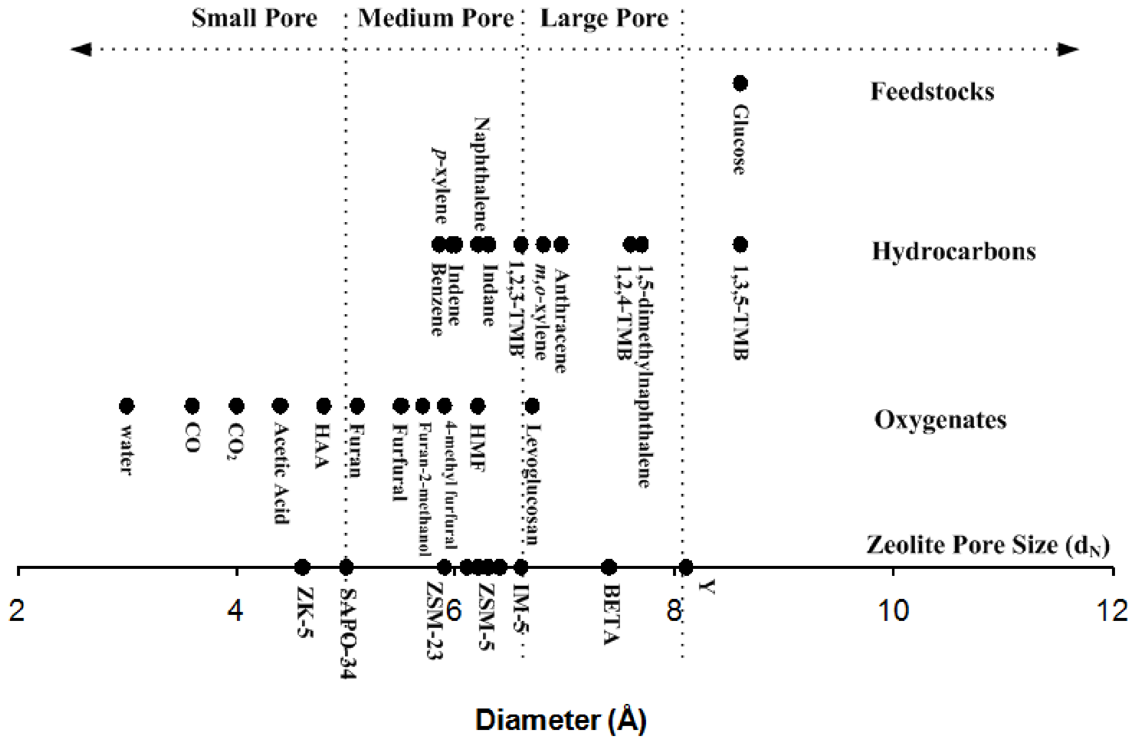

Figure 5.5 Schematic of zeolite pore diameter (d_N) compared to the kinetic diameter of feedstocks, and oxygenate and hydrocarbon catalytic pyrolysis products.

5.3.2 Catalytic Fast Pyrolysis of Glucose

The aromatic yield is a strong function of average pore size for the CFP of glucose as shown in Figure 5.6. The yield goes through a maximum with the average pore size of the zeolite between 5.3 and 5.5 Å. Small pore zeolites, such as ZK-5 and SAPO-34, produced primarily oxygenated species formed from the pyrolysis of glucose, char, CO and CO_2. These small pore zeolites are widely used for methanol to olefin conversion [89] and their small pore sizes, 3.9 to 4.3 Å do not produce aromatics. Aromatics were produced mainly in the medium pore (10—membered—ring) zeolites, including MCM-22, ZSM-23, SSZ-20, ZSM-11, ZSM-5, IM-5, and TNU-9. All of these zeolites have an effective pore size of 5.2 to 5.9 Å. Ferrierite (intersecting 8 and 10 ring pore systems) produced primarily oxygenates with low yields of aromatic hydrocarbons. It appears that the 8-membered ring (3.5 × 4.8 Å) pore slows down the overall diffusion rate and inhibits aromatics formation. SSZ-20 and ZSM-23 (one dimensional pore systems) produced moderate yields of aromatic hydrocarbon with high yields of oxygenates. Molecular diffusion inside these one-dimensional pores is more limited than multi-dimensional pores. In addition, these zeolites have high silica to alumina ratio (90 and 160, respectively), which can also impact the catalyst selectivity. Hence, production of the intermediate oxygenate species could be favored. Oxygenates are not produced in the other multi-dimensional 10 ring pore zeolites. Large pore zeolites including Beta zeolite, SSZ-55, and Y-zeolite produced aromatics; however, the aromatic yield was low and coke was the major product. Thus, large pores also produce high coke yields.

The maximum aromatic yield of 35% was obtained from ZSM-5, a zeolite with an intersecting 10-membered ring pore system composed of straight (5.3 × 5.6 Å) and sinusoidal (5.1 × 5.5 Å) channels. ZSM-11, formed of two intersecting straight channels (5.3 × 5.4 Å), shows an aromatic yield of 25%. However, MCM-22, TNU-9, and IM-5 show relatively low aromatic yields even though their pore sizes, pore dimensionality, and silica to alumina ratio are similar to ZSM-5 and ZSM-11. As shown in Table 5.2, these zeolites have high mesopore volumes created by inter-crystalline space, compared to ZSM-5 and ZSM-11. This suggests that these mesopores act as large pores, facilitating the formation of coke.

Further insights into the differences in the reactivity of medium pore zeolites can be obtained from the size of internal pore space (i.e., pore intersections). As shown in Table 5.1, MCM-22 and TNU-9 have large internal pore spaces of 9.69 Å and 8.46 Å, respectively, compared to that of ZSM-5 (6.36 Å) and ZSM-11 (7.72 Å). Thus, these results suggest that, in addition to pore window size, the steric hindrance of reacting molecules inside zeolite pores plays a role in this reaction. This also suggests that biomass conversion into aromatics with zeolites is a reaction where there are both mass transfer and transition state effects within the zeolite.

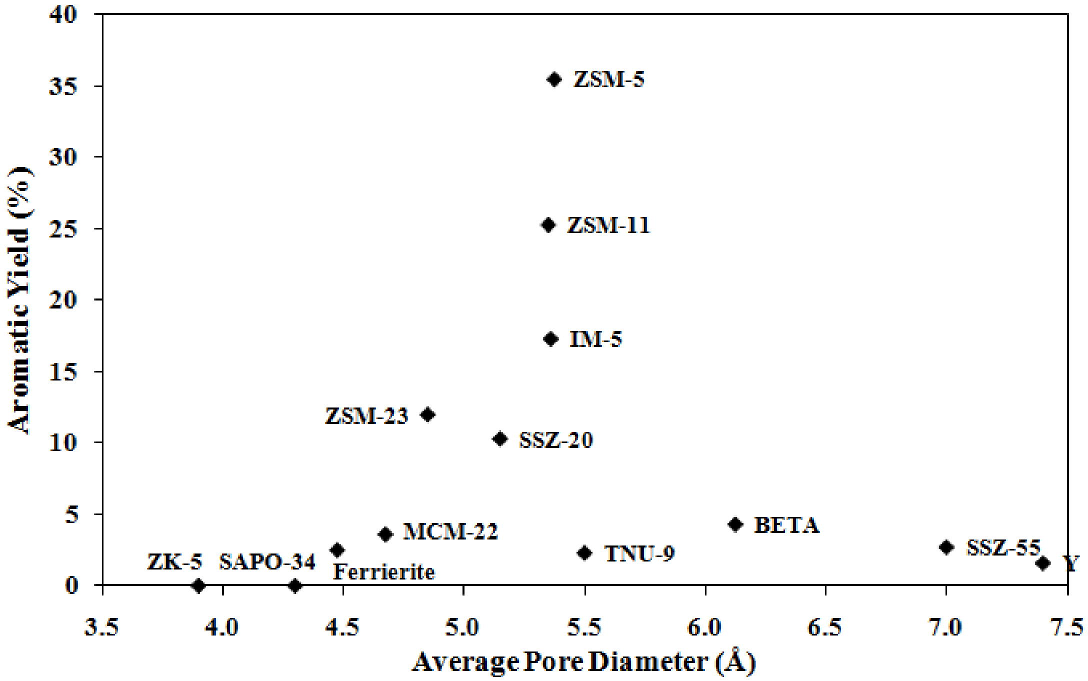

Figure 5.6 Aromatic yields as a function of average pore diameter for different zeolites for catalytic fast pyrolysis of glucose. Reaction conditions: catalyst to feed weight ratio = 19, nominal heating rate 1000℃ s^{-1}, reaction time 240 s.

Tables 5.5 shows the carbon yield of these reactions. Table 5.6 and 5.7 show the product distributions of aromatics and oxygenated species, respectively. The major glucose pyrolysis product is levoglucosan (LGA, 1,6-anhydro-β-D-glucopyranose, $C_6H_{10}O_5$), which is the dehydrated product of glucose [158]. Other anhydrosugars, including levoglucosenone (LGO, 6,8-dioxabicyclo[3.2.1]oct-2-en-4-one, $C_6H_6O_3$), 1,4:3,6-

dianhydro-β-D-glucopyranose (DGP, $C_6H_8O_4$), and 1,6-anhydro-β-d-glucofuranose (AGF, $C_6H_{10}O_5$) are present in lower amounts. However, as shown in Table 5.7, levoglucosenone and furfural becomes the major products among produced oxygenate species for ZK-5 and SAPO-34. This suggests that levoglucosan is further dehydrated by surface catalyzed reaction because these small pore zeolites do not allow any oxygenate species to diffuse into the pore. Moreover, levoglucosan was only dominant for ZSM-23 (SiO_2/Al2O_3=160), the high silica catalyst. In ZSM-23, the surface acid sites have relatively low concentration, and this could minimize the surface catalyzed reaction. Hence, this oxygenate distribution combined with the kinetic diameter estimation clearly shows the role of surface reaction in catalyst fast pyrolysis of glucose.

The gaseous products are CO and CO_2 for all the catalysts, as shown in Table 5.5. These gaseous product yields increased with increasing aromatic yield. In order to produce aromatics, oxygen for the intermediate pyrolysis products has to be removed by CO, CO_2, and water. Hence, the small pore zeolite (no aromatic production) produced relatively low CO and CO_2 yield compared to medium pore and large pore zeolites. Especially, CO and CO_2 yields are remarkably high for IM-5, ZSM-11, and ZSM-5 which produce high aromatic yield.

As shown in Table 5.6, the major aromatic products are naphthalenes(N), toluene(T), xylenes(X), and benzene(B) for all of the catalysts. The aromatic distribution was a function of zeolite type. However, aromatic distribution was not a simple function of zeolite pore. For one-dimensional zeolite such as ZSM-23, SSZ-20, and SSZ-55, naphthalene selectivity increased with increasing the pore size of zeolite (24.9%, 38.3%, and 47.2%). On the other hand, the opposite trend was observed for multi-dimensional zeolites. Large pore zeolites such as Beta and Y-zeolite showed relatively low naphthalene selectivity and high BTX selectivity compared to medium pore zeolites even though their large pores can facilitate the production of larger aromatic molecules. Interestingly, aromatic distribution of medium pore TNU-9 was similar to large pore zeolites. This aromatic distribution results suggest that the internal pore architecture of zeolite plays a significant role on the reaction chemistry.

Table 5.5 Carbon yields (%) for catalytic fast pyrolysis of glucose with different zeolites. Reaction conditions: catalyst to feed weight ratio = 19, nominal heating rate 1000℃ s^{-1}, reaction time 240 s.

Zeolite	**Aromatics**	**Oxygenates**	**CO_2**	**CO**	**Coke**	**Unidentified***	**Total Carbon**
ZK-5	0.0	14.1	4.3	8.7	55.1	17.8	100.0
SAPO-34	0.0	30.0	3.2	7.7	34.7	24.4	100.0
Ferrierite	2.5	14.1	4.4	11.6	48.0	19.4	100.0
ZSM-23	12.0	12.7	4.8	10.5	40.8	19.2	100.0
MCM-22	3.6	0	10	26	63	-	102
SSZ-20	10.3	18.0	4.1	9.7	43.1	14.8	100.0
ZSM-11	25.3	0	11.0	24.9	44.7	-	106
ZSM-5	35.5	0	8.9	23.3	30.4	-	98.1
IM-5	17.3	0	10	28	48.5	-	103.8
TNU-9	2.3	0	5.6	15.9	66.8	9.4	90.6
β-zeolite	4.3	<1	10.5	7.8	67.0	10.4	89.6
SSZ-55	2.7	<1	3.7	14.1	83.7	-	104.2
Y-zeolite	1.6	<1	3.9	13.4	84.9	-	103.8

*Unidentified includes unidentified oxygenate species in GC-MS and missing carbon.

Table 5.6 Aromatic product selectivity for catalytic fast pyrolysis of glucose with different zeolites. Reaction conditions: catalyst to feed weight ratio 19, nominal heating rate 1000℃ s^{-1}, reaction time 240 s. Abbreviations: Ben.= benzene, Tol.= toluene, E-Ben.= ethyl-benzene, Xyl.= xylenes, M,E-Ben.=methyl-ethyl-benzene, Tm-Ben.=trimethylbenzene, Ph.=Phenols, Ind.=indanes, Nap.=naphthalenes. Others include ethyl-dimethyl-benzene and methyl-propenyl-benzene.

	Aromatic Selectivity (%)							
Catalyst	Ben.	Tol.	E-Ben. Xyl.	M,E-Benz. Tm-Benz.	Ph.	Ind.	Naph.	Others
ZK-5	-	-	-	-	-	-	-	-
SAPO-34	-	-	-	-	-	-	-	-
Ferrierite	3.1	18.4	8.2	0.0	14.2	4.6	51.6	0.0
ZSM-23	10.6	25.8	19.3	6.2	3.8	6.9	24.9	2.4
MCM-22	29.4	25.2	10.2	0.0	0.0	0.0	35.1	0.0
SSZ-20	7.3	23.1	16.8	5.4	1.3	8.0	38.3	0.0
ZSM -11	14.2	27.1	17.3	1.5	2.5	4.4	32.6	0.4
ZSM-5	12.8	18.5	12.9	2.6	0.1	2.2	50.7	0.3
IM-5	17.4	25.4	11.4	3.2	0.4	0.7	41.5	0.0
TNU-9	31.9	40.0	11.1	0.0	0.0	0.0	16.9	0.0
β-zeolite	30.9	34.7	13.4	0.9	0.0	0.0	20.1	0.0
SSZ-55	13.3	27.9	9.1	1.2	1.3	0.0	47.2	0.0
Y-zeolite	20.6	31.0	12.5	1.6	5.3	0.0	29.1	0.0

Table 5.7 Oxygenated product selectivity for catalytic fast pyrolysis of glucose with different zeolites. Reaction conditions: catalyst to feed weight ratio 19, nominal heating rate 1000℃ s^{-1}, reaction time 240 s.

Oxygenate Selectivity (%)	Catalyst				
	ZK-5	SAPO-34	Ferrierite	ZSM-23	SSZ-20
Acetic Acid	0.0	1.5	0.0	20.4	8.1
4-methyl-2,3-dihydrofuran	10.1	12.3	9.6	8.5	12.3
Furfural	40.0	23.7	30.6	5.0	13.1
5-methyl furfural	3.0	4.1	2.0	0.0	0.0
2-furanmethanol	1.7	2.8	1.4	0.9	1.9
Furancarboxylic acid, methyl ester	1.6	2.6	1.1	0.0	2.5
5-methyl-2(5H)-Furanone	0.6	0.7	0.8	0.0	1.0
5-hydroxymethyl furfural	1.5	11.5	0.0	0.0	0.0
Isomaltol	0.7	1.3	0.0	0.0	0.7
Ethanone, 1-(2-furanyl)-	1.2	1.6	0.0	0.0	0.0
2-hydroxymethylene-tetrahydrofuran-3-one	2.5	2.8	1.1	0.0	3.0
1,4:3,6-dianhydro-alpha-d-glucopyranose	5.8	12.6	10.1	9.0	8.9
1,6-anhydro-beta-D-glucopyranose (Levoglucosan)	5.0	0.0	0.0	22.9	0.0
Levoglucosenone	26.3	22.5	43.2	33.7	48.4

5.3.3 Aromatic Yields as a Function of Constraint Index

The constraint index (CI) is a widely used concept to investigate the shape selectivity of zeolites [159]. It is defined as the ratio of the observed cracking rate constants of n-hexane to 3-methylpentane; a higher CI value thus indicates a larger steric hindrance and a lower CI value indicates the absence of steric hindrance. Figure 5.7 shows the aromatic yield as a function of constraint index. It was found that the medium pore zeolites with moderate CI values produce high aromatic yield. IM-5 and TNU-9 have low CI values of 1.8 and 1.0—2.0 compared to the 6.9 of ZSM-5. Hence, a low CI index (less steric hindrance) is not preferable for aromatic formation. Notably, ZSM-23 and SSZ-20, CI values of 10.6 and 6.9, respectively, show higher aromatic yields than the zeolites with low CI values (except IM-5). It is also remarkable that TNU-9 and MCM-22 produced significant amounts of coke (66.8% and 63%) along with aromatics, behaving like large pore zeolites. This can be explained by the presence of the cages inside the zeolite pores (i.e., the effect of pore intersections). MCM-22 and TNU-9 have large cylindrical pore intersections (7.1Å) and large cavities accessible through 10 ring pore window, respectively [119]. Thus, we believe that these cages inside the zeolite channels can provide the space needed for coke formation. Carpenter et al. [160] also showed that the presence of a large cage can contribute to the low CI values and fast deactivation of zeolite by providing more void space.

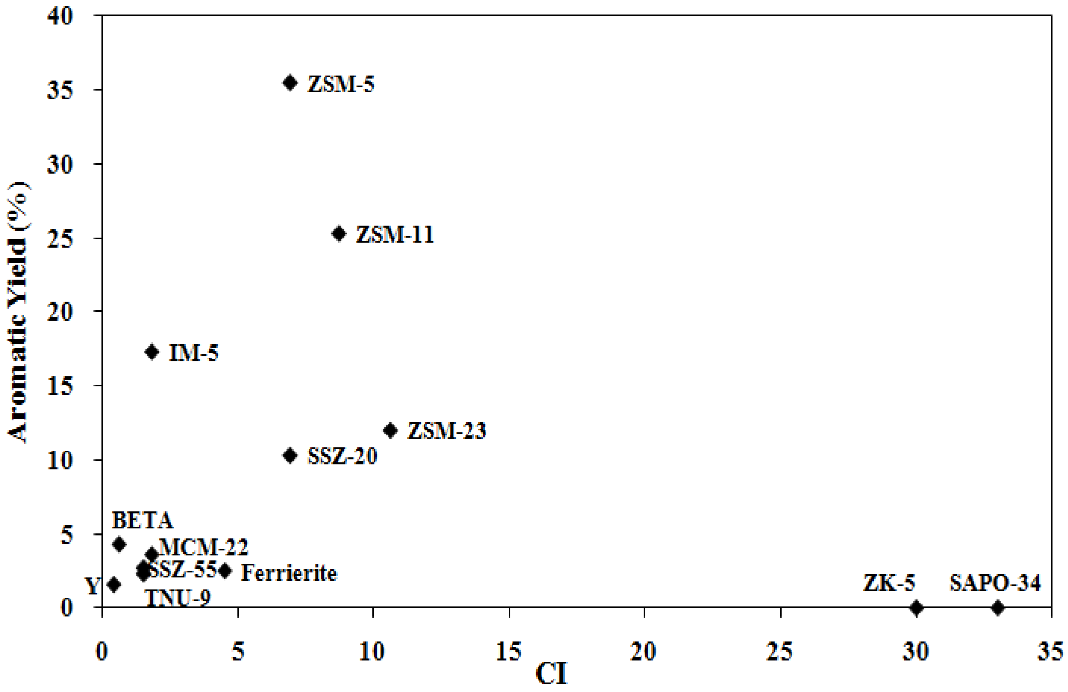

Figure 5.7 Aromatic yields versus the constraint index

5.3.4 Design of Zeolite Catalysts for Conversion of Biomass-derived Oxygenates into Aromatics

The results in this study can be used to design new zeolite catalyst for conversion of biomass-derived oxygenates into aromatics. The reaction for conversion of biomass-derived molecules into aromatics is a shape selective reaction where the shape selectivity effect is caused by both mass transfer effects, linked to pore window size of zeolite, and transition state effects, related to the internal void space of zeolites. The external surface acid sites also contribute to the dehydration of pyrolysis product to smaller oxygentates and production of larger aromatic molecules which are less valuable products. Based on our results, ZSM-5 is the optimal zeolite structure having the ideal pore size and internal pore space for biomass conversion. ZSM-5 can be further modified to improve its catalytic properties. The mass transfer effects can be varied by changing the crystallite size of ZSM-5. Small crystallite size of ZSM-5 might be beneficial by enhancing diffusion of molecules within the catalyst and creating high surface area for access of molecules into acid sites. Alternatively, recent advance in hierarchical zeolite synthesis allows us to introduce mesoporosity into ZSM-5 framework [161-164]. Carefully designed mesoporous ZSM-5 might have benefits of enhanced mass transfer and transformation of bulky molecules through the mesoporosity. Tranisition state effect can be adjusted by incorporating different types of sites preferentially within the ZSM-5. These sites located inside ZSM-5 pores can provide new active sites for reaction (e.g. hydrogenation) and enhanced steric hindrance. In addition, the surface acid sites of ZSM-5 can be tuned to decrease the secondary reaction on the catalyst surface. Decreasing the exterior surface acidity by dealumination or silylating agent treatment might reduce formation of the undesired larger aromatic molecules. As suggested in this paper, the catalytic properties of ZSM-5 can be optimized in many ways. Proper tuning of each parameter can offer highly selective zeolite catalysts for conversion of biomass-derived oxygenates into aromatics.

5.4 Conclusions

We studied the influence of zeolite pore size and shape selectivity on the conversion of glucose to aromatics by catalytic fast pyrolysis. We first estimated the kinetic diameters for the reactants and products to determine whether the reactions occur inside the pores or at external surface sites for the different zeolite catalysts. This analysis showed that the aromatic products and the majority of the reactants can fit inside the zeolite pores of most of the medium and large pore zeolites. However, in some of the smaller pore zeolites the polycyclic aromatics may form by secondary reactions on the catalyst surface, either directly or via reaction of the smaller aromatics. Zeolites having a wide range of pore size and shape (small pore ZK-5, SAPO-34, medium pore Ferrierite, ZSM-23, MCM-22, SSZ-20, ZSM-11, ZSM-5, IM-5, TNU-9, and large pore SSZ-55, Beta-zeolite, Y-zeolite) were tested in a pyroprobe reactor for the conversion of glucose to aromatics. The aromatic yield was a function of the pore size of the zeolite catalyst. Small pore zeolites did not produce any aromatics with oxygenated products (from pyrolysis of glucose), CO, CO_2 and coke as the major products. Aromatic yields were highest in the medium pore zeolites with pore sizes in the range of 5.2 to 5.9 Å. High coke yield, low aromatic yields, and low oxygenate yields were observed with large pore zeolites, suggesting that the large pores facilitate the formation of coke. In addition to pore window size, internal pore space and steric hindrance play a determining role for aromatic production. Medium pore zeolites with moderate internal pore space and steric hindrance (ZSM-5 and ZSM-11) have the highest aromatic yield and the least amount of coke.

CHAPTER 6

OPTIMIZATION OF ZSM-5 BASED CATALYSTS FOR CATALYTIC FAST PYROLYSIS OF BIOMASS[4]

6.1 Introduction

The main drawback in the CFP process is the low yield of aromatic hydrocarbons (up to 30% carbon) and high yield of undesired coke (up to 30% carbon). As seen in the chapter 5, ZSM-5 is the most effective catalyst for the conversion of biomass into aromatics. Thus, the objective of this study is to “tune” the ZSM-5 catalyst properties to optimize aromatic production in the CFP process. ZSM-5 can be synthesized under a wide range of different conditions, giving rise to different crystal sizes, morphologies, and elemental compositions. Indeed, recent advances in hierarchical zeolite synthesis allow us to tailor mesopore structure to ZSM-5. This flexibility allows for an effort to study some of the factors affecting the aromatic yield from CFP of biomass in more detail in order to develop a better ZSM-5-based catalyst.

One simple method to increase the yield towards aromatics may be to increase the density of available catalytic sites. However, as more aluminum is incorporated into the zeolite framework, the zeolite will become more hydrophilic[165] and the appearance of closely located Brønsted acid sites may have an effect on the catalytic chemistry within the zeolite. This suggests that an optimum silica-to-alumina ratio (SAR) may exist for this reaction. Another strategy is to improve the diffusion characteristics of the catalysts. This

---

[4] The results in this chapter have been published in A.J. Foster, J. Jae, Y.-T. Cheng, G.W. Huber and R.F. Lobo, *Applied Catalysis, A: General* **under review**; Y.-T. Cheng, J. Jae, J. Shi, W. Fan and G.W. Huber, *Angew. Chem.-Int. Edit.* **in-press**

may be accomplished by either decreasing the size of the zeolite particles or by creating hierarchical mesopores within the zeolite framework [166]. Because the catalytic conversion of biomass pyrolysis products is likely limited by diffusion into the micropores, any improvement in the accessibility to micropore openings will have a positive effect on the ability of the zeolites to catalyze the desired reactions. As a side effect, the increased surface area will also lead to an increase in the number of external surface acid sites.

Since reactions confined within the zeolite micropores benefit from shape-selectivity, they are likely the key sites for the formation of monoaromatic species. Acid sites on external particle surfaces may have different activity and selectivity than the micropore sites [167]. Selectively deactivating these external sites makes it possible to study their role in catalytic fast pyrolysis. Deactivation can be accomplished by using a silylating agent to make the sites inaccessible or by selective leaching from the zeolite surface using an acid treatment.

The other approach is to incorporate metal into the ZSM-5 structure as sites to create new type of bifunctional catalyst. Metal can be loaded into ZSM-5 catalyst by post-synthesis methods such as ion exchange and incipient wetness, or isomorphous metal substitution in the ZSM-5 framework. Several researchers have shown that Ga promoted ZSM-5 is a highly active catalyst for aromatic production from alkanes [168-173] and pyrolysis vapors [19, 39]. Because CFP of biomass produces high yield of olefins such as ethylene and propylene in a fluidized bed reactor, Ga promoted ZSM-5 could produce more aromatics via conversion of olefin species to aromatics. As we will show in this chapter, Ga/ZSM-5 is a promising catalyst, producing 40% more aromatics than ZSM-5 for CFP of biomass.

We will systematically study the effects of 1) varying the ZSM-5 bulk silica-to-alumina ratio, 2) changing the particle size, 3) tailoring hierarchical mesopores, 4) removing external acid sites, 5) incorporating Ga into the ZSM-5 structure, on the CFP of glucose, furan, and maple/pine wood in the pyroprobe, fixed bed, and fluidized bed reactors. Each of these modifications can alter both the yield and selectivity of aromatic products from CFP of biomass. Understanding the impact of these factors will help us design more active catalysts for the conversion of biomass into aromatics.

6.2 Experimental

The experimental methods and materials used for this work are described in Sections 2.1, 2.2, 2.3, 2.5, 2.7, 2.8, 2.9, 2.10, and 2.11.

6.2.1 Zeolite Synthesis

Mesoporous ZSM-5 (MesZSM-5) was synthesized using the surfactant-mediated method reported by Ryoo et al. [174-175]. Tetraethyl orthosilicate, tetrapropylammonium bromide, sodium hydroxide and deionized water were combined and stirred for 1 hour. 3-(trimethoxysilyl) propyl dimethyl octadecyl ammonium chloride (TMPDOA) was then added to act as a mesoporogen. In a separate container, sodium aluminate, deionized water, and sulfuric acid were combined and stirred for 1 hour. The aluminate solution was then added to the silica-containing solution, which was stirred for another 2 hours. The resulting gel had a molar oxide composition of 40 Na_2O: 95 SiO_2: 3.3 Al_2O_3: 5 TPA_2O: 26 H_2SO_4:

9000 H_2O: 5 TMPDOA. Samples were then loaded into Parr Acid Digestion Vessels and hydrothermally synthesized under autogenous pressure in at 150 ℃ for 4 days.

Non-mesoporous samples of ZSM-5 (MicZSM-5) were synthesized using tetrapropylammonium as a structure-directing agent. The synthesis gel had a molar oxide composition of 5 Na_2O: 100 SiO_2: 3.3 Al_2O_3: 8 TPA_2O: 3000 H_2O. Samples were then loaded into Parr Acid Digestion Vessels and hydrothermally synthesized under autogenous pressure at 150 ℃ for 5 days.

ZSM-5 samples with different particle sizes and identical Si/Al ratio of 30 were synthesized using colloidal silica as (Ludox 40) a silica source, sodium aluminate as an aluminum source, tetrapropylammonium bromide as a template. The particle size was controlled by adjusting the pH of the synthesis gel and crystallization time. Small particle ZSM-5-1 (below 2µm) was crystallized at pH 10 at 170 ℃ for 3 days. Medium particle ZSM-5-2 (below 10µm) was crystallized at pH 13 at 170 ℃ for 3 days. Large particle ZSM-5-3 (above10µm) was crystallized at pH 13 at 170 ℃ for 7 days. The elemental compositions of ZSM-5 samples were determined using X-ray fluorescence **(**XRF**).**

Ga/F catalyst (isomorphic substitution of alumina with gallium in the ZSM-5 framework) was synthesized using the method reported by Choudhary et al.[176-178]. Ga/F precursor solutions were prepared using N-brand silicate (SiO_2/Na_2O = 3.22, PQ Corp.), Ga-$(NO_3)_3$ (Sigma-Aldrich), Al-$(NO_3)_3$ (BDH), tetrapropylammonium bromide (TPA-Br, Aldrich), deionized water, and sulfuric acid (which is used for adjusting pH). The composition of the final reaction mixture in molar oxide ratios was: 3.3 Al_2O_3 : 1 Ga_2O_3 : 100 SiO_2 : 12.5 TPA-Br : 5020 H_2O where the amount of $Ga(NO_3)_3$ and $Al(NO_3)_3$

are varied to adjust SiO_2/Ga_2O_3, and SiO_2/Al_2O_3 ratio in the mixture, respectively. The reaction mixture was crystallized at 180 °C under autogenous pressure for 72 h in the autoclave.

After synthesis, zeolite samples were washed repeatedly with water, filtered and dried overnight at 80 ℃. Samples were then calcined in air at 550 ℃ for 6 h to remove occluded organic molecules. Zeolite samples were ion-exchanged to the ammonium form by treatment in 0.1M NH_4NO_3 at 70℃ for 24 h followed by filtration, and drying at 80 ℃. The samples were then calcined again at 550 ℃ to prepare the acid form of the zeolite before catalytic testing.

Ga1 and Ga3/HZSM-5 catalysts were prepared by ion exchange, where 1g of HZSM-5 (Zeolyst Int, CBV 3024E, SiO_2/Al_2O_3= 30) was refluxed in 100 mL of an aqueous solution of $Ga(NO_3)_3$ (0.010 M, Sigma-Aldrich, 99.9%) at 70℃ for 12 h. After ion exchange, the Ga1 solution was filtered out and the Ga3 solution was dried at 110 ℃. Both of the remained powders were calcined under air at 550 °C. Ga2/ZSM-5 was prepared by incipient wetness impregnation using a $Ga(NO_3)_3$ solution (0.43 M, Sigma-Aldrich, 99.9%). The impregnated ZSM-5 was dried at 110 ℃ overnight and calcined under air at 550 °C. The same process was used to synthesize Ga/SiO_2 and GaSD (Commercial spray dried ZSM-5 catalyst for fludized bed reactor) where silica (Aerosil 300) and SD was used instead of ZSM-5. A physical mixture zeolite catalyst was prepared from synthesized Ga/SiO_2 and ZSM-5 (Zeolyst Int., SiO_2/Al_2O_3 = 30). They were physically mixed to a 2.5wt% Ga concentration on ZSM-5. Silica (SiO_2) was treated as an inert. The Ga content for each catalyst was determined by inductively coupled plasma (ICP) analysis performed by Galbraith Laboratories (Knoxville, TN).

Samples used to study the effect of framework SiO_2/Al_2O_3 were purchased from Zeolyst with silica-to-alumina ratios of 23, 30, 50 and 80.

6.2.2 Surface Dealumination

Zeolite samples in the H^+ form were treated in a 2 M tartaric acid solution for 1 h at 70 ℃ to selectively remove surface acid sites (MicZSM-5* and MesZSM-5*). After treatment, samples were quickly cooled to room temperature, filtered and dried at 80 ℃. Samples were then ion exchanged with NH_4NO_3 and calcined again as described above.

6.3 Results and Discussion

6.3.1 Effect of Silica-to-Alumina Ratio (SAR)

Changing the alumina content of the zeolite particles will impact both the hydrophilicity of the catalyst[165] and the number density of Brønsted acid sites and hence may impact the aromatic yield [179]. ZSM-5 can be synthesized over a wide range of silica-to-alumina ratios, and this has an effect on its activity for biomass catalytic fast pyrolysis. Four ZSM-5 samples (obtained from Zeolyst) with different silica-to-alumina ratios (23, 30, 50, 80) were tested for CFP of glucose to study the effect of changing the Al content in the catalyst. X-ray diffraction of the samples confirmed that all were highly crystalline MFI-type framework materials. Nitrogen adsorption measurements confirmed that all samples had microporous volume of approximately 0.12 cm^3/g and mesoporous volume between 0.03-0.08 cm^3/g (see Table 6.1). SEM images revealed that there were no visible morphological differences between the samples with different SAR.

Table 6.1 Microporous and mesoporous volumes of samples used for SiO_2/Al_2O_3 study as measured by N_2 adsorption.

Sample	V_{micro} (cm^3/g)	V_{meso} (cm^3/g)
ZSM-5, SAR = 23	0.115	0.029
ZSM-5, SAR = 30	0.107	0.056
ZSM-5, SAR = 50	0.124	0.059
ZSM-5, SAR = 80	0.119	0.077

The yield of aromatic products from glucose as a function of the bulk silica to alumni ratio is shown in Figure 6.1. The maximum aromatic yield occurred at a $SiO_2/Al_2O_3 = 30$, with a concurrent minimum in the amount of coke produced. The CO and CO_2 produced during CFP are considered to be the products of decarbonylation and decarboxylation reactions, respectively [180]. The strong Brønsted acid sites in ZSM-5 have been shown to be active for the decarbonylation of benzaldehydes[181] and furfurals[182], two types of compounds produced during biomass fast pyrolysis[183]. The amount of CO produced is at a maximum for the $SiO_2/Al_2O_3 = 30$ sample, suggesting that there may be a relationship between the rate of oxygen removal via decarbonylation and the formation of aromatic species. A silica-to-alumina ratio of 30 represents an optimal composition for the high availability of Brønsted sites while simultaneously maintaining the hydrophilicity and Brønsted acid strength necessary to catalyze decarbonylation of the pyrolysis intermediates. As the silica-to-alumina ratio of ZSM-5 is decreased, the increasing polarity of the framework helps to energetically stabilize the polar oxygenates which are important intermediates during pyrolysis. This stabilization makes energetically more demanding to remove oxygen via decarbonylation, decarboxylation, or dehydration. Similar effects of the silica-to-alumina ratio on reactivity have been observed in the esterification of acetic acid and butanol over USY[184] and dodecane cracking over ZSM-5 [185].

The amount of CO_2 produced during the reaction depends weakly on the aluminum content of the ZSM-5 samples. The sample with the highest aluminum content produced the highest amount of CO_2, suggesting that the decarboxylation is enhanced by Brønsted acid catalysis but is less sensitive to acid site density than decarbonylation.

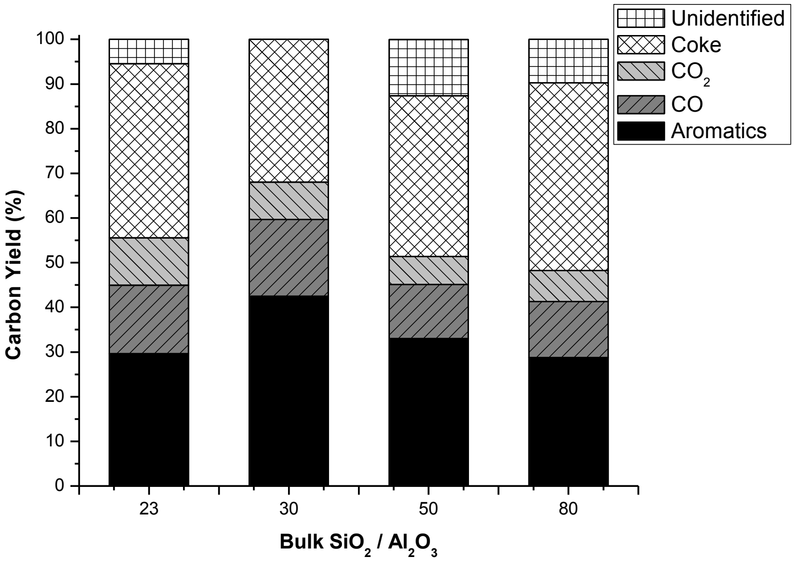

Figure 6.1 Yield of aromatic hydrocarbons, CO_2, CO, and coke produced from catalytic fast pyrolysis of glucose over ZSM-5 with varying SiO_2/Al_2O_3 composition. Reaction conditions: 600 °C, 19 mg catalyst / mg glucose, 240 s reaction time.

The distribution of aromatic hydrocarbon products from CFP of glucose changed slightly between samples as shown in Figure 6.2. The ZSM-5 sample with the highest aluminum content showed the highest selectivity towards smaller aromatic products (benzene and toluene), and samples with a lower amount of aluminum were slightly more selective towards larger products (C_8+ aromatics and polyaromatics). The larger aromatic products included xylenes, ethylbenzene, trimethylbenzene, ethylmethyl benzene, and indane.

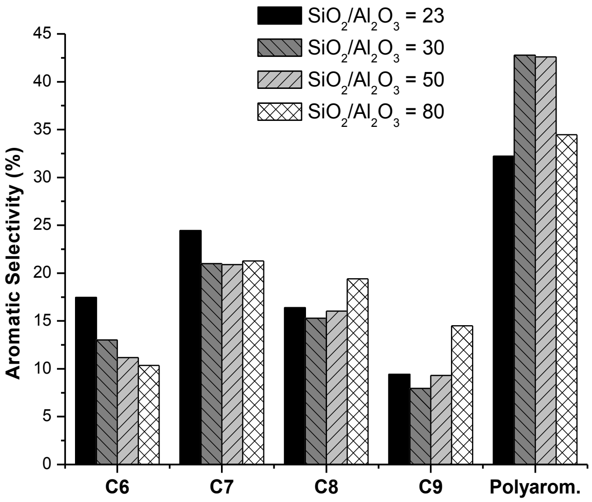

Figure 6.2 Distribution of aromatic products from CFP of glucose over ZSM-5 with varying SiO_2/Al_2O_3 composition. Reaction conditions: 600 °C, 19 mg catalyst / mg glucose, 240 s reaction time.

The results show the yield and product distribution are influenced to some degree by the concentration of aluminum in the sample. The optimum aluminum content of the ZSM-5 CFP catalyst to maximize yield of aromatic hydrocarbons occurs at a SAR of 30. However, the relationship between aluminum content and selectivity for different aromatic species is less clear: other aspects of the ZSM-5 catalyst must be modified to control and improve the product distribution.

6.3.2 Effect of Catalyst Particle Size

Zeolite catalysts with small particle size will have enhanced diffusion characteristics by a shortening in the diffusion path length of reactants and products in and out of the micropores [162, 186-188]. The higher internal diffusion rate can have a positive effect on catalytic chemistry for desired products. In addition, high surface area created by small particle size might facilitate access of molecules into micropore openings. Thus, three ZSM-5 samples with different particle sizes were tested for CFP of glucose to study the effect of changing the catalyst particle size. X-ray diffraction of the samples confirmed that all samples were highly crystalline MFI materials. The particle sizes of samples were measured by SEM (see Figure 6.3). SEM images showed that each of the samples had different particle size of ZSM-5-1(below 2 µm), ZSM-5-2(below 10µm), and ZSM-5-3(above 10µm).

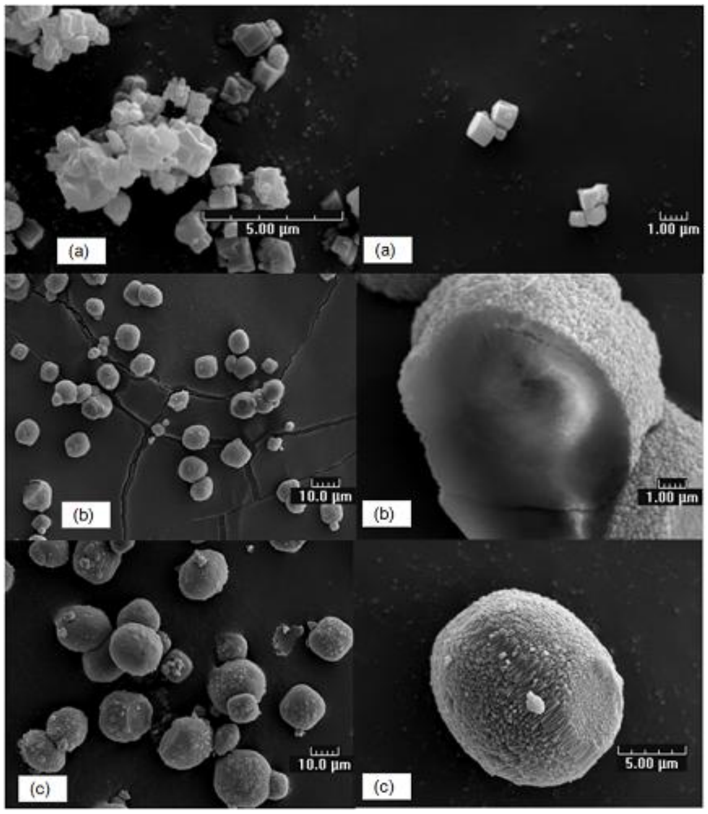

Figure 6.3 Scanning electron microscopy images of (a) ZSM-5-1, (b) ZSM-5-2, and (c) ZSM-5-3.

The silica-to-alumina ratios of samples were determined by X-ray fluorescence (XRF) spectroscopy (see Table 6.2). It is critical to keep identical silica-to-alumina ratio among ZSM-5 samples because silica-to-alumina ratio impacts on the aromatic yield and selectivity of CFP of glucose, as shown in the last section (6.3.1). However, ZSM-5-1 had lower silica-to-alumina ratio (SiO_2/Al_2O_3=30) than ZSM-5-2 and ZSM-5-3 (SiO_2/Al_2O_3=60).

Table 6.2 Elemental analyses of the samples by XRF.

Sample	Na (wt%)	Si (wt%)	Al (wt%)
ZSM-5-1	1.667	43.56	2.66
ZSM-5-2	0.938	45.26	1.46
ZSM-5-3	0.625	45.31	1.39

The yield and selectivity of aromatics from CFP of glucose as a function of particle size are shown in Figure 6.4 and 6.5. Highest aromatic yield and lowest coke yield were observed with the small particle ZSM-5-1, suggesting that small particles may increase the rate of aromatic formation and slow the rate of coke formation. Significant increase in the aromatic yield was observed with decreasing particle size from ZSM-5-2 (below 10 µm) to ZSM-5-1 (below 2 µm), while ZSM-5-2 and ZSM-5-3 showed a similar aromatic yield. The distribution of aromatic products showed some trends as a function of particle size, as shown in Figure 6.5. As the particle size became smaller, the selectivity toward polyaromatics and benzene increased and the selectivity for xylenes and C_9 aromatics decreased.

The results show that ZSM-5 with small particle size enhances aromatic production and suppresses coke formation. However, due to the higher aluminum content in the ZSM-5-1 sample, the effect of particle size is not conclusive. Thus, mesoporous ZSM-5 was used to better understand the effect of enhanced diffusion rate on the CFP of biomass.

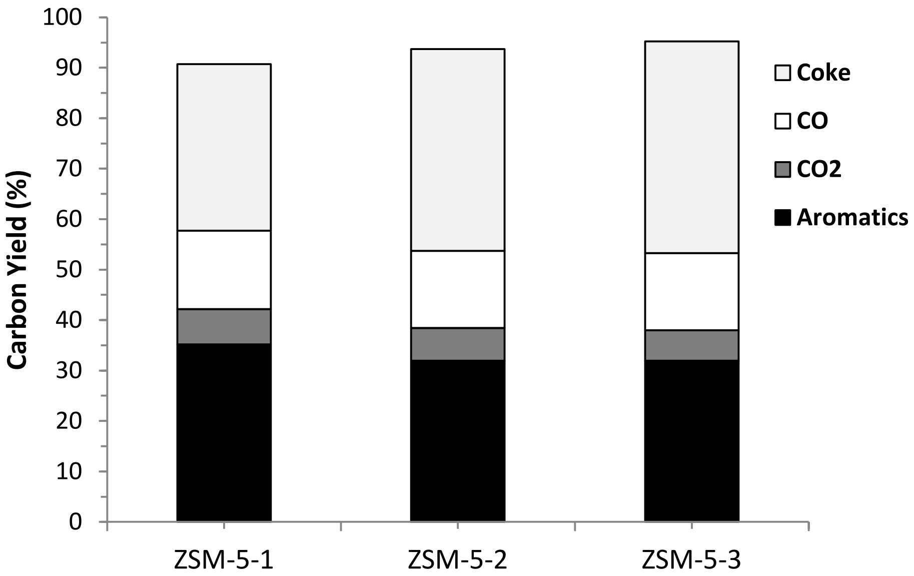

Figure 6.4 Yield of aromatic hydrocarbons, CO_2, CO, and coke produced from catalytic fast pyrolysis of glucose over ZSM-5 with varying particle size. Reaction conditions: 600 ℃, 19 mg catalyst / mg glucose, 240 s reaction time.

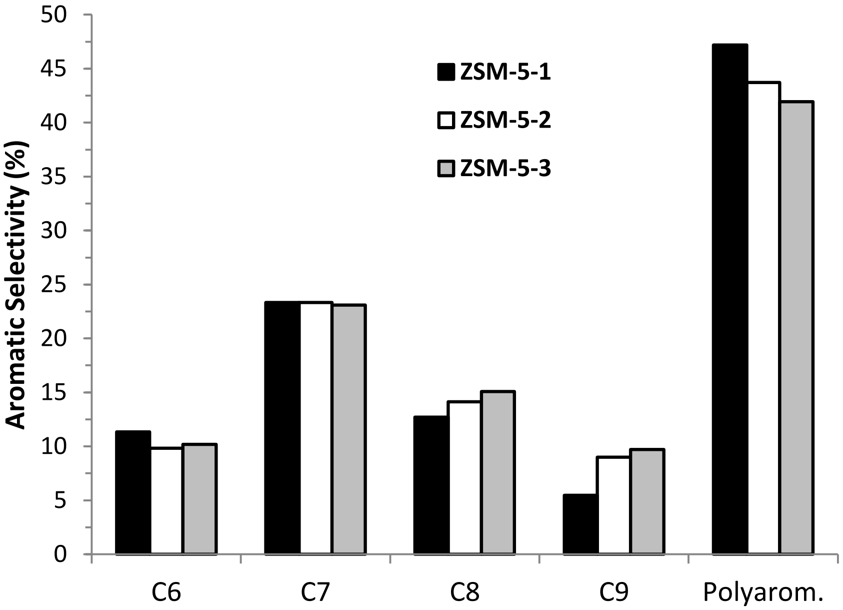

Figure 6.5 Distribution of aromatic products from CFP of glucose over ZSM-5 with varying particle size. Reaction conditions: 600 ℃, 19 mg catalyst / mg glucose, 240 s reaction time.

6.3.3 Effects of Mesoporosity and Removal of External Surface Acid Sites

The effects of mesoporosity and an acid treatment were investigated to determine the roles of internal mass transfer rate and external-surface catalysis during CFP of biomass-derived compounds. Samples of ZSM-5 were synthesized through a conventional TPA hydroxide method (MicZSM-5) and through a method using a combination of TPA and an organosilane surfactant to create crystalline ZSM-5 samples with hierarchical mesopores (MesZSM-5). All samples were synthesized with $SiO_2/Al_2O_3 = 30$. Samples of both materials were then treated with L-tartaric acid (MicZSM-5* and MesZSM-5*) to selectively remove acid sites from external particle surfaces and to widen any existing mesopores[189].

X-ray diffraction measurements confirmed that both the conventional and hierarchical samples of ZSM-5 were crystalline (Figure 6.6) after the tartaric acid treatment. Acid treatment of the mesoporous sample led to a decrease in intensity of the low angle peaks ($2\theta < 10°$), suggesting some reduction in long-range crystalline order. This observation is consistent with the acid leaching of surface material leading to the expansion of the intracrystalline mesopores.

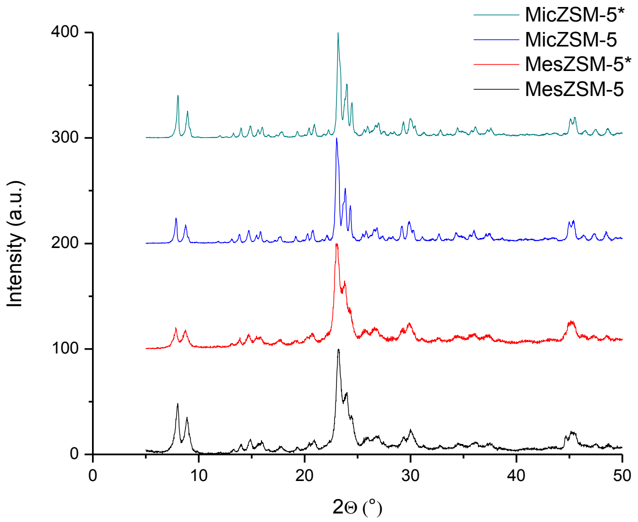

Figure 6.6 X-ray diffraction patterns of mesoporous and conventional ZSM-5 catalysts both before and after dealumination in tartaric acid. The ZSM-5 crystal structure is retained after acid treatment.

The porosity of the zeolite particles was quantified using N_2 physisorption. An interesting consequence of the acid treatment was an increase in the average diameter of the mesopores in the mesoporous ZSM-5 sample. Figure 6.7 shows that the untreated MesZSM-5 sample has pores 4-6 nm in diameter, while after acid treatment (MesZSM-5*) these pores expanded to 8-12 nm. The total mesoporous volume of this material was also increased by the acid treatment, and the microporous volume increased slightly.

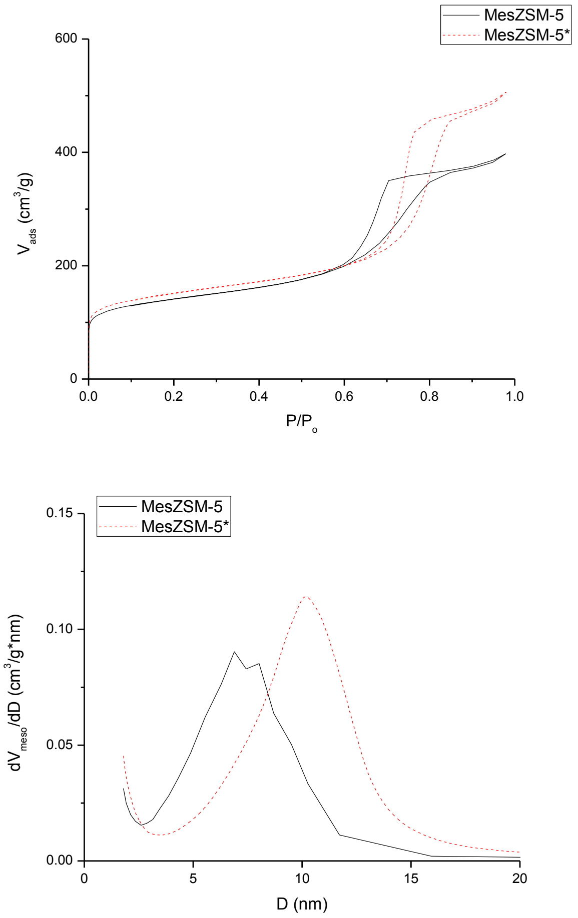

Figure 6.7 Nitrogen adsorption isotherms and BJH adsorption pore size distribution of mesoporous ZSM-5 catalyst both before (solid line) and after (dashed line) dealumination in L-tartaric acid.

Nitrogen adsorption on the MicZSM-5 catalyst resulted in a type I isotherm characteristic of a purely microporous material. A slight increase in the microporous volume was observed upon acid treatment (MicZSM-5*) of the non-mesoporous sample as seen in Table 6.3, but the sample remained purely microporous. This result shows that the acid treatment can be used to enhance existing mesoporosity, but is not a means for creating mesoporosity by itself. The adsorption isotherms show an increase in the measured microporous volume of the samples after the dealuminating treatment. The voids created by removal of aluminum from the ZSM-5 framework likely account for this change.

Table 6.3 Microporous and mesoporous volume of the ZSM-5 samples.

Sample	**V_{micro} (cm^3/g)**	**V_{meso} (cm^3/g)**
MicZSM-5	0.118	0.054
MicZSM-5*	0.122	0.062
MesZSM-5	0.107	0.550
MesZSM-5*	0.112	0.709

Figure 6.8 shows SEM images for mesoporous and purely microporous samples both before and after dealumination. Significant structural differences between MesZSM-5 and MicZSM-5 are clear. The primary particles comprising the mesoporous sample are much smaller than those observed for the purely microporous ZSM-5 sample. SEM images of the samples after tartaric acid treatment showed no visible decrease in particle size or roughening of particle surfaces.

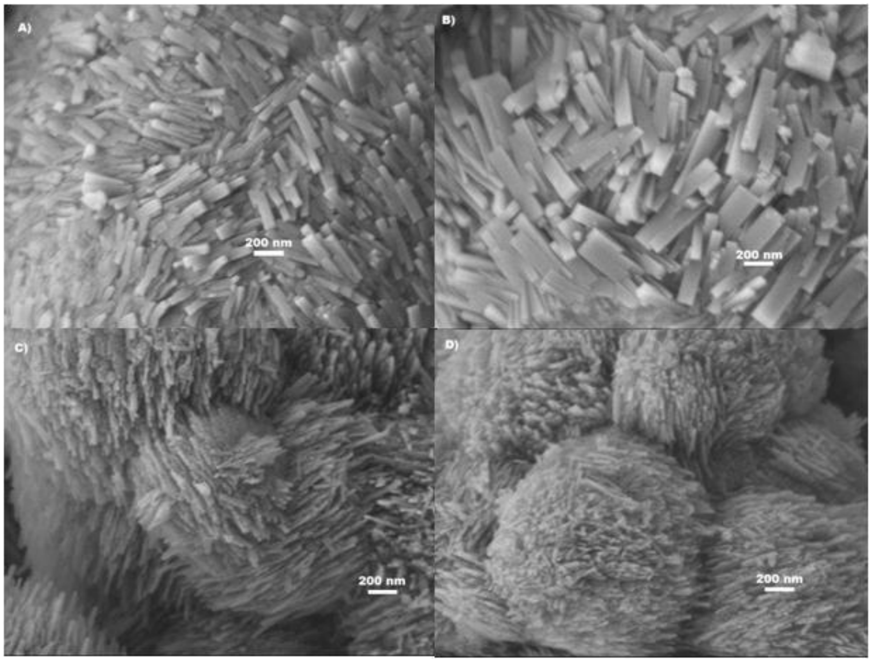

Figure 6.8 SEM images of A) MicZSM-5 before and B) after acid treatment, C) MesZSM-5 before and D) after acid treatment.

The extent of aluminum removal from particle surfaces was quantified by XPS and the bulk composition of the zeolite samples was measured using EDS (see Table 6.4). The XPS measurements show that the acid treatment was able to remove approximately 30% of the aluminum from the exterior particle surfaces in both cases. The EDS measurements show no statistically significant change in the bulk composition of the zeolite samples after the tartaric acid treatment. Taken together, this is experimental evidence showing that the tartaric acid treatment is highly selective in leaching Brønsted acid sites from the particle surface.

Table 6.4 Surface (via XPS) and bulk composition (via EDS) of ZSM-5 samples before and after dealumination.

	Surface SiO_2 / Al_2O_3		Bulk SiO_2/Al_2O_3	
Sample	As-synthesized	Acid Treated	As-synthesized	Acid Treated
MesoZSM-5	34	48	42 ± 20	45 ± 16
TPAZSM-5	46	65	32 ± 16	31 ± 12

6.3.3.1 Glucose and Maple Wood Catalytic Pyrolysis

Figures 6.10 and 6.11 show the yield of different products from pyrolysis of glucose and powdered maple wood, respectively, over the ZSM-5 catalysts. The removal of surface acid sites and creation of hierarchical mesopores did little to improve the yield of aromatic products from CFP. The yield of CO_2 was increased slightly over the mesoporous samples. The removal of the acid sites from the surface sites and mesopore walls by dealumination had no significant effect on the extent of coke formation. This result indicates that acid sites present on mesopore walls and external particle surfaces do not promote coke formation over production of volatile aromatic species.

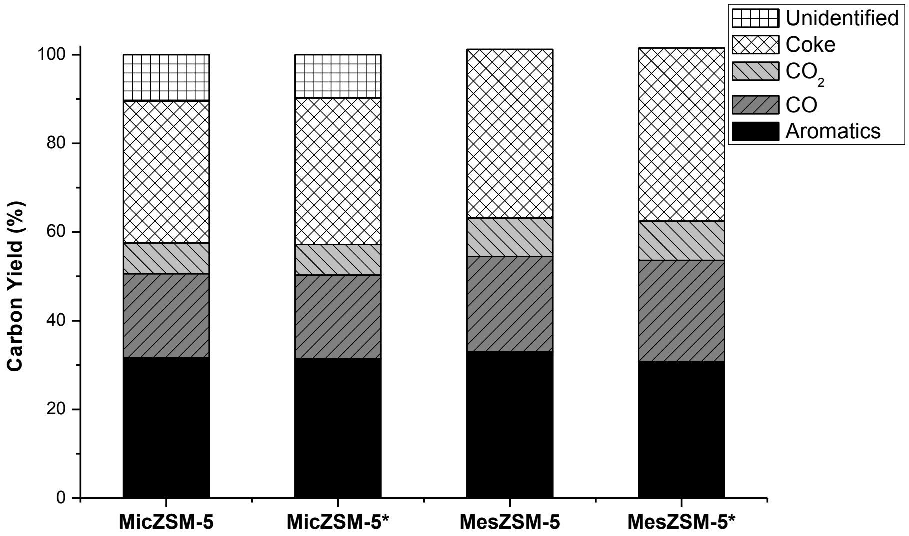

Figure 6.9 Comparison of the yield of aromatics from glucose pyrolysis over microporous ZSM-5 (MicZSM-5), tartaric acid-treated ZSM-5 (MicZSM-5*), mesoporous ZSM-5 (MesZSM-5) and mesoporous ZSM-5 treated with tartaric acid (MesZSM-5*). Reaction conditions: 600 ℃, 19 mg catalyst / mg glucose, 240 s reaction time.

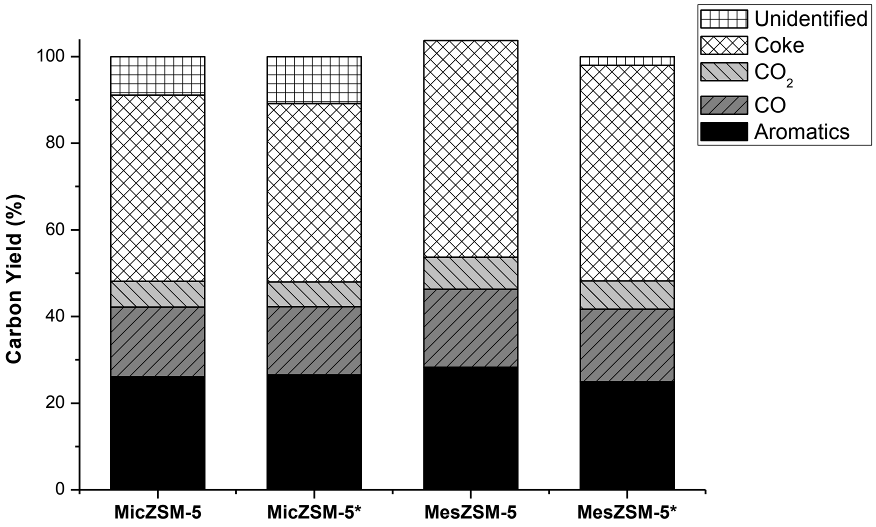

Figure 6.10 Comparison of the yield of aromatics from maple wood pyrolysis over microporous ZSM-5 (MicZSM-5), tartaric acid-treated ZSM-5 (MicZSM-5*), mesoporous ZSM-5 (MesZSM-5) and mesoporous ZSM-5 treated with tartaric acid (MesZSM-5*). Reaction conditions: 600 ℃, 19 mg catalyst / mg wood, 240 s reaction time.

The most notable difference between mesoporous and purely microporous samples was the distribution of aromatic products. Mesoporous ZSM-5 was more selective for the production of larger aromatic species from glucose (Figure 6.12). The microporous materials produced only a small amount of C_9 and larger aromatics, while this was dramatically increased over the mesoporous material. Similar effects of mesoporosity on product selectivity have also been observed for xylene isomerization on a zeolite catalyst[190]. Decreasing the diffusion length in a ZSM-5 catalyst has also been shown to lead to larger products in the conversion of propanal[191]. The dealuminated mesoporous ZSM-5 sample was slightly more selective for larger hydrocarbons (C_{10} and polyaromatics) than the untreated mesoporous sample, suggesting that the mesopore diameter can influence the distribution of aromatics produced through catalytic pyrolysis.

The trends in aromatic distribution were largely the same during the pyrolysis of maple wood (Figure 6.13). Both mesoporous catalysts were more selective than the purely microporous samples for the production of C_8 and larger aromatics. As with glucose, the larger mesopores in the dealuminated sample shifted the product distribution towards C_{10} and larger polyaromatic products. However, the mesoporous samples were found to produce fewer polyaromatics from maple wood than the microporous samples. The volatile intermediate species formed during the initial thermal decomposition of wood are larger than those formed during pyrolysis of glucose, and these reactants naturally are less able to access the Brønsted acid sites in a purely microporous sample of ZSM-5. When this restriction on reactant diffusion is relaxed by incorporating mesopores into the ZSM-5, these intermediate products are more likely to crack into units that lead to monoaromatics inside the zeolite rather than forming coke through a noncatalytic process outside of the zeolite. Mesoporous samples of ZSM-5 favor the production of larger alkylaromatics due to the relaxation of shape-selectivity controlling the product distribution.

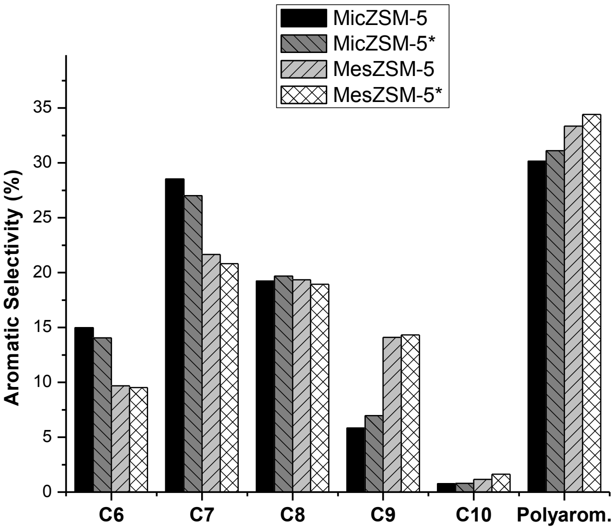

Figure 6.11 Distribution of aromatic products from pyrolysis of glucose over microporous ZSM-5 (MicZSM-5), tartaric acid-treated ZSM-5 (MicZSM-5*), mesoporous ZSM-5 (MesZSM-5) and mesoporous ZSM-5 treated with tartaric acid (MesZSM-5*). Reaction conditions: 600 °C, 19 mg catalyst / mg glucose, 240 s reaction time.

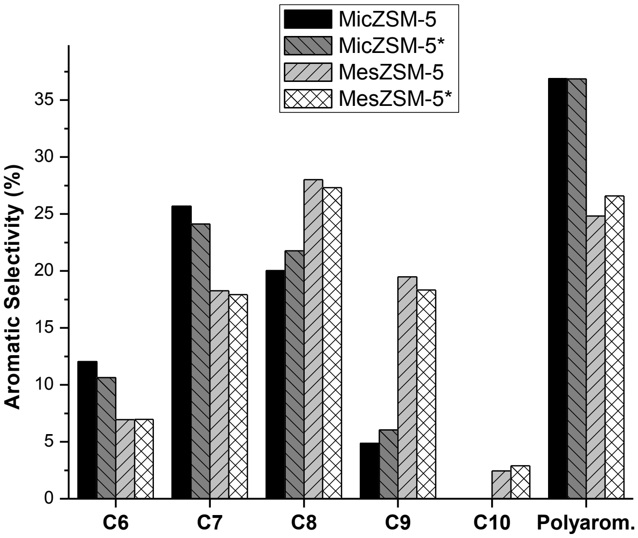

Figure 6.12 Distribution of aromatic products from pyrolysis of maple wood over microporous ZSM-5 (MicZSM-5), tartaric acid-treated ZSM-5 (MicZSM-5*), mesoporous ZSM-5 (MesZSM-5) and mesoporous ZSM-5 treated with tartaric acid (MesZSM-5*). Reaction conditions: 600 °C, 19 mg catalyst / mg wood, 240 s reaction time.

6.3.3.2 Furan Conversion

The micro- and mesoporous ZSM-5 catalysts were tested for conversion of furan in a continuous flow fixed-bed reactor to measure the activity and selectivity of these different materials as shown in Table 6.5. We have previously shown that furan is an important intermediate during CFP of glucose (Chapter 4). In addition, the enhancement of reactant diffusivity by mesoporous ZSM-5 could be better observed in a fixed-bed reactor than the semi-batch reactor. Furan CFP had a slightly lower reaction rate over the mesoporous ZSM-5 samples than over the microporous samples at the conditions tested. As observed for the CFP of glucose and maple wood, the mesoporous catalysts also produced more coke from furan. The mesoporous ZSM-5 samples had slightly lower yields of aromatics and olefins than the microporous ZSM-5. This suggests that the mesopores act as spaces for the formation and accumulation of coke. The improved molecular diffusion in mesopores does not contribute positively to the total yield of aromatics from pyrolysis of furan. The mesoporous material had lower selectivity to benzene, toluene and xylene, and tended to favor production of larger monoaromatics than the microporous materials. This was also observed for these catalysts during the conversion of glucose and maple wood. CO and CO_2 selectivity were similar for all catalysts tested.

Treatment of samples with tartaric acid to remove external surface acid sites does not appear to improve the CFP of furan to hydrocarbons. Minor differences in the aromatic yield and distribution were observed between dealuminated samples and the untreated parent materials, but no clear trends can be associated with the removal of surface acid sites. This suggests that the role of surface acid sites during the CFP of biomass is not critical enough to impact the observed products.

Table 6.5 Furan conversion and product selectivity obtained from reaction over microporous and mesoporous ZSM-5 samples. Reaction conditions: 600 °C, WHSV 10.4 h^{-1}, and furan partial pressure 6 torr.

Catalyst	Mic HZSM-5	Mic HZM-5*	Mes HZSM-5	Mes HZSM-5*
Furan conversion	35.9	40.3	36.3	29.5
Overall selectivity (%)				
Aromatics	44.7	40.5	35.8	37.0
Olefins	19.2	17.2	17.1	16.3
CO	12.0	11.3	9.8	9.2
CO_2	2.7	2.8	2.8	2.5
Coke	17.4	24.6	29.0	28.1
Oxygenates[1]	4.1	3.7	5.5	6.9
Aromatic selectivity (%)				
Benzene (C_6)	21.0	20.7	18.3	17.8
Toluene (C_7)	18.6	18.1	17.7	18.2
C_8 Aromatics[2]	8.8	8.1	8.7	8.7
C_9 Aromatics[3]	13.9	14.2	16.5	15.7
C_{10} Aromatics[4]	7.4	8.3	11.7	12.8
Naphthalenes	30.4	30.6	27.1	26.7
Olefin selectivity (%)				
Ethylene	36.4	36.6	26.7	26.8
Propylene	34.8	34.5	38.1	34.8
Allene	8.2	8.4	11.8	13.7
C_4 olefins	4.6	5.2	6.7	5.1
C_5 olefins	12.5	11.7	11.1	13.0
C_6 olefins	3.5	3.6	5.6	6.6

1. Oxygenates include methylfuran, furylethylene, and benzofuran.
2. C_8 aromatics include ethylbenzene, styrene, and xylenes.
3. C_9 aromatics include indene, indane, and methylstyrenes.
4. Methylindene is the only C_{10} monoaromatic observed.

6.3.4 Bifunctional Ga/ZSM-5 Catalyst

Ga/ZSM-5 catalyst has been shown to be the effective catalyst for bio-oil upgrading into aromatics[19, 39] and methanol conversion into aromatics[89]. Thus, Ga/ZSM-5 was used for CFP of biomass and studied in detail to explore how Gallium impacts the reaction chemistry and the aromatic yield. Metal can be incorporated into ZSM-5 by a variety of methods such as ion exchange, incipient wetness, isomorphous metal substitution, and the degree of Ga exchange and the location of Ga in ZSM-5 largely depend on the preparation method. Therefore, a series of Ga promoted ZSM-5 catalysts was prepared to systematically study the effect of gallium incorporation into ZSM-5 on the aromatic yield and selectivity from CFP of biomass. Four different methods were used for synthesis of Ga catalysts: (1) ion-exchange (Ga1/HZSM-5) (2) incipient wetness (Ga2/HZSM-5), (3) modified ion-exchange (Ga3/HZSM-5) and (4) a hydrothermal synthesis method where the Ga was incorporated directly into the ZSM-5 framework (GaF4 – GaF7/ZSM-5). Modified ion-exchange method was employed to increase the Ga loading in ZSM-5. X-ray diffraction measurements confirmed that all zeolite samples were purely MFI structure (see Figure 6.13). A Ga/SiO_2 catalyst was also prepared by incipient wetness to investigate the role of isolated Gallium on the reaction chemistry. Ga was added to a commercially available spray-dried (SD) catalyst as well (GaSD) for fluidized bed reactor testing. The bulk composition of all catalysts was determined using ICP (see Table 6.6).

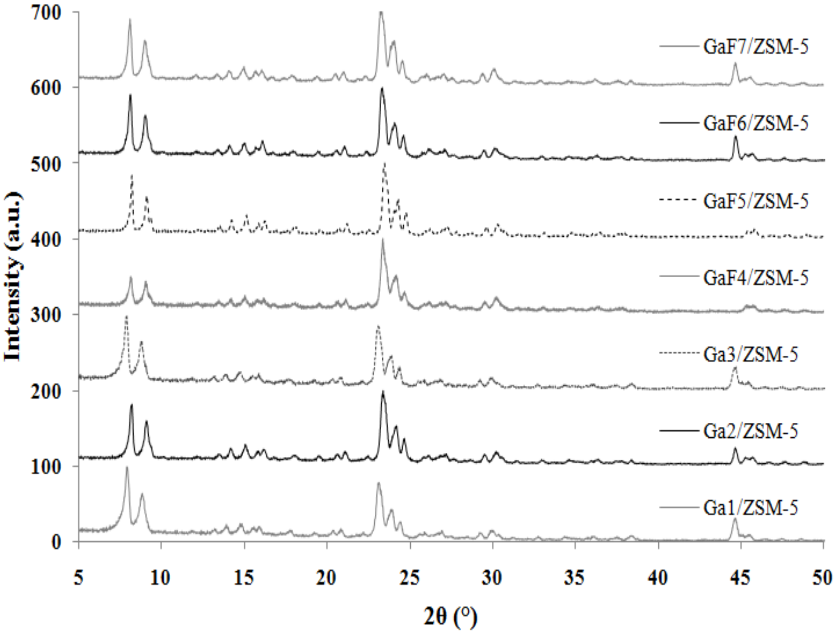

Figure 6.13 X-ray diffraction patterns of the synthesized Ga/ZSM-5 catalysts

Table 6.6 Elemental analysis of synthesized catalysts

Preparation	Code	SiO_2/Al_2O_3	SiO_2/Ga_2O_3	$SiO_2/(Al_2O_3+Ga_2O_3)$
Commercial ZSM-5	ZSM5	30	0	30
Ion-exchanged ZSM5	Ga1/HZSM5	30	262	27
Wet-impregnated ZSM5	Ga2/HZSM5	30	108	23
Ion-exchanged ZSM5	Ga3/HZSM5	30	68	21
Hydrothermally synthesized from gel state (Ga is in the framework)	GaF4/ZSM5	0	32	32
	GaF5/ZSM5	0	51	51
	GaF6/ZSM5	34	108	26
	GaF7/ZSM5	34	47	20
Wet-impregnated SiO_2	Ga/SiO_2	0	20	20
Physical mixture (2.5wt% Ga on ZSM5 synthesized by Ga/SiO_2+ZSM5)	PM	30	86	22
Commercial spray dried catalyst	SD	30	0	30
Wet-impregnation of SD	GaSD	30	108	23

The acidity of the ZSM-5 and Ga promoted catalysts (Ga2 and Ga3/HZSM-5) was examined using NH_3- and IPA (isopropylamine)-TPD for (Figure 6.14). Table 6.7 shows the acid density of the three zeolites where total and Brønsted acid densities were calculated from NH_3-TPD and IPA-TPD, respectively. The ratio of Brønsted to total acid densities decreased with the increase of Ga content. There is no peak shift in NH_3 and IPA desorption between catalysts, suggesting that some protons were replaced by Ga species and the remaining protons were not affected.

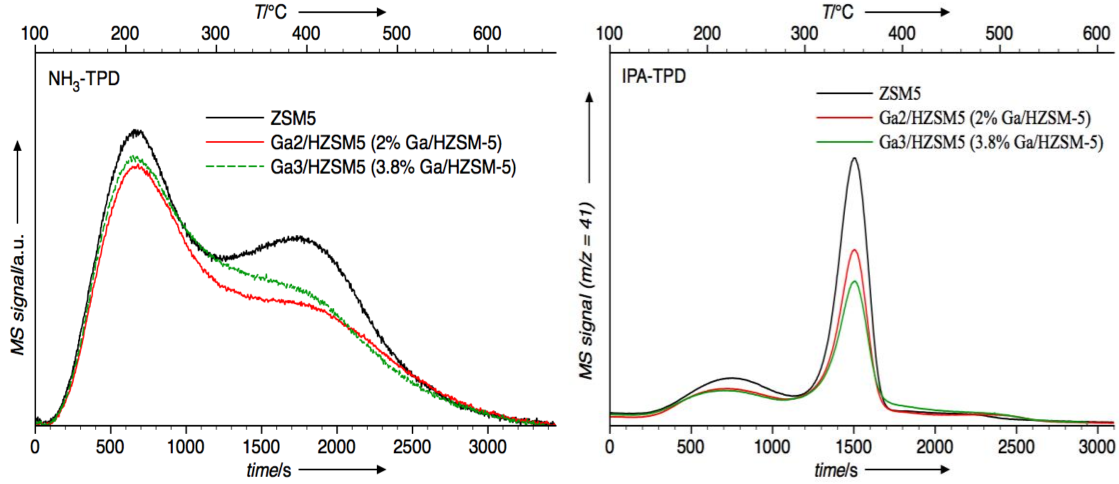

Figure 6.14 Temperature-programmed desorption of NH_3 and IPA (isopropylamine) from ZSM-5, Ga2, and Ga3/HZSM-5 catalysts; (a) NH_3-TPD, recorded m/z value = 17; (b) IPA-TPD, recorded m/z = 41 (propylene).

Table 6.7 Brønsted acid density (A_B, by IPA-TPD), total acidity (A_{total}, by NH_3-TPD), the ratio of Brønsted to total acidity, the Lewis acid density (A_L, calculated)

Catalyst	A_B	A_{total}	A_B/A_{total}	A_L
ZSM-5	0.41	0.80	0.51	0.39
Ga2/HZSM-5	0.25	0.58	0.42	0.34
Ga3/HZSM-5	0.23	0.65	0.35	0.43

6.3.4.1 Furan Conversion

Table 6.8 shows the products distribution for furan conversion over the different Ga/ZSM-5 catalysts in a flow fixed-bed reactor. The Ga promoted catalysts that were prepared by the ion-exchange and incipient wetness methods had comparable catalytic activity to ZSM-5. The aromatics selectivity increased from 31% for ZSM-5 up to 44% for Ga3/HZSM-5. The addition of Ga also caused the olefins selectivity to decrease, the CO selectivity to increase, and the coke selectivity to decrease. These same Ga promoted catalysts also had a higher benzene and naphthalene selectivity than the unpromoted ZSM-5. The allene selectivity increased from 5 to 20 % when Ga was added to ZSM-5. These results suggest that the Ga is increasing the rate of both decarbonylation (to form allene and CO) and also olefins aromatization (to convert more olefins into aromatics).

Table 6.8 Summary of furan conversion and carbon selectivity of products obtained by using ZSM-5 and Ga promoted ZSM-5 as the catalyst; reaction conditions: temperature 600 °C, WHSV 10.4 h^{-1}, and furan partial pressure 6 torr

Catalyst	ZSM-5	Ga1/ HZSM-5	Ga2/ HZSM-5	Ga3/ HZSM-5	Ga4F/ ZSM-5	Ga5F/ ZSM-5	Ga6F/ ZSM-5	Ga7F/ ZSM-5	Ga/ SiO_2
Furan conversion (%)	48	53	50	47	28	15	28	33	14
Overall selectivity(%)									
Aromatics	31.0	37.8	39.7	43.5	28.3	23.0	35.5	24.8	17.8
Olefins	19.1	16.0	14.0	13.2	17.5	19.9	17.9	16.3	27.7
Aromatics + olefins	50.1	53.9	53.7	56.8	45.8	42.8	53.4	41.1	45.6
CO	13.9	16.8	16.8	17.2	14.9	13.0	16.1	18.6	9.3
CO_2	1.1	1.7	2.0	1.8	0.7	0.0	0.5	1.0	4.6
Coke	33.8	26.9	27.1	23.8	38.3	43.7	28.9	38.6	39.9
Oxygenates	1.0	0.6	0.5	0.5	0.4	0.4	1.1	0.7	0.7
Aromatic selectivity (%)									
Benzene	25.9	38.8	35.6	33.7	45.4	40.5	38.1	53.8	16.5
Toluene	23.6	21.2	17.5	15.1	16.1	13.3	16.1	17.5	12.3
Xylenes[a]	4.3	3.1	1.9	1.5	2.4	1.5	2.6	1.9	2.5
Benzofuran	5.9	4.0	3.2	3.4	7.3	11.6	5.5	4.6	13.3
Indenes[b]	19.3	10.4	11.6	11.5	15.1	19.0	13.8	10.7	19.2
Naphthalenes[c]	10.6	13.6	23.5	28.1	6.4	9.4	14.8	6.0	30.8
Alkylbenzenes[d]	1.2	0.6	0.4	0.3	0.5	0.3	0.6	0.5	0.3
Styrenes[e]	9.2	8.3	6.4	6.3	6.8	4.4	8.5	5.0	5.2
Olefin selectivity (%)									
Ethylene	38.7	39.9	40.4	39.6	18.2	13.6	34.1	41.6	18.7
Propylene	35.1	27.4	27.6	24.8	11.8	7.9	17.5	22.0	14.4
Allene	4.6	15.8	16.7	20.2	53.1	60.3	30.6	23.9	50.2
C_4 olefins	4.3	5.0	4.9	5.2	7.4	10.3	5.8	4.2	7.2
C_5 olefins	14.2	9.5	8.2	7.8	8.0	5.1	9.4	6.7	6.1
C_6 olefins	3.1	2.3	2.3	2.3	1.5	2.8	2.6	1.6	3.4

[a] Xylenes include p-, m-, and o-xylenes. [b] Indenes include indene, methylindenes and indane. [c] Naphthalenes include naphthalene and methylnaphthalene. [d] Alkylbenzenes include ethylbenzene and trimethylbenzene. [e] Styrenes include styrene and methylstyrenes.

The catalysts that had Ga inside the zeolite framework (GaF/ZSM-5) had a lower catalytic activity compared to ZSM-5. The GaF/ZSM-5 catalysts also had lower aromatics selectivity and higher coke selectivity than ZSM-5 (with the exception of Ga6F/ZSM-5), suggesting that framework Ga is undesirable for aromatics production. The low reactivity of GaF/ZSM-5 catalysts could be due to the unstable framework Ga at our reaction temperature 600°C. It has been shown that degalliation of the framework gallium occurred at 600°C, causing the decrease of acidity [192]. The Ga framework catalysts had very high allene selectivity, especially for those lacking strong Brønsted acid sites given by SiO_2/Al_2O_3 (Ga4F and Ga5F/ZSM-5). This suggested that strong Brønsted acid sites are required for allene conversion into olefins and the subsequent aromatization. The high benzene selectivity could be attributed to allene dimerization catalyzed by Ga species.

The Ga/SiO_2 catalyst had a very low activity for furan conversion and formed large amounts of coke. The Ga/SiO_2 catalyst also had a very high allene and CO selectivity, indicating that Ga catalyzes decarbonylation of furan into allene. The Ga/SiO_2 catalyst produced aromatics, primarily indenes and naphthalenes. The BTX selectivity was low (17, 12, and 3%, respectively) with Ga/SiO_2.

The results show that Ga/ZSM-5 enhances aromatic production from CFP of furan. Aromatic selectivity of up to 44% was obtained from the Ga/ZSM-5 samples prepared by the modified ion exchange method. Figure 6.15 shows that proposed reaction pathway for furan conversion over Ga/ZSM-5 catalyst[193]. Furan initially undergoes either decarbonylation to form allene (C_3H_4) and CO or Diels-Alder condensation to form benzofuran (C_8H_6O) and water. The allene can undergo either oligomerization to form a series of olefins, or alkylation with other aromatics to form heavier aromatics and ethylene.

The olefins can react with the furan to form aromatics and water. The benzofuran can also undergo decarbonylation to form benzene, CO, and coke. In this reaction scheme, Ga species can increase the rate of decarbonylation for allene formation, as we discovered in this study. In the literature, Ga promoted zeolite catalysts have been shown to increase the rate of olefins oligomerization and subsequent conversion into aromatics[168-171]. Furthermore, Ga promoted catalysts have also shown to have high rates of dehydrogenation and aromatization of alkanes[168-173]. Therefore, the furan decarbonylation and olefins aromatization are promoted by Ga species during CFP of furan.

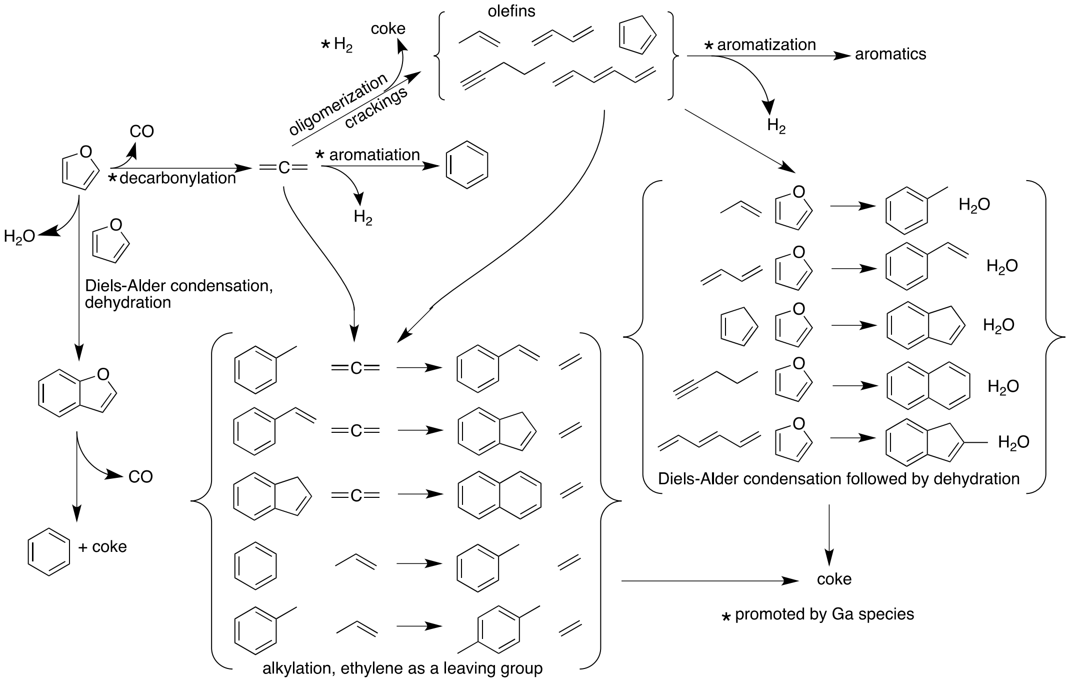

Figure 6.15 Reaction network of furan conversion into aromatics over ZSM-5 at 600℃.

6.3.4.2 Pine Wood Catalytic Pyrolysis

Because Ga promoted ZSM-5 catalysts show promising results for furan conversion, a spray-dried Ga promoted catalyst was prepared and also tested for CFP of pinewood sawdust in a bubbling fluidized-bed reactor (Table 6.8). The addition of Ga increased the aromatics yield from 15 to 23% at reaction temperature 550°C. These results suggest that the Ga promoted catalyst is able to convert not only model compounds but real wood into aromatics in higher yields.

Catalyst stability is an important issue for industrial application. The Ga promoted ZSM-5 catalyst was tested for 28 reaction-regeneration cycles to investigate the stability of Ga promoted catalysts during CFP of biomass. No significant deactivation was observed during the testing of this catalyst indicating that the minerals in the biomass do not poison this catalyst.

Table 6.9 Summary of pinewoods conversion obtained by using SD and GaSD as the catalyst[a]

Catalyst *T* /°C	ZSM-5 550	GaSD 550	ZSM-5 600	GaSD 600
Overall Carbon Yield(%)				
Aromatics	15.4	23.2	11.5	17.5
Olefins	7.1	8.9	8.8	6.6
Methane	2.0	1.5	2.0	2.8
CO_2	7.7	5.4	4.7	4.5
CO	20.3	17.1	24.9	17.2
Coke	42.1	33.3	34.0	37.6
Total	94.7	89.4	85.8	86.3
Aromatic Carbon Selectivity(%)				
Benzene	12.4	19.6	25.6	33.0
Toluene	31.2	34.3	37.8	33.7
Xylenes	22.4	18.9	16.9	10.2
Ethylbenzene	1.6	2.7	1.4	0.8
Styrene	2.5	2.4	1.1	0.6
Phenol	4.8	5.2	4.0	2.0
Benzofuran	6.2	1.8	1.6	3.2
Indene	0.9	1.2	0.9	0.1
Naphthalenes	18.2	14.0	10.7	0.6
Olefin Carbon Selectivity(%)				
Ethylene	34.3	42.5	42.4	43.7
Propylene	51.9	49.1	44.4	41.7
C_4 olefins	13.7	8.3	13.2	7.6
A+O Carbon Yield/Theoretical A+O Carbon Yield(%)				
	29.3	42.7	23.8	32.5

[a] Reactions were run at 550 and 600°C, WHSV 0.35 h^{-1}, and gas flow rate 1000 mL/min. Reaction time was 30 min.

6.4 Conclusions

In this study, we have investigated the catalytic fast pyrolysis of glucose, furan, maple/pine wood over different types of ZSM-5 catalyst. The aromatic yield from glucose CFP goes through a maximum as a function of framework silica-to-alumina ratio with an optimum at SAR=30. This composition also minimizes the amount of coke formed during reaction. This suggests that tuning the acid concentration and the hydrophilicity of the zeolite framework is necessary for obtaining high aromatic yields.

Creating hierarchical mesopores within the zeolite catalyst had little effect on the aromatic yield from CFP of glucose and maple wood in the pyroprobe reactor. However, CFP over mesoporous ZSM-5 catalysts yielded more coke than the purely microporous samples. This suggests that the mesopores may act as spaces for coke to form and accumulate. The purely microporous ZSM-5 catalyst favors the production of smaller monoaromatics (benzene, toluene, and xylene) while hierarchically mesoporous samples shifts the product distribution towards heavier alkylated monoaromatics. Similar observations were made in the CFP of furan in the fixed-bed reactor studies. The aromatic yield and selectivity from surface dealuminated samples were largely the same as the untreated parent material, suggesting that the presence of external surface acid sites plays only a minor role on the overall CFP chemistry.

Addition of Gallium to ZSM-5 catalyst increases the rate of aromatics production during CFP. We were able to produce 40% more aromatics over Ga promoted catalysts for CFP of pine wood. Furan conversion studies over Ga/ZSM-5 suggest that the catalyst is a bifunctional catalyst where the Ga increases the rate of decarbonylation and olefins aromatization whereas the zeolite catalyzes the other reactions such as oligomerization.

This study shows that the concentration of acid sites on the ZSM-5 catalyst, mesopores within the ZSM-5, and addition of Ga to ZSM-5 can be adjusted to tune aromatic selectivity and yield from CFP of biomass. Especially, the bifunctional Ga/ZSM-5 is a promising catalyst by significantly increasing aromatic yield from CFP of biomass.

CHAPTER 7

CATALYTIC FAST PYROLYSIS OF BIOMASS IN A PROCESS DEVELOPMENT UNIT

7.1 Introduction

We have previously demonstrated CFP technology in a semi-continuous lab scale fluidized bed reactor (2" in diameter) by obtaining an aromatic yield of 14% carbon directly from pinewood sawdust [24]. This data suggests the results from microscale semi-batch reactor can be reproduced in a realistic and scalable continuous reactor. However, the lab scale fluidized bed reactor can be operated for only a short time (less than an hour) because there is no continuous catalyst addition or removal. During CFP of biomass, the large amount of coke deposition on the catalyst deactivates the active sites of the catalyst and thereby reduces the catalytic activity for aromatic production after just 40 minutes. In order to operate the reactor continuously with maintaining a constant yield of aromatic products, the spent catalyst needs to be withdrawn from the reactor and replaced with de-coked catalyst during the operation.

The objective of this portion of the thesis is to study CFP of pine wood in a large-scale fluidized bed reactor that can operate continuously for a longer time. In addition, we will produce liter quantities of aromatic products in this reactor to demonstrate scalability and capability for continuous operation of CFP technology. This reactor system will be called a process development unit (PDU) that features the continuous addition and removal of catalyst. In the PDU, the spent catalyst is continuously replaced with the fresh catalyst during the reaction in order to maintain a constant yield. In order to optimize the reactor performance, we have studied how changing process variables, including the reaction temperature, the biomass weigh hourly space velocity (WHSV), catalyst to biomass ratio, static bed height (i.e. volume of the catalyst bed), and fluidizer gas velocity, affects the product yield and selectivity in the CFP of pinewood with a spray dried ZSM-5 catalyst. In particular, the results from the latter two variables are closely related to the hydrodynamic conditions in the fluidized bed reactor and thus will be discussed in detail. The PDU has been operated for three months to produce 1 L of aromatics at optimal reaction conditions.

In addition, we will study the stability of the ZSM-5 catalyst during long term operation which is crucial for the commercialization of CFP technology. It is possible that minerals (ash) in the biomass can poison the active sites of ZSM-5 catalyst during CFP. Thus, both catalyst activity measurements and characterizations of the ZSM-5 catalyst after 30 successive reaction-regeneration cycles were conducted to study the influence of impurities in the biomass and operating conditions on the performance and physical/chemical properties of the ZSM-5 catalyst.

7.2 Experimental

The experimental methods and materials used for this work are described in Sections 2.4, 2.5, 2.6, 2.7, and 2.8.

7.2.1 Process Development Unit

A schematic of the process development unit is shown in Figure 7.1. The fluidized bed reactor is a 4 inch diameter 316 stainless steel tube 30 inches tall. The top of the freeboard expands to 6 inches to suppress entrainment of catalyst particles in the exit gas stream. The catalyst bed is supported by a distributor plate made from a stack of 316 stainless steel mesh sheets (200 mesh). The bottom of the reactor below the distributor plate serves as a gas preheater zone. This bottom section of the reactor was loosely packed with quartz wool for good gas distribution and good heat transfer. The catalyst is fluidized via a nitrogen gas stream controlled by a mass flow controller. The reactor is externally heated with a four-zone electric furnace, and the inlet gas stream is heated with a heating tape. All zones were maintained at reaction temperature. The temperatures of each zone were measured by K-thermocouples inserted into the reactor (~ 1 cm from wall).

The biomass feed (pine wood sawdust) is loaded into a sealed feed hopper (Tecweigh, volumetric feeder) and conveyed by a stainless steel auger inside the hopper into a feed tube connected to the side of the reactor (1 inch above the distributor plate). The second screw auger inside the feed tube rapidly carries biomass through the feed tube into the reactor. The auger is turned by an electric motor using speed control to provide a constant feed flow rate during reaction. The feed system was calibrated for different flow rates before reaction. The outside temperature of the feed tube was kept at 0℃ using a cooling jacket to prevent pre-pyrolysis of the biomass before introduction to the reactor. To maintain an inert environment in the reactor, the hopper is swept with nitrogen at a rate of 2 L min^{-1}. The wood used was ground down to pass through a 1mm screen before loading it into the hopper. The catalyst powder is injected, by a specially designed ball valve (Swagelok, T60M thermal series ball valve), into the top of the reactor from a sealed catalyst hopper. Two small cups, inside the valve, transfer the catalyst powder into the reactor by valve rotation. The valve is turned by an electric motor using speed control to provide a constant catalyst flow rate during reaction. The catalyst falls downward through the stainless steel tube inside the reactor. The end of the tube is 6 inches above the distributor plate. The catalyst hopper is swept with nitrogen at a rate of 800 mL min^{-1}. The catalyst is drawn from the reactor through the catalyst outlet tube connected to the side of the reactor (1.5 inch above the distributor plate). The same type of valve as the catalyst inlet valve is used. A small nitrogen flow at a rate of 40 mL min^{-1} is provided through the catalyst outlet tube for stripping any remaining products entrapped in the catalyst. Pressure drop across the reactor was monitored using a differential pressure gauge (0 to 8 inch of water).

The gas exiting the reactor passes through a cyclone where entrained solids are removed and collected. The gas exiting the cyclone enters a stainless steel bubbler filled with ethanol in an ice water bath, to quickly cool down the temperature of the hot vapor. The vapor then passes through a condenser train. The first two condensers are maintained at 0 ℃ in an ice bath and the following six condensers are maintained at -55 ℃ in a dry ice/acetone bath. Each condenser was filled with 10 - 20 ml of ethanol to trap aromatic species more efficiently. The non-condensed vapors exiting the condenser train are collected in a Tedlar gas sampling bag for GC-FID/TCD analysis. Total gas flow is measured using a bubble flow meter prior to the gas sampling. Liquids collected in the condensers are quantitatively removed after reaction with ethanol. The total volume of the ethanol/product solution collected is recorded. The solution is then analyzed with GC/MS and GC/FID. The mass of carbon on the spent catalyst is determined by Thermogravimetric Analyzer (TGA) and Total Organic Carbon Analyzer (TOC).

The catalyst used was a commercial spray-dried 40% ZSM-5 catalyst (Intercat. Inc.). Prior to reactions, the catalyst was calcined in a muffle furnace at 580°C for 12 hr. The gas flow rate employed between 3.2 slpm and 8 slpm was in a bubbling fluidized bed flow regime. The biomass hopper is weighed before and after each run and the biomass used is calculated by difference to ensure good mass closure. After the feed auger is stopped the reactor is purged with nitrogen flow for another 20 min to “strip” any remaining product in the reactor. All of the spent catalyst is collected, transferred into alumina crucibles, and regenerated in the muffle furnace at 580˚C for 16 hr in air.

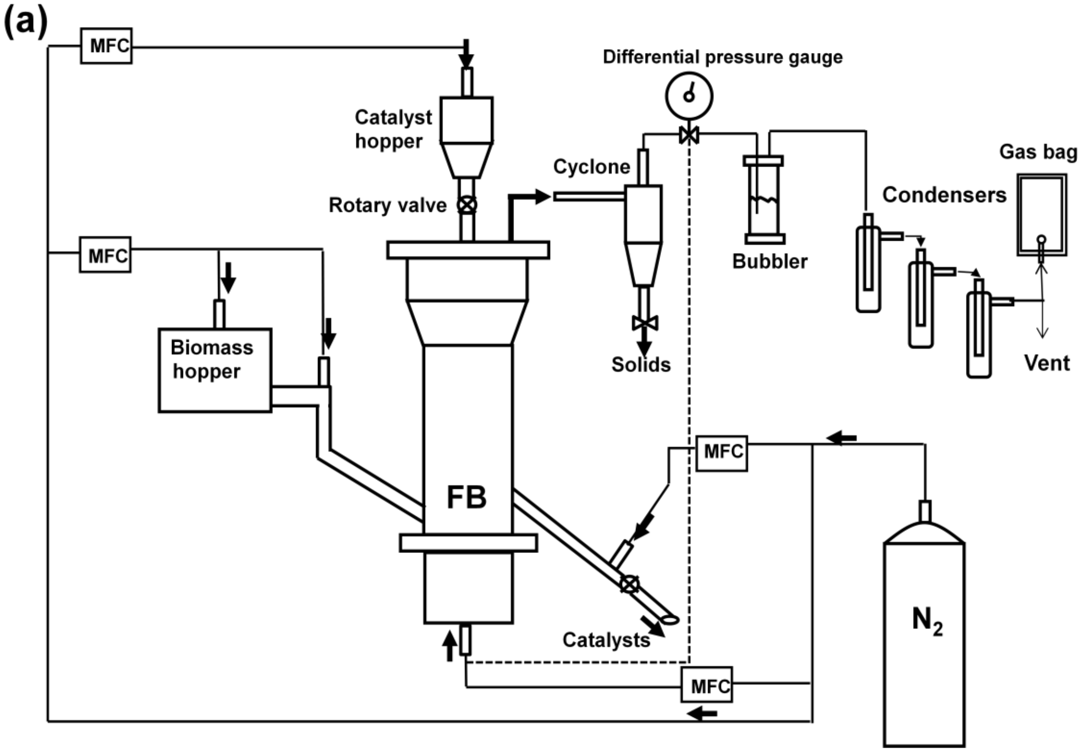

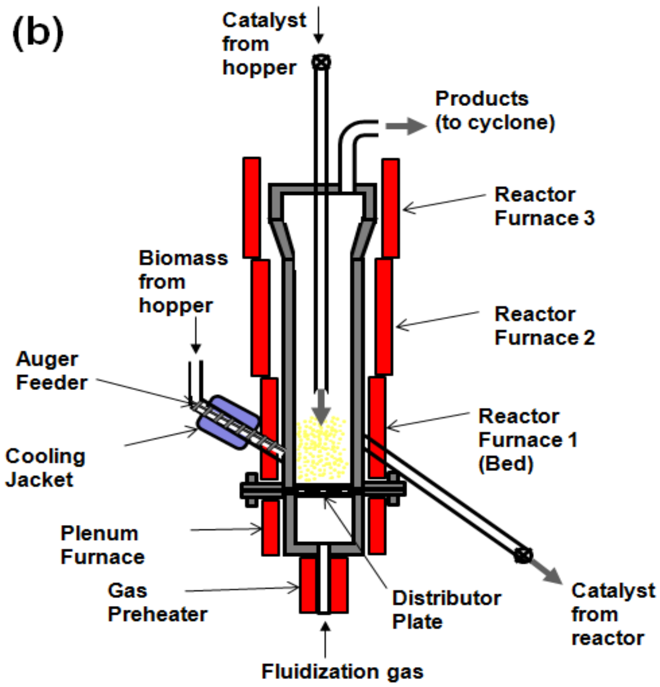

Figure 7.1 Experimental setup of the process development unit. (a) Schematic of the process development unit and (b) detailed cross-sectional drawing of the reactor

7.3 Results and Discussion

7.3.1 Catalytic Fast Pyrolysis of Pine Wood in the Process Development Unit

Experiments were conducted to determine the optimum operating conditions for CFP of pine wood in the PDU. The process parameters investigated were temperature, biomass weight hourly space velocity, catalyst to biomass ratio, static bed height, and fluidization gas flow rate.

7.3.1.1 Gas Product Yields as a Function of Time on Stream

Figure 7.2 shows the concentration of gaseous products as a function of time on stream during CFP of pinewood in the PDU at standard reaction conditions: a temperature of 600 °C, WHSV of 0.3 h^{-1}, catalyst to biomass ratio of 6. As shown, the gaseous product concentrations are almost constant with time, suggesting the reactor is operated at steady state. Decrease in product concentrations with time occurs due to catalyst deactivation by coke deposition on the catalyst surface. In the PDU, coked catalyst is continuously replaced with fresh catalyst during the reaction in order to operate the reactor with a constant level of catalytic activity. Thus, the catalyst phase can be considered as a CSTR. Since the PDU is run at steady state, all the data from the experiments of changing operating conditions were collected in a short time period (150 minute time on stream period).

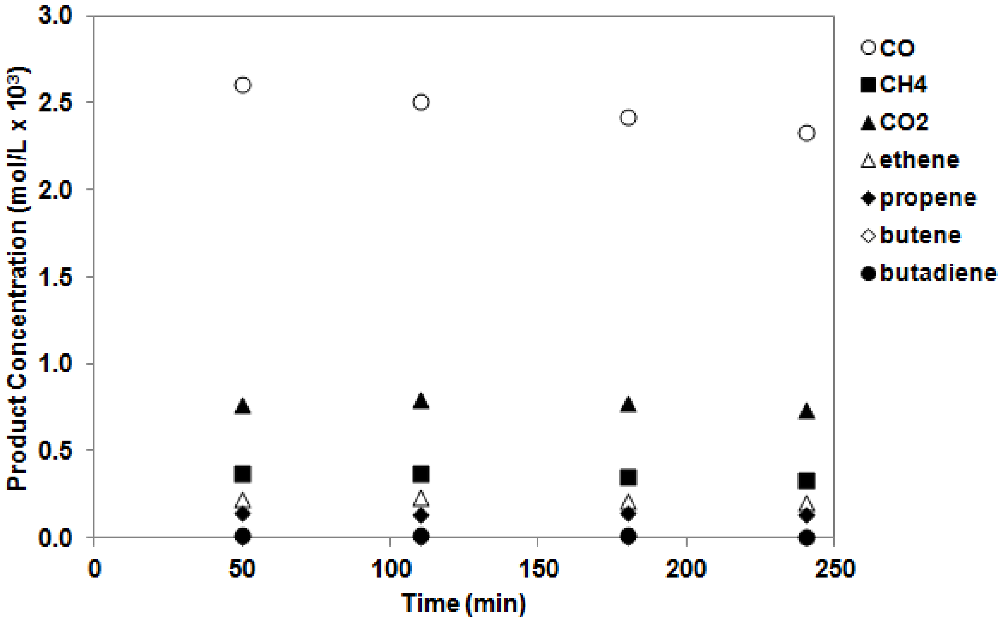

Figure 7.2 Gas phase product concentrations as a function of time on stream for catalytic fast pyrolysis of pine sawdust. Reaction conditions: ZSM-5 catalyst, pine wood feed at 0.3 WHSV, catalyst to biomass ratio of 6, 600°C reaction temperature, 5 slpm N_2 fluidization flow rate, 4 inch static bed height

7.3.1.2 Effect of Reaction Temperature

The product carbon yields for CFP of pine wood in the PDU at different temperatures are shown in Figure 7.3 and Table 7.1. During the reaction, the other operating parameters, including WHSV, catalyst to biomass ratio, fluidization gas flow rate, and static bed height, were held constant. The aromatic yield goes through a maximum of 14.2 % at 600°C. Further increasing the temperature to 650°C decreases the yield to 10.5%. Increasing the temperature increases the yield of olefins from 6.0% to 8.5%. The yields of CO, CO_2, and methane gases also increase, while increasing the temperature decreases the coke yield from 41.9% to 28.2%. These results suggest that gasification reactions are favored at higher temperatures. The detailed product yields and selectivity at different temperatures are listed in Table 7.1. The selectivities for both aromatic and olefin compounds are strong functions of temperature. The main aromatic products include benzene, toluene, xylenes, and naphthalenes. Benzene selectivity increases significantly from 17.8% to 41.2%, while xylenes (total of meta, ortho and para isomers) selectivity decreases from 29% to 9.1% as temperature increases. The olefins produced include ethylene, propylene, butene, and butadiene. Ethylene selectivity increases, whereas propylene, butane, and butadiene selectivities decrease with increasing temperature.

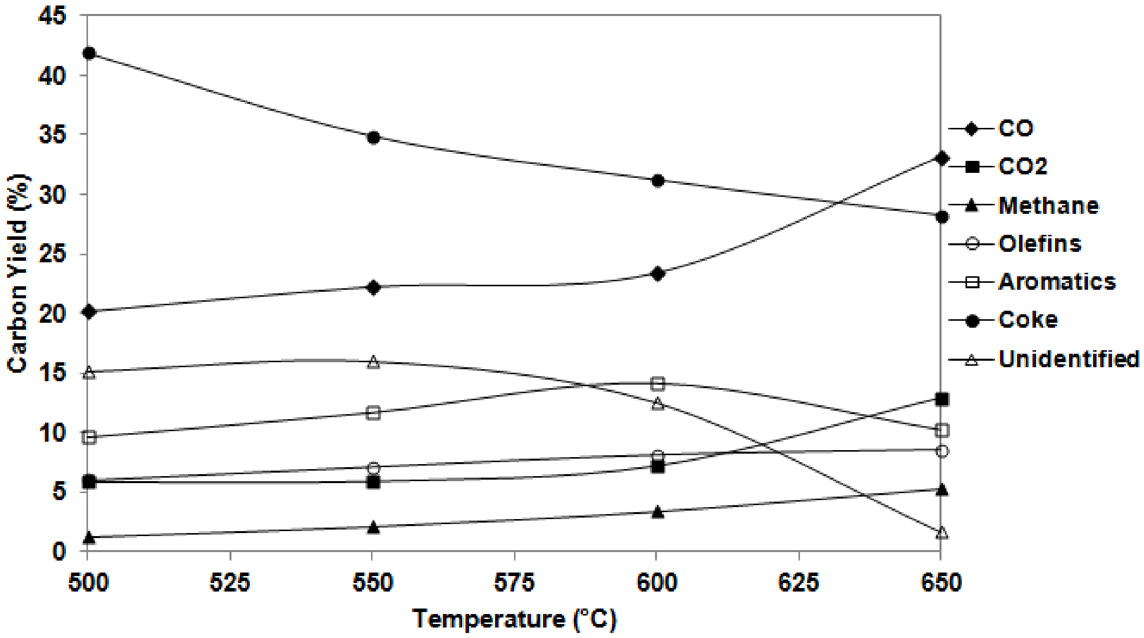

Figure 7.3 Effect of temperature on the carbon yield for CFP of pine sawdust. Reaction conditions: ZSM-5 catalyst, pine wood feed at 0.3 WHSV, catalyst to biomass ratio of 6, 5 slpm N_2 fluidization flow rate, 4 inch static bed height, and 150 min total reaction time.

Table 7.1 Detailed carbon yield distribution and product selectivity for CFP of pine wood at different temperatures. Aromatic selectivity is defined as the moles of carbon in the product divided by the total moles of aromatic carbon. Olefin selectivity is defined as the moles of carbon in the product divided by the total moles of olefin carbon.

	Temperature (°C)			
Compound	500	550	600	650
Overall Yields				
Carbon Monoxide	20.2	22.2	23.4	33.1
Carbon Dioxide	5.9	5.9	7.2	12.9
Methane	1.3	2.2	3.4	5.3
Olefins	6.0	7.1	8.1	8.5
Aromatics	9.6	11.7	14.2	10.3
Coke	41.9	34.9	31.2	28.2
Total Balance	84.9	84.0	87.5	98.3
Unidentified	15.1	16.0	12.5	1.7
Aromatic Selectivity				
Benzene	17.8	20.3	27.6	41.2
Toluene	43.3	48.5	44.9	38.7
Ethyl-Benzene	1.3	0.6	0.4	0.4
m-Xylene and p-Xylene	23.9	17.7	13.0	7.7
Styrene	0.5	0.8	1.8	3.0

o-Xylene	5.1	3.7	2.8	1.4
Benzofuran	0.4	0.4	0.2	0.2
Phenol	0.7	0.4	0.6	0.7
Indene	2.2	2.3	3.5	3.4
Naphthalenes	4.8	5.1	5.4	3.4
Light Hydrocarbon Selectivity				
Ethylene	43.1	46.1	50.8	63.3
Propylene	47.4	47.0	43.5	32.0
Butene+Butadiene	9.6	6.9	5.7	4.8

7.3.1.3 Effect of Weight Hourly Space Velocity (WHSV)

The product carbon yields for CFP of pine wood as a function of weight hourly space velocity (WHSV) are shown in Figure 7.4 and Table 7.2. During the reaction, the other operating parameters, including temperature, catalyst to biomass ratio, fluidization gas flow rate, and static bed height, were held constant. WHSV is defined as the mass flow rate of feed divided by the mass of catalyst in the reactor. A WHSV was adjusted from 0.15 to 1.0 h^{-1} by changing the biomass feed rate from 82.5 – 550 g/hr. The aromatic yield goes through a maximum at WHSV = 0.3 h^{-1}. The amount of unidentified carbon increases with increasing WHSV from 9.7% to 17.9% for 0.15 – 1 h^{-1}, respectively. The unidentified carbon is mostly from intermediate oxygenate products. These oxygenate products could be high molecular weight oligomer species which are not detectable by GC/FID and GC/MS. The CO and methane yield both increase with increasing WHSV. The yield of olefins goes through a maximum of 9.1% at WHSV = 0.6 h^{-1}. The CO_2 and coke yields decrease with increasing WHSV. WHSV also has an effect on the selectivities for aromatic and olefin products. The benzene and toluene selectivities increase, while the xylenes and naphthalenes selectivities decrease as WHSV increases from 0.3 to 1.0 hr^{-1}. The ethylene selectivity decreases, whereas the propylene, butene, and butadiene selectivities increase with increasing WHSV.

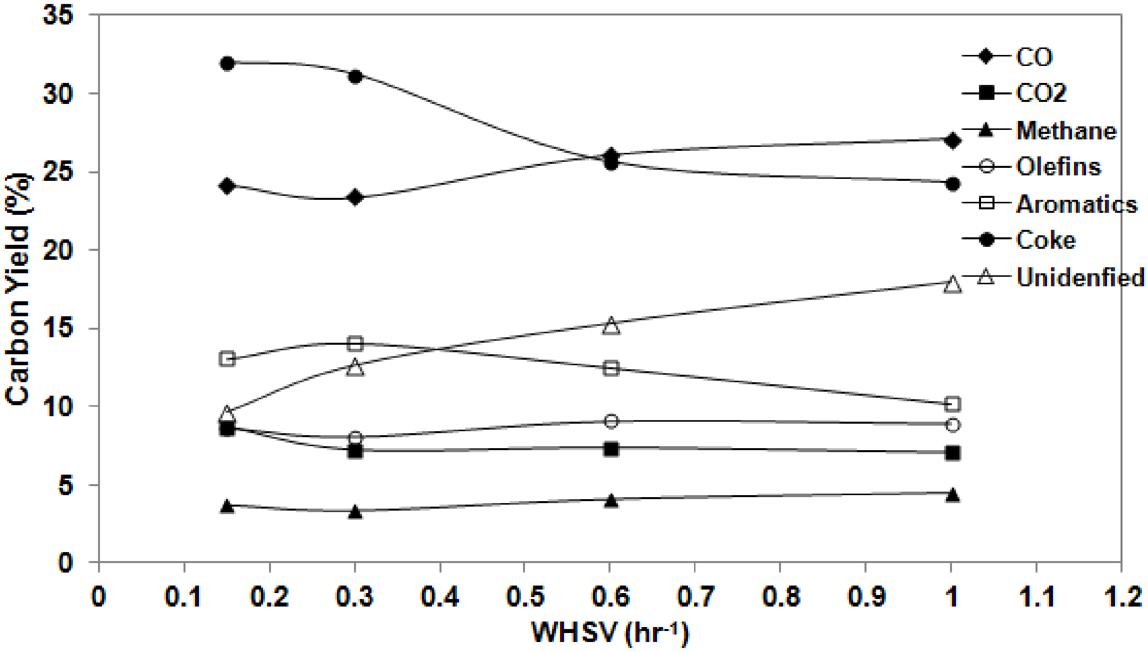

Figure 7.4 Effect of biomass WHSV on the carbon yield for CFP of pine sawdust. Reaction conditions: ZSM-5 catalyst, 600°C reaction temperature, catalyst to biomass ratio of 6, 5 slpm N_2 fluidization flow rate, 4 inch static bed height, and 150 min total reaction time. WHSV is defined as the mass flow rate of feed divided by the mass of catalyst in the reactor.

Table 7.2 Detailed carbon yield distribution and product selectivity for CFP of pine wood at different biomass WHSV.

	WHSV (hr^{-1})			
Compound	0.15	0.3	0.6	1.0
Overall Yields				
Carbon Monoxide	24.2	23.4	26.1	27.1
Carbon Dioxide	8.7	7.2	7.3	7.0
Methane	3.7	3.4	4.1	4.5
Olefins	8.7	8.1	9.1	8.9
Aromatics	13.1	14.1	12.5	10.2
Coke	32.0	31.2	25.6	24.3
Total balance	90.3	87.4	84.7	82.1
Unidentified	9.7	12.6	15.3	17.9
Aromatic Selectivity				
Benzene	37.5	27.6	29.8	32.2
Toluene	42.7	44.9	46.4	46.9

Ethyl-Benzene	0.3	0.4	0.7	0.7
m-Xylene and p-Xylene	9.2	13.0	11.3	10.5
Styrene	0.9	1.8	1.7	1.6
o-Xylene	2.0	2.8	2.3	2.6
Benzofuran	0.1	0.2	0.3	0.4
Phenol	0.2	0.6	0.6	0.3
Indene	3.9	3.5	2.5	2.2
Naphthalenes	3.2	5.4	4.3	2.6
Light Hydrocarbon Selectivity				
Ethylene	53.3	50.8	44.2	42.8
Propylene	43.9	43.5	46.3	46.1
Butene+Butadiene	2.8	5.7	9.5	11.1

7.3.1.4 Effect of Catalyst to Biomass Ratio

Figure 7.5 and Table 7.3 show product yields as a function of catalyst to biomass ratio for CFP of pine wood. During the reaction, the other operating parameters were held constant. Catalyst to biomass ratio is defined as the mass flow rate of catalyst divided by the mass flow rate of feed. A catalyst to biomass ratio of 3 - 9 was adjusted by changing the catalyst feed rate between 540 and 1530 g/hr. In addition, changing the catalyst to biomass ratio is directly related to the catalyst residence time in the reactor. Catalyst residence time can be defined as the mass flow rate of catalyst divided by the mass of catalyst in the reactor. Varying the catalyst feed rate from 540 to 1530 g/hr changes the catalyst residence time from 60 to 20 minutes. Therefore, increase of the catalyst to biomass ratio decreases the catalyst residence time. As shown in Figure 7.5, the aromatic and olefin yields both increase with increasing the catalyst to biomass ratio and decreasing the catalyst residence time. The highest aromatic yield of 14.2 % was obtained at a catalyst to biomass ratio of 6 and catalyst residence time of 30 minutes. The amount of coke produced decreases with increasing the catalyst to biomass ratio and decreasing the catalyst residence time. As the catalyst to biomass ratio decreases and the catalyst residence time increases, the reaction occurs with more coked catalyst. For instance, the amount of coke on the catalyst decreases from 4.1 to 1.7 wt% as the catalyst to biomass ratio increases from 3 to 9. Hence, less concentration of active sites is available with higher amounts of coked catalyst. This might have a negative effect on the desired chemistry for aromatic production. For this reason, the yields of aromatics and olefins are low, whereas undesired coke and methane formation are high at a low catalyst to biomass ratio. However, the selectivities for the aromatic and olefin compounds do not change significantly with the catalyst to biomass ratio.

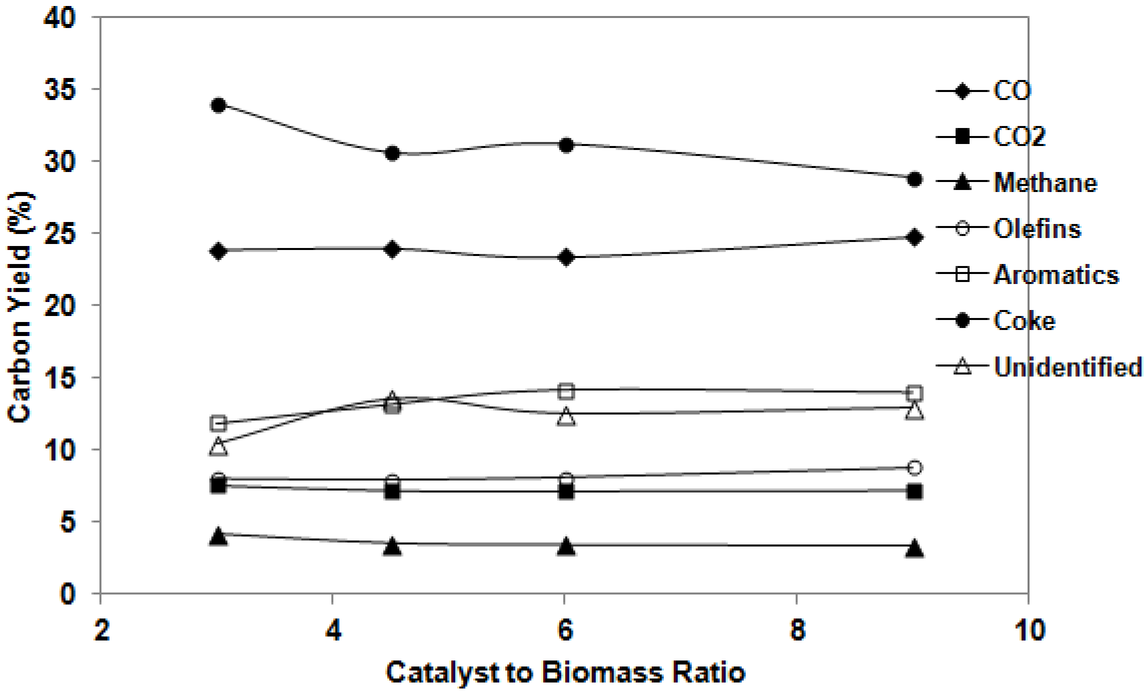

Figure 7.5 Effect of catalyst to biomass ratio on the carbon yield for CFP of pine sawdust. Reaction conditions: ZSM-5 catalyst, 0.3 wood WHSV, 600°C reaction temperature, 5 slpm N_2 fluidization flow rate, 4 inch static bed height, and 150 min total reaction time. Catalyst to biomass ratio is defined as the mass flow rate of catalyst divided by the mass flow rate of feed.

Table 7.3 Detailed carbon yield distribution and product selectivity for CFP of pine wood at different catalyst to biomass ratios.

	Catalyst to biomass ratio			
Compound	3.0	4.5	6.0	9.0
Overall Yields				
Carbon Monoxide	23.9	24.2	23.4	24.8
Carbon Dioxide	7.6	7.2	7.2	7.2
Methane	4.2	3.5	3.4	3.3
Olefins	8.0	7.9	8.1	8.8
Aromatics	11.9	13.1	14.2	13.9
Coke	34.0	30.6	31.2	28.9
Total balance	89.6	86.5	87.5	87.1
Unidentified	10.4	13.5	12.5	12.9
Aromatic Selectivity				
Benzene	28.5	29.8	27.6	28.8
Toluene	47.3	46.2	44.9	48.9
Ethyl-Benzene	0.6	0.6	0.4	0.5
m-Xylene and p-Xylene	12.1	12.3	13.0	12.0
Styrene	1.9	1.8	1.8	1.5
o-Xylene	2.4	2.5	2.8	2.5
Benzofuran	0.3	0.2	0.2	0.2
Phenol	0.5	0.5	0.6	0.4
Inden	2.6	2.5	3.5	2.0
Naphthalene	3.8	3.6	5.4	3.3
Light Hydrocarbon Selectivity				
Ethylene	49.6	50.6	50.8	48.5
Propylene	41.8	41.7	43.5	43.2
Butene+Butadiene	8.6	7.7	5.7	8.2

7.3.1.5 Effect of Static Bed Height

The effect of static bed height on the product yield for CFP of pine wood at temperate of 600 °C, biomass WHSV of 0.3 h^{-1}, catalyst to biomass ratio of 6, and fluidization gas flow rate of 5 slpm, is shown in Figure 7.6. Static bed height is defined as the height of the catalyst level above the distributor plate. The static bed height was adjusted by varying the mass of catalyst in the reactor. The static bed height is directly related to the fraction of the reactor volume occupied by the catalyst. Thus, the operation of the reactor with a high bed height is important for industrial application because the operation of the reactor with a higher bed height means higher reactor efficiency by processing more biomass at given reaction conditions. However, changing the bed height influences the vapor residence time, which is defined as the reactor volume occupied by the catalyst divided by the volumetric gas flow rate. A higher bed height means a longer vapor residence time (more contact between the reactants and the catalyst) in the reactor. For instance, an increase of the static bed height from 4 to 8 inch increases the vapor residence time from 5.2 to 9.6 sec. As shown in Figure 7.6, the aromatic and unidentified oxygenate yields decrease with increasing the static bed height, while the CO, CO_2, methane, and coke yields show the opposite trend. The highest aromatic yield of 14.2 % was obtained at the lowest static bed height (4 inch) and the shortest vapor residence time (5.2 sec) among the tested range. Decrease of the unconverted oxygenates yields could be explained by the longer residence time of the vapor in the reactor. However, it appears that the long residence time promotes secondary reactions in the catalyst. These undesired secondary reactions might cause a decrease in the aromatic yield and an increase in the coke and gas yields by the secondary cracking of the vapor. Similar results have been reported from catalytic pyrolysis of corncobs[27]. The selectivity for aromatic compounds is also influenced by the static bed height as shown in Table 7.4. Both benzene and toluene carbon selectivities slightly increase with increasing the bed height, while xylenes and naphthalenes show the opposite trend.

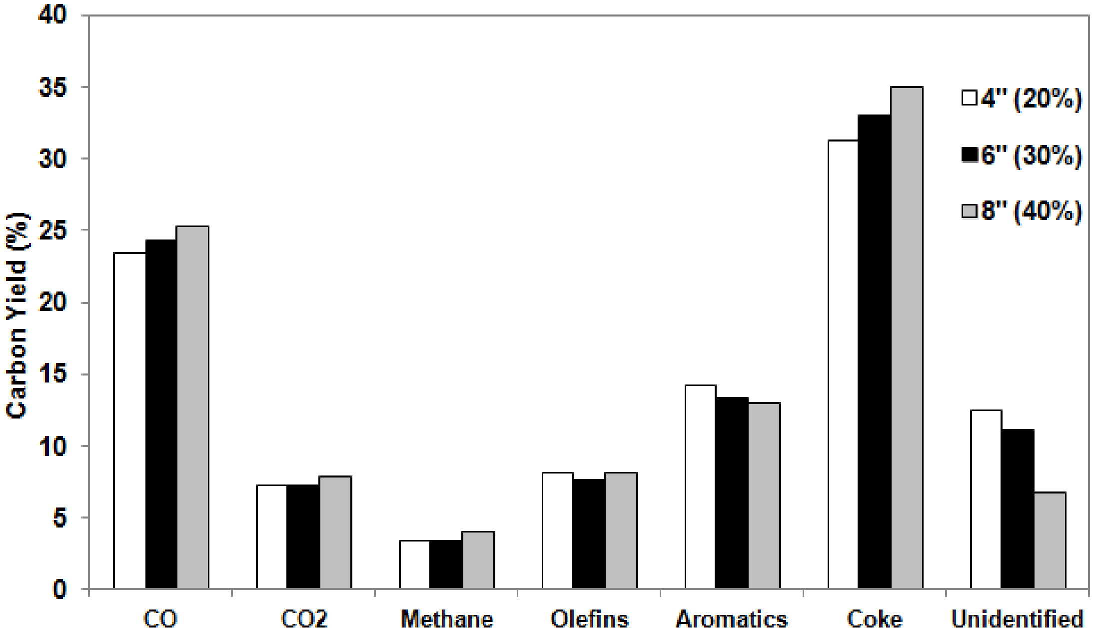

Figure 7.6 Effect of static bed height on the carbon yield for CFP of pine sawdust. Reaction conditions: ZSM-5 catalyst, 0.3 wood WHSV, catalyst to biomass ratio of 6, 600°C reaction temperature, 5 slpm N_2 fluidization flow rate, and 150 min total reaction time. ( ) represents the fraction of the reactor volume occupied by the catalyst.

Table 7.4 Detailed carbon yield distribution and product selectivity for CFP of pine wood at different static bed heights.

	Static bed height (inch)		
Compound	4	6	8
Overall Yields			
Carbon Monoxide	23.4	24.3	25.2
Carbon Dioxide	7.2	7.2	7.9
Methane	3.4	3.4	4.0
Olefins	8.1	7.6	8.1
Aromatics	14.2	13.3	13.0
Coke	31.2	33.0	34.9
Total balance	87.5	88.9	93.2
Unidentified	12.5	11.1	6.8
Aromatic Selectivity			
Benzene	27.6	29.0	30.8
Toluene	44.9	46.5	47.6
Ethyl-Benzene	0.4	0.5	0.4
m-Xylene and p-Xylene	13.0	12.1	10.6

Styrene	1.8	1.5	1.2
o-Xylene	2.8	2.9	2.5
Benzofuran	0.2	0.2	0.3
Phenol	0.6	0.4	0.3
Indene	3.5	2.6	2.1
Naphthalenes	5.4	4.4	4.2
Light Hydrocarbon Selectivity			
Ethylene	50.8	51.7	49.7
Propylene	43.5	42.0	43.5
Butene+Butadiene	5.7	6.3	6.7

7.3.1.6 Effect of Fluidization Gas Flow Rate

The effect of fluidization gas flow rate on the product yield for CFP of pine wood at temperate of 600 °C, biomass WHSV of 0.3 h^{-1}, catalyst to biomass ratio of 6, and static bed height of 4 inch, is shown in Figure 7.7. In the fluidized bed reactor, fluidization gas flow rate is directly related to bubble formation and growth. Bubbles can form between the dense bed when fluidization gas velocity is typically 4 to 10 fold higher than minimum fluidization velocity[194]. The size of bubbles increases with increasing gas flow rates [195]. In general, the bubbles formed create good mixing and good gas-solid contact. As shown in Figure 7.7, the aromatic and coke yields decrease, while the CO, olefins, and unidentified oxygenates yield increase with increasing fluidization gas flow rates. The maximum aromatic yield of 15.1 % was obtained at the lowest fluidization gas flow rate (3.2 slpm). These results suggest that change in the bubble size impacts the reaction chemistry. Higher flow rates mean larger bubble size where the gas inside the bubbles has poor interaction with the catalysts [196]. Therefore, the large bubbles formed by high gas flow rates could result in an increase in the unidentified oxygenates yield and a decrease in the aromatic yield due to poor gas-catalyst interaction. The selectivities for aromatic and olefin compounds also show a trend as shown in Table 7.5. Benzene and toluene carbon selectivities both slightly increase with increasing the gas flow rate, while xylenes and naphthalenes show the opposite trend. Ethylene selectivity decreases, whereas butene and butadiene selectivity increases with an increase in gas flow rate.

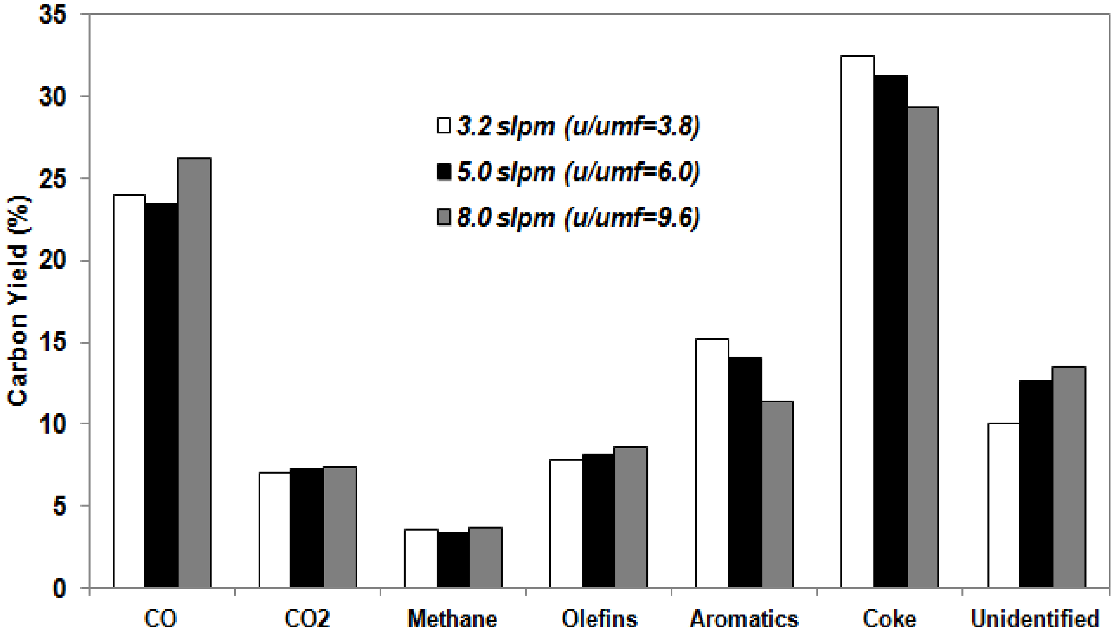

Figure 7.7 Effect of fluidization gas flow rates on the carbon yield for CFP of pine sawdust. Reaction conditions: ZSM-5 catalyst, 0.3 wood WHSV, catalyst to biomass ratio of 6, 600°C reaction temperature, 4 inch static bed height, and 150 min total reaction time. u/u_{mf} is the ratio of fluidization gas velocity to minimum fluidization gas velocity.

Table 7.5 Detailed carbon yield distribution and product selectivity for CFP of pine wood at different fluidization gas flow rates.

	N_2 flow rate (slpm)		
Compound	3.2	5.0	8.0
Overall Yields			
Carbon Monoxide	24.0	23.4	26.2
Carbon Dioxide	7.0	7.2	7.3
Methane	3.5	3.4	3.6
Olefins	7.8	8.1	8.6
Aromatics	15.1	14.1	11.4
Coke	32.5	31.2	29.3
Total balance	89.9	87.4	86.5
Unidentified	10.1	12.6	13.5

Aromatic Selectivity			
Benzene	27.5	27.6	34.7
Toluene	44.1	44.9	46.6
Ethyl-Benzene	0.4	0.4	0.5
m-Xylene and p-Xylene	14.7	13.0	9.8
Styrene	1.7	1.8	1.6
o-Xylene	2.8	2.8	1.9
Benzofuran	0.2	0.2	0.2
Phenol	0.3	0.6	0.4
Indene	2.8	3.5	2.1
Naphthalenes	5.6	5.4	2.3
Light Hydrocarbon Selectivity			
Ethylene	53.5	50.8	50.0
Propylene	40.6	43.5	41.6
Butene+Butadiene	5.9	5.7	8.5

7.3.1.7 Comparison of CFP in the Process Development Unit with CFP in the Lab Scale Fluidized Bed Reactor

As a result of our investigations, the optimal operating conditions for CFP of pine wood in the process development were found to be: a temperature of 600 °C, WHSV of 0.3 h^{-1}, catalyst to biomass ratio of 6, fluidization gas flow rate of 3.2 slpm, and static bed height of 4 inch. At these conditions, the highest aromatic yield of 15.1 % and the olefin yield of 7.8% were obtained. These results were compared with the optimized yields from CFP in the semi-continuous lab-scale fluidized bed reactor as shown in Table 7.6. The total reaction time in the process development unit is five times longer than that in the lab-scale fluidized bed reactor. The aromatic yield is slightly higher in the process development unit than the lab scale fluidized bed reactor, showing the ability of the process development unit for prolonged operations while maintaining a high yield of aromatics. However, the olefin yield is higher in the lab scale fluidized bed reactor. The process development unit produces more benzene and toluene and less naphthalene than the lab-scale fluidized bed reactor, suggesting that the two reactors have slightly different reaction environments.

Table 7.6 Comparison of the lab scale fluidized bed reactor with the process development unit at the optimized reaction conditions: for the lab-scale fluidized bed reactor, ZSM-5 catalyst, temperature 600°C, 0.35 wood WHSV, gas flow rate of 1.0 slpm, 30 min reaction time and for the process development unit, ZSM-5 catalyst, temperature 600℃, 0.3 wood WHSV, catalyst to biomass ratio of 6, gas flow rate of 3.2 slpm, 4 inch static bed height, 150 min reaction time. Pine wood sawdust was used as a feed for both reactors.

	Lab scale FB	**PDU**
Overall yields		
CO	32.2	24.0
CO_2	9.5	7.0
Methane	4.3	3.5
Olefins	9.4	7.8
Aromatics	13.9	15.1
Coke	26.7	32.5
Total balance	96.4	89.9
Unidentified	3.6	10.1
Aromatic selectivity		
Benzene	20.8	27.5
Toluene	37.1	44.1
Ethyl-benzene	2.3	0.4
p-and *m*-Xylene	16.6	14.7
o-Xylene	3.2	2.8
Styrene	2.8	1.7
Benzofuran	1.9	0.2
Indene	2.6	2.8
Phenol	1.4	0.3
Naphthalene	11.2	5.6
Olefin selectivity		
Ethylene	52.8	53.5
Propylene	36	40.6
Butenes	11.2	5.9

7.3.1.8 Continuous Operation for the Production of 1 L Aromatics

We have produced 1 L of aromatics from pine wood in the process development unit. To achieve this, the process development unit was operated daily. A typical run lasted for 4 to 5 hrs per day. The longest operation was 7 hrs. After each run, the liquid products in the dry ice condensers were collected and the total volume of the liquid was recorded. To obtain pure aromatic products, ethanol solvent was not used in each condenser. Because using the condensers without ethanol solvent was unable to capture all of the aromatic effluents, about 20 to 30% of aromatics were lost in the gas phase. The spent catalyst was then collected and regenerated in the muffle furnace at 580 °C for 16 - 20 hours and used for the next run. Hence, the same HZSM-5 catalyst was used for the entire run through successive reaction-regeneration cycles. The reaction was carried out using the spray-dried ZSM-5 catalyst at the optimal operating conditions: temperature of 600 °C, WHSV of 0.3 h^{-1}, catalyst to biomass ratio of 6, fluidization gas flow rate of 5-6 slpm, and static bed height of 4 inch. Table 7.7 shows the detailed summary report for each run. Total operation hours of the PDU were over 120 hrs and more than 20 kg of pine wood was used. The aromatic products produced were over 1 L.

Table 7.7 A detailed report about each run during three months. Liquid products (ml) are the liquid samples collected from dry ice condensers which consist mostly of aromatics.

Date	Sample Code	Gas velocity (SLPM)	WHSV (h^{-1})	Catalyst regeneration cycle	Operation hour (min)	Biomass used (g)	Liquid products (ml)
8-Jun	Bayer	7	0.33	2	218	604.7	N.q
10-Jun	Bayer	7	0.3	3	155	397.7	N.q
13-Jun	Bayer	7	0.39	4	155	503.3	N.q
14-Jun	Bayer	6	0.37	5	220	681.8	N.q
16-Jun	Bayer	5	0.36	6	240	728.6	N.q
20-Jun	Flint Hills	6	0.3	7	270	680.0	N.q
21-Jun	DARPA	6	0.446	8	270	1004.4	N.q
22-Jun	DARPA	6	0.31	9	270	699.2	50
24-Jun	DARPA	6	0.28	10	255	601.5	46
27-Jun	DARPA	6	0.29	11	377	1001	71
29-Jun	DARPA	6	0.31	12	330	948	59
1-Jul	DARPA	5	0.31	13	300	853	52
6-Jul	DARPA	5	0.32	14	368	1074	66
8-Jul	DARPA	5	0.32	15	333	983.7	60
11-Jul	DARPA	5	0.35	16	285	1007.2	64
13-Jul	DARPA	5	0.35	17	330	1068	64
18-Jul	DARPA	5	0.35	18	305	1072	66
20-Jul	DARPA	6	0.30	19	320	955.5	60
22-Jul	DARPA	4.5	0.22	20	240	529.5	32
25-Jul	DARPA	5	0.33	21	353	1076	68
27-Jul	DARPA	5	0.34	22	410	1278.7	66

1-Aug	DARPA	5	0.37	23	410	1402.0	71
30-Aug	DARPA	5	0.41	24	265	998.6	53
31-Aug	DARPA	5	0.45	25	235	998.4	53
2-Sep	DARPA	5	0.35	26	240	773.9	40

Figure 7.8 shows photographs of the raw liquid products and pure aromatic samples obtained by distillation of the raw liquid products. The initial liquid product obtained from the PDU was dark brown. This could be due to the small amount of furfural in the samples. After simple distillation of the raw liquid products using a rotary evaporator, we were able to obtain pure aromatic samples consisting mainly of benzene, toluene, and xylenes.

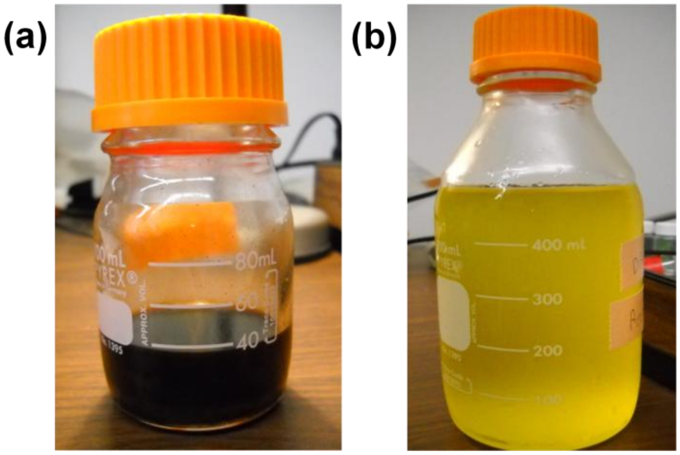

Figure 7.8 Liquid products produced in the process development unit. (a) raw liquid products and (b) pure aromatic samples obtained after distillation of the raw liquid products.

7.3.2 Stability of the Catalyst in Reaction-Regeneration Cycles

To study the stability of the ZSM-5 catalyst during CFP, the catalyst was subjected to up to 30 successive reaction-regeneration cycles. The catalyst was exposed to a total reaction time of over 150 hrs and a total regeneration time of over 540 hrs. For each cycle the reaction was performed for 4 - 5 hours at the standard conditions: temperature of 600

°C, WHSV of 0.3 h^{-1}, catalyst to biomass ratio of 6, fluidization gas flow rate of 5 - 6 slpm, and static bed height of 4 inch. After reaction the catalyst was regenerated in air at 580 °C for 16 - 20 hours. After 30 reaction-regeneration cycles the catalyst was studied with XRD, SEM, ammonia TPD, and in situ FT-IR to investigate the physical and chemical stability during CFP. The catalyst was also tested at the standard reaction conditions using pine wood as a feed to compare the product yield and distribution with the fresh catalyst.

7.3.2.1 Product Yield

Figure 7.9 shows the product yield for CFP of pine wood at the optimal operating conditions with the fresh catalyst and the catalysts after 5 and 30 reaction-generation cycles. For the carbon yields of olefins, CO, CO_2, and methane, the catalysts after 5 and 30 reaction-regeneration cycles show similar results as compared to the fresh catalyst. However, there is a slight decrease in the aromatic yield from 14.2% to 13.1% after the fifth regeneration. Then, there is another decrease in the aromatic yield from 13.1% to 12.2% after the thirtieth regeneration. These results suggest that the catalyst steadily loses its activity in successive reaction-regeneration cycles. However, a comparison between 5 cycles and 30 cycles shows that the decrease becomes less significant as the number of cycles increases.

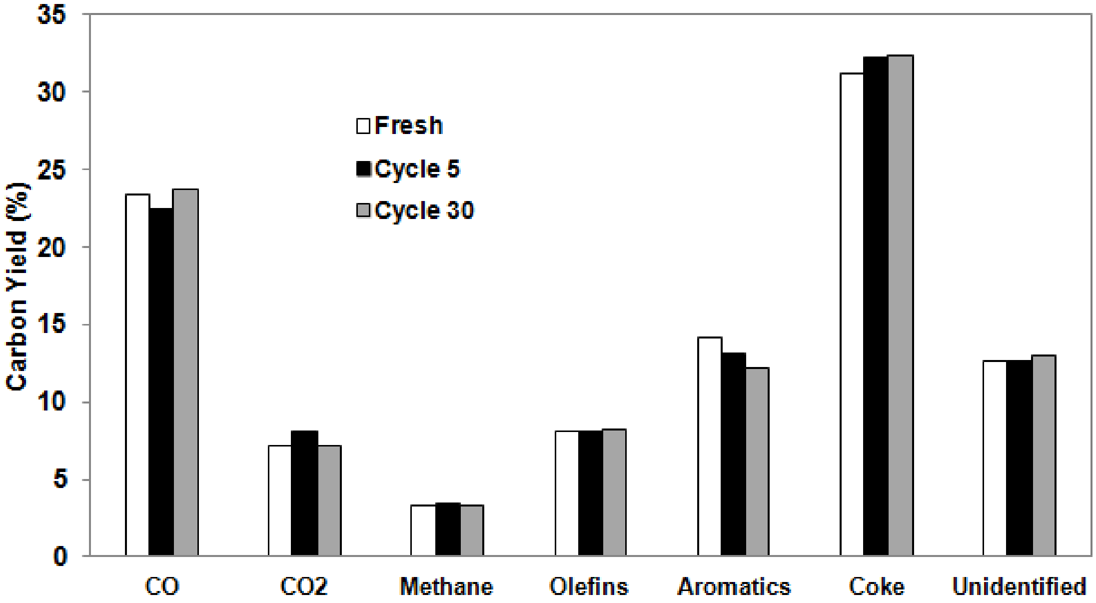

Figure 7.9 Catalytic fast pyrolysis of pine wood with a fresh ZSM-5, the ZSM-5 after 5 reaction-regeneration cycles, and the ZSM-5 after 30 reaction-regeneration cycles. Reaction conditions: 0.3 wood WHSV, catalyst to biomass ratio of 6, 600°C reaction temperature, 4 inch static bed height, 5 slpm N_2 fluidization flow rate, and 150 min total reaction time.

7.3.2.2 Catalyst Characterization

The temperature programmed oxidation curves of the separated char and the coked catalyst are shown in Figure 7.10. After reaction, the collected spent catalyst contained some char particles. The char was separated from the catalyst by sieving using 120 mesh (See Figure 7.11). The morphology of char particles has significantly different characteristics from catalyst particles. The separated char and the spent catalyst were combusted at a ramping rate of 5°C/min to 600°C in the TGA, respectively. As shown in Figure 7.10, the char contains significantly more carbon (~12%) than the spent catalyst (~2%). In addition, this result shows that 88% of char content is non-combustible minerals (i.e. ash), suggesting that the minerals likely accumulated in the catalyst during successive reaction-regeneration cycles.

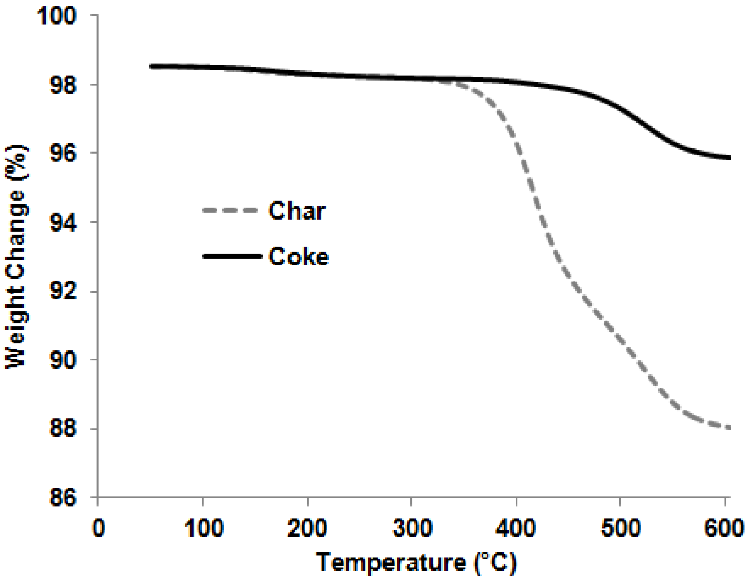

Figure 7.10 TPO curves in the combustion of the char (carbon from pyrolysis of wood) and the coked catalyst (carbon deposited on the catalyst).

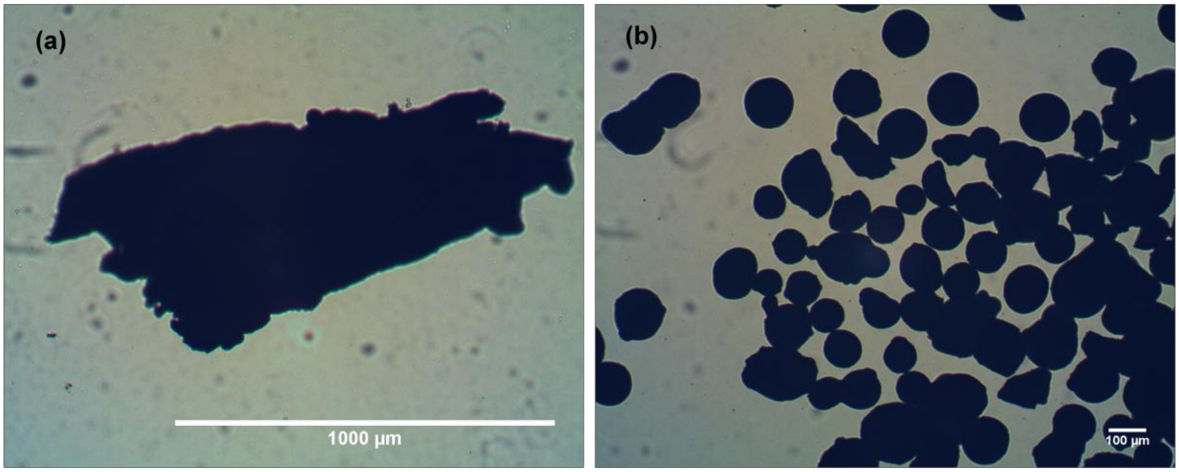

Figure 7.11 Optical microscope images of (a) the separated char and (b) the coked catalyst.

Figure 7.12 shows the X-ray diffraction patterns of measurements of the fresh ZSM-5 and the ZSM-5 after 30 reaction-regeneration cycles. The crystal structure and crystallinity of the ZSM-5 were intact after 30 reaction-regeneration cycles. SEM images were recorded for the catalysts (Figure 7.13). The ZSM-5 catalyst after 30 reaction-regeneration cycles shows some broken pieces of catalyst particles. This could result from the collision between catalyst particles in the fluidized bed reactor.

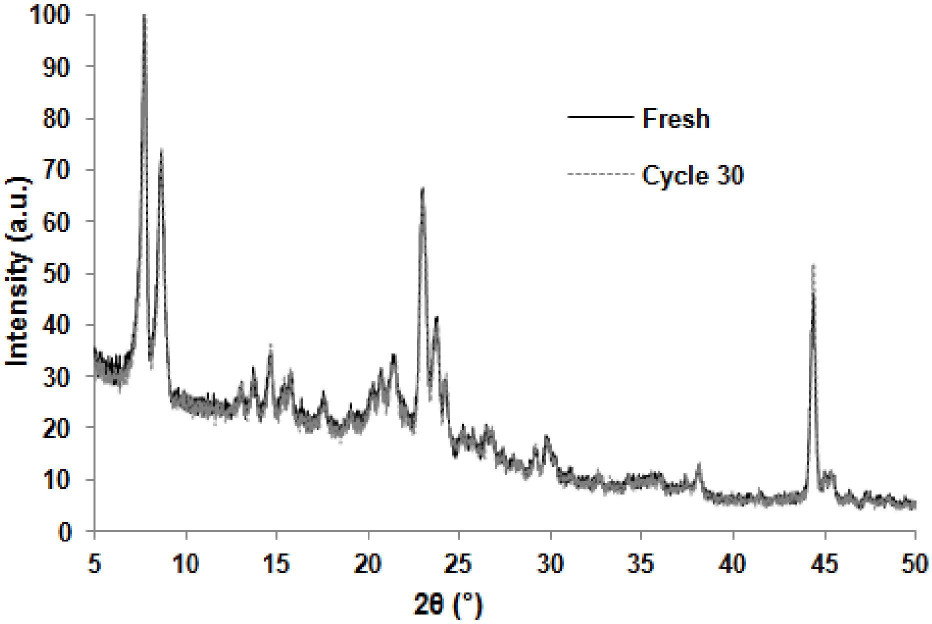

Figure 7.12 X-ray diffraction patterns of the fresh catalyst and the catalyst after 30 reaction-regeneration cycles.

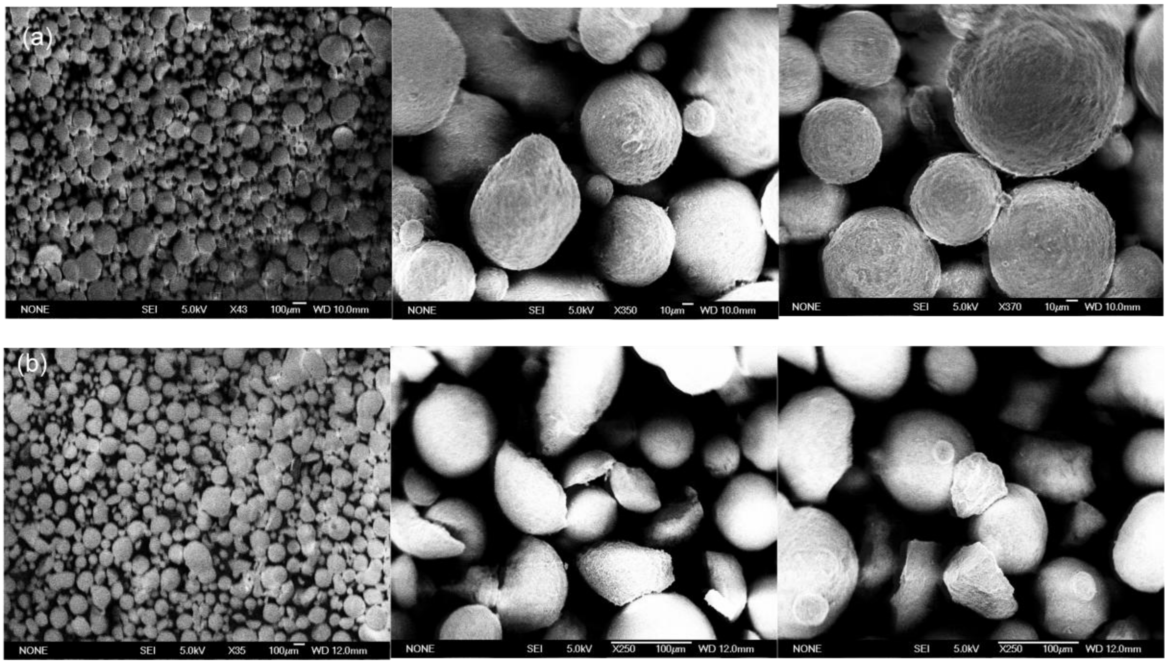

Figure 7.13 SEM images of (a) the fresh catalyst and (b) the catalyst after 30 reaction-regeneration cycles.

The total number of acid sites for the fresh ZSM-5 and the ZSM-5 after 30 reaction-regeneration cycles was measured using temperature programmed desorption (TPD) of ammonia, as shown in Figure 7.14 and Table 7.8. NH_3 TPD curves show a significant loss in acidity of the catalyst after 30 reaction-regeneration cycles from the decrease of the peak intensity. As reported in Table 7.8, the total number of acid sites decreases from 0.35 to 0.23. This loss in acidity could be attributed to ash from the biomass, poisoning the acid sites (See Figure 7.10 and 7.11). Another possible reason for loss in acidities is that dealumination within the catalyst occurs at reaction conditions in which water vapor is present at high temperatures [197].

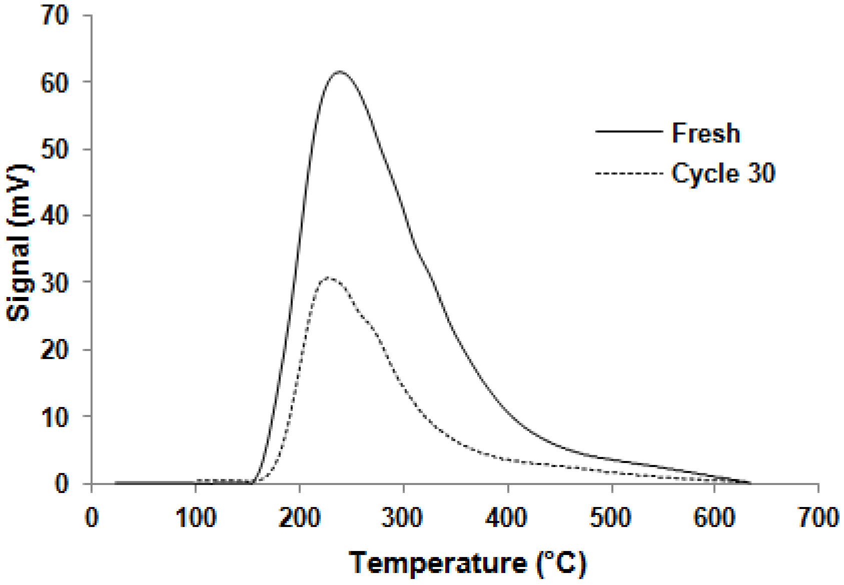

Figure 7.14 Temperature programmed desorption of ammonia for the fresh catalyst and the catalyst after 30 reaction-regeneration cycles.

Table 7.8 Total acidity of the fresh catalyst and the catalyst after 30 reaction-regeneration cycles.

	Total Acidity (mmol NH3/g catalyst)
Fresh	0.35
Cycle 30	0.23

Figure 7.15 shows the in situ DRIFTS spectra of ammonia adsorbed on the fresh ZSM-5 and the ZSM-5 after 30 reaction-regeneration cycles. The spectra of the fresh and the regenerated catalysts show the same features, however, the fresh catalyst shows a stronger band at 3610 cm^{-1} assigned to the OH vibration associated with Bronsted acid sites. The bands observed for the ZSM-5 with ammonia adsorbed are assigned in Table 7.7. The Bronsted to Lewis site ratio can be obtained from the ratio of Bronsted and Lewis band heights (1478 cm^{-1} and 1614 cm^{-1} respectively). There is a decrease in the Bronsted/Lewis site ratio from 1.5 to 1.2 between the fresh catalyst and the catalyst after 30 reaction-regeneration cycles, indicating a loss of some of the Bronsted acid sites. This is likely due to the ash from biomass or dealumination by steaming.

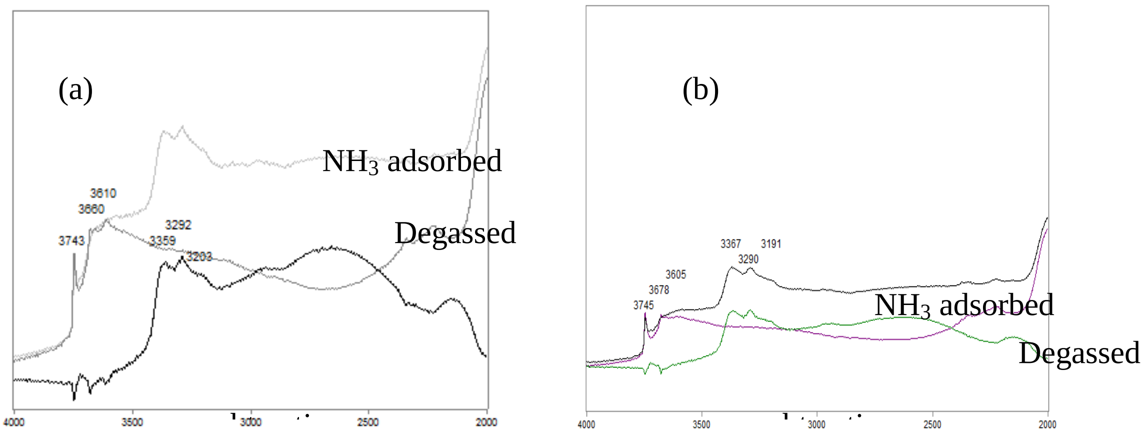

Figure 7.15 In situ DRIFTS spectra of ammonia adsorbed on (a) the fresh catalyst and (b) the catalyst after 30 reaction-regeneration cycles.

Table 7.9 Band positions and assignments of DRIFTS spectra of ammonia adsorbed on the ZSM-5 catalyst.

Band Position (cm^{-1})	Assignment	Species
3745	ν(OH)	Si-OH terminal silanols
3679	ν(OH)	Si-OH or Extra framework Al
3605	ν(OH)	α-cages or Al-OH Extra framework Al
3367	ν(NH)	Si-NH-Al
3290	ν(NH)	Si-NH2…Al
3191	ν(NH)	NH_4^+ Bronsted site
1614	(NH2)	Lewis site
1478	(NH2)	Bronsted site

7.4 Conclusions

In this study we conducted catalytic fast pyrolysis of pine wood using a spray-dried ZSM-5 catalyst in the process development unit. The process development unit was designed and built for continuous operation of the CFP process at steady state over a long duration. The effects of operating parameters on the yield and selectivity of aromatic and olefin products were studied to optimize the reactor performance. The highest aromatic yield was obtained at a intermediate temperature (600 °C), a low biomass weight hourly space velocity (0.3 h^{-1}), and a high catalyst to biomass ratio (6 to 9). Aside from these conditions, the static bed height should be low (4 inch) to avoid a secondary coking reaction from an increased bed height. The fluidization gas velocity should be low (3.2 slpm, u/u_{mf}=3.8) to keep the size of the bubbles small for good gas-catalyst contact. The highest aromatic yield of 15.1% and the olefin yield of 7.8% were obtained at the optimized operating conditions. The aromatic yield from CFP in the process development unit was comparable to the semi-continuous lab scale fluidized bed reactor at the optimized conditions, showing the ability of the process development unit for prolonged operations while maintaining a high yield of aromatics. The stability of the ZSM-5 catalyst during extended operation was studied over 30 successive reaction-regeneration cycles. The catalyst showed a slight decrease in the aromatic yield after 30 successive reaction-regeneration cycles by irreversible deactivation. The concentration of acid sites on the catalyst was reduced by 70% of the fresh catalyst after 30 reaction-regeneration cycles. This loss in acidity could be attributed to mineral impurities from the biomass, poisoning acid sites or dealumination by steaming.

CHAPTER 8

CONCLUSIONS AND FUTURE WORK

8.1 Conclusions

The objective of this thesis was to advance CFP technology by studying the reaction chemistry for CFP, developing the optimized zeolite catalysts for CFP, and demonstrating the scale-up of the CFP process in a process development unit. To gain a fundamental understanding of the underlying chemistry of CFP, we have examined both the homogeneous and heterogeneous reactions for CFP of glucose (a model compound for cellulose). A combination of milligram-scale pyroprobe reactor, TG/DTG system, ex-situ FTIR characterization, and isotopic labeling experiments was used to investigate the intermediate and final products of the reaction in the absence and presence of the ZSM-5 catalyst. The reaction network for the conversion of glucose to aromatics was proposed based on the experimental evidence.

CFP of glucose involves two steps. Glucose initially thermally decomposes through two different pathways. At high temperatures glucose is dehydrated into anhydrosugars which are then converted by dehydration reactions into furans. At low temperature, glucose is decomposed to dihydroxyacetone and glyceraldehydes through retro-aldol condensation. Both decomposition pathways can occur homogeneously or on the catalyst. The oxygenates produced from thermal decomposition then diffuse into the ZSM-5 pores where they are converted into aromatics, CO, CO_2, and water through a series of dehydration, decarbonylation, decarboxylation, and oligomerization reactions. The isotopic labeling studies revealed that the monocyclic aromatics are formed from random hydrocarbon fragments which are most likely produced from a "hydrocarbon pool" inside the zeolite, while naphthalene is produced via the combination of monocyclic aromatics with oxygenated fragments. The major competing reaction to the aromatic production is the formation of coke. Coke is formed through intermediate furan polymers which ultimately decompose to unsaturated coke. To achieve maximum aromatic yields, pyrolysis should proceed with rapid decomposition of glucose to oxygenates to react with the catalyst. The concentration of oxygenates should remain low to avoid formation of coke and less desirable polycyclic aromatics.

We established the fundamental relationship between zeolite pore size/structure and glucose conversion into aromatics. For this study, a range of zeolites, including small pore zeolites (ZK-5 and SAPO-34), medium pore zeolites (Ferrierite, ZSM-23, MCM-22, SSZ-20, ZSM-11, ZSM-5, IM-5, and TNU-9), and large pore zeolites(SSZ-55, beta, Y zeolite), were synthesized, characterized, and tested for CFP of glucose. The aromatic yield is a function of the pore size and internal pore space of the zeolite catalyst. Aromatic yields were highest in the medium-pore zeolites with pore sizes in the range of 5.2 to 5.9 Å. In addition to micropore diameter, internal pore space and steric hindrance played a determining role for aromatic production. Medium-pore zeolites with moderate internal pore space and steric hindrance (ZSM-5 and ZSM-11) gave the highest aromatic yield and the least coke formation. The remarkable catalytic activity of these medium pore zeolites is due to the fact that the majority of aromatics and oxygenated species present during the reaction fit inside the pores of most medium pore zeolites. Zeolites with small pores severely hinder the diffusion of both reactants and products. Zeolites with large pores allow for faster reactant diffusion, but the formation of coke within the zeolite micropores becomes more prevalent due to the lack of reactant confinement.

We have developed improved ZSM-5 based catalysts to enhance aromatic production from CFP by (1) adjusting the concentration of acid sites inside the zeolites catalyst; (2) addition of Ga to the ZSM-5 to create new type of active sites; (3) incorporation of mesoporosity into the ZSM-5 framework to enhance its diffusion characteristics. The optimum aluminum content of the ZSM-5 catalyst for CFP of glucose to maximize the aromatic yield occurs at a SAR of 30. This composition is thought to have the optimum acid concentration and hydrophilicity of the zeolite framework, for aromatic formation. ZSM-5 catalyst with SAR of 30 was further modified by incorporation of Gallium. Ga promoted ZSM-5 increased the aromatic yield over 40% for CFP of pine wood. Furan conversion studies over Ga/ZSM-5 suggest that the catalyst is a bifunctional catalyst where the Ga increases the rate of decarbonylation and olefin aromatization, whereas the zeolite catalyzes the other reactions necessary for aromatic production. Aside from controlling the active sites of ZSM-5, the pore structure of ZSM-5 was also modified by creating hierarchical mesopores within the ZSM-5 to improve the accessibility of biomass-derived compounds into the micropores during CFP. Mesoporous ZSM-5 shifted the aromatic distribution toward heavier alkylated monoaromatics, showing a similar aromatic yield to ZSM-5 for CFP of maple wood. The production of lager alkylaromatics is due to the relaxation of shape-selectivity controlling the product distribution by the presence of mesoporosity.

We demonstrated the scale-up of the CFP process in the process development unit by producing liter quantities of aromatic products directly from solid biomass. The process development unit was designed and built for continuous operation of the CFP process at steady state over long durations. The effects of operating conditions on the yield and selectivity of aromatic and olefin products were studied to optimize the reactor performance. The optimal operating conditions for CFP of pine wood in the process development unit were: a temperature of 600 °C, WHSV of 0.3 h^{-1}, catalyst to biomass ratio of 6, fluidization gas flow rate of 3.2 slpm, and static bed height of 4 inch. At these conditions, the highest aromatic yield of 15.1 % and the olefin yield of 7.8% were obtained. The stability of the ZSM-5 catalyst during extended operation was studied with the catalyst up to 30 successive reaction-regeneration cycles. The catalyst retained most of the activity after 30 reaction-regeneration cycles, but some loss in acid sites were observed due to mineral impurities (ash) from the biomass.

Additionally, we estimated the potential for integration of the CFP process with the other biomass conversion technologies, hydrolysis and pyrolysis, with the goal of maximizing the production of fuel precursors from the biomass. It was found that combining CFP with hydrolysis is an attractive route in an integrated biorefinery because CFP can convert solid waste stream (lignin residues) into aromatics, while aqueous sugar solutions produced by hydrolysis can be easily fermented to alcohols or converted into alkanes by liquid phase processing. This route can increase the overall energy output of the biomass by two times as much as the direct application of the CFP process to the biomass.

The CFP process still has much room for improvements. Although we discovered a new catalyst, Ga/H-ZSM-5, that can significantly enhance aromatic production from CFP of biomass and demonstrated the scale-up of the CFP process in this study, further research needs to be undertaken to optimize the CFP reactor and catalytic chemistry. Currently, on an energy basis, 41% of the energy of the wood can be converted into aromatics in the fluidized bed reactor, using Ga/H-ZSM-5. Competing technologies such as production of cellulosic ethanol by hydrolysis/fermentation have demonstrated that 49% of the energy of the biomass feed is converted into ethanol. However, it should be noted that this technology is significantly more complicated than the single step process of CFP. Aromatics also have a higher value than ethanol because aromatics can be used as an octane enhancer or as petrochemical feedstocks. More research in catalysis and reaction engineering can optimize the CFP reactor and the catalyst to obtain higher energy yields than the other biomass conversion technologies.

8.2 Future Work

For future work, more experiments need to be undertaken in the process development unit for practical application. In an industrial setting, the gases produced during CFP reaction would be recycled for fluidization. In CFP, the producer gas is composed of a mixture of carbon monoxide, carbon dioxide, methane, ethylene, and propylene. While nitrogen used for CFP as a fluidization gas in this work is an inert gas, the producer gas might impact the reaction chemistry. Hence, the effect of the producer gas on the CFP of biomass needs to be addressed for industrial application. In addition, irreversible deactivation of the catalyst during CFP was observed after 30 times reaction-regeneration cycles with 30% reduction in acid sites of the catalyst (Section 7.3.2). This is likely due to the ash from the biomass, poisoning the acid sites. Therefore, future studies need to focus on the efficient removal of the ash from the catalyst to avoid the catalyst deactivation. A fluidized bed reactor type regenerator might work for separating the ash from the catalyst where a high velocity of gas stream would carry over the small ash particles with the gas as entrainment whereas the catalyst particles circulate within the catalyst bed.

Aside from the process development unit experiments, fundamental questions related to the effect of modifying ZSM-5 catalyst properties on the CFP reaction should be addressed to develop improved catalysts for the CFP process. Firstly, the role of silica to alumina ratio on CFP reaction needs to be studied in detail (Section 6.3.1). It was observed that the appearance of closely located Brønsted acid sites and the increase in hydrophilicity inside the zeolite with incorporation of more aluminum into ZSM-5 framework play an important role on achieving high yields of aromatics from glucose CFP. Therefore, it is important to understand how the change in the hydrophilic character of the ZSM-5 will affect the adsorption behavior of pyrolysis oxygenates in the ZSM-5. Further detailed studies on polarity of pyrolysis oxygenates and their adsorption in the zeolite will provide a clear understanding of the effect of changing the silica to alumina ratio of the ZSM-5 on the CFP reaction.

Secondly, the effect of controlling the diffusion characteristics of the ZSM-5 catalyst on the CFP reaction should be studied in detail with further catalyst characterizations (e.g. diffusivity measurement) together with activity measurements in a flow reactor. It has been shown that furan reaction over ZSM-5 is under strong pore diffusion limited conditions [29]. Thus, any improvements in the diffusion properties in ZSM-5 can have a positive effect on catalytic activity. Our results in Section 6.3.2 showed that the improvements in diffusion properties of ZSM-5 by decreasing the particle size of ZSM-5 catalyst enhanced the aromatic yield from CFP of glucose. However, besides the particle size, the crystallite size of each catalyst particle is more relevant to the molecular diffusion in the zeolite channel. Future studies of the effects of crystal sizes of ZSM-5 catalysts on conversion and turnover frequency (TOF) in CFP reaction will provide a better insight into the diffusion effects on the CFP reaction.

Thirdly, the exterior surface sites of the mesoporous ZSM-5 catalyst should be better tuned to decrease the undesired coke formation. It has been shown for methanol conversion that mesoporous ZSM-5 could increase the catalyst lifetime due to the faster removal of products and facile diffusion of coke precursors through mesopore walls in the zeolite [198-199]. However, the mesoporous ZSM-5 showed the high amount of coke formation and fast deactivation rate for the CFP reaction (Section 6.3.3). This is likely due to preferential coke formation through the polymerization of furan intermediates in the mesopores. In this work, tartaric acid treatment was used to selectively remove the exterior surface sites of the mesoporous ZSM-5; however, this method did not show the effectiveness in the reduction of coke formation. Therefore, more selective methods for removal of the surface acid sites should be studied to improve the catalytic properties of the mesoporous ZSM-5 for the CFP reaction.

Lastly, the location of Gallium in the ZSM-5 catalyst and its role on the CFP reaction need to be studied in detail. The results in this work suggested that some of the protons in the ZSM-5 were replaced by Gallium, evidenced in the reduction of concentration of Bronsted acid sites in Ga/HZSM-5 catalyst (Section 6.3.4). However, the exact state and location of Gallium within the ZSM-5 catalyst should be elucidated with other techniques (e.g. IR and MAS-NMR) combined with DFT calculations. In this work, it is suggested that the Ga/HZSM-5 enhances aromatic production by increasing the rate of decarbonylation (e.g. furan conversion into allene) and olefins aromatization (See Figure 6.15). However, it has also been shown that Ga/HZSM-5 has high rates of dehydrogenation and light alkane aromatization [200]. Therefore, more mechanistic studies will provide a better insight into the exact role of Ga species on the CFP reaction. It is likely that fundamental understanding of these catalyst properties on the CFP reaction will lead to the development of new zeolite catalysts for efficient conversion of biomass into aromatics.

BIBLIOGRAPHY

[1] L.R. Lynd, J.H. Cushman, R.J. Nichols, C.E. Wyman, Science, 251 (1991) 1318-1323.

[2] T.E. Bull, Science, 285 (1999) 1209-1209.

[3] G.W. Huber, S. Iborra, A. Corma, Chemical Reviews, 106 (2006) 4044-4098.

[4] L.R. Lynd, C.E. Wyman, T.U. Gerngross, Biotechnology Progress, 15 (1999) 777-793.

[5] A. Aden, M. Ruth, K. Ibsen, J. Jechura, K. Neeves, J. Sheehan, B. Wallace, L. Montague, A. Slayton, J. Lukas, in, National Renewable Energy Laboratory, Golden,CO, 2002.

[6] G.W. Huber, J.N. Chheda, C.J. Barrett, J.A. Dumesic, Science, 308 (2005) 1446-1450.

[7] A.V. Bridgwater, Chemical Engineering Journal, 91 (2003) 87-102.

[8] A.V. Bridgwater, Thermal Science, 8 (2004) 21.

[9] A.V. Bridgwater, Chem. Eng. J., 91 (2003) 87.

[10] A.V. Bridgwater, D. Meier, D. Radlein, Org. Geochem., 30 (1999) 1479-1493.

[11] D. Mohan, C.U. Pittman, P.H. Steele, Energy Fuels, 20 (2006) 848-889.

[12] D.C. Elliott, D. Beckman, A.V. Bridgwater, J.P. Diebold, S.B. Gevert, Y. Solantausta, Energy Fuels, 5 (1991) 399-410.

[13] D.C. Elliott, A. Oasmaa, Energy Fuels, 5 (1991) 102-109.

[14] T.P. Vispute, G.W. Huber, Green Chem., 11 (2009) 1433-1445.

[15] T.P. Vispute, H.Y. Zhang, A. Sanna, R. Xiao, G.W. Huber, Science, 330 (2010) 1222-1227.

[16] F.Y. Gong, Z. Yang, C.G. Hong, W.W. Huang, S. Ning, Z.X. Zhang, Y. Xu, Q.X. Li, Bioresour. Technol., 102 (2011) 9247-9254.

[17] H.Y. Zhang, Y.T. Cheng, T.P. Vispute, R. Xiao, G.W. Huber, Energy Environ. Sci., 4 (2011) 2297-2307.

[18] Y. Zhao, L. Deng, B. Liao, Y. Fu, Q.X. Guo, Energy Fuels, 24 (2010) 5735-5740.

[19] H.J. Park, H.S. Heo, J.K. Jeon, J. Kim, R. Ryoo, K.E. Jeong, Y.K. Park, Appl. Catal. B-Environ., 95 (2010) 365-373.

[20] B. Valle, A.G. Gayubo, A.T. Aguayo, M. Olazar, J. Bilbao, Energy Fuels, 24 (2010) 2060-2070.

[21] A.G. Gayubo, B. Valle, A.T. Aguayo, M. Olazar, J. Bilbao, Ind. Eng. Chem. Res., 49 (2010) 123-131.

[22] J.D. Adjaye, N.N. Bakhshi, Fuel Process. Technol., 45 (1995) 185-202.

[23] J.D. Adjaye, N.N. Bakhshi, Fuel Process. Technol., 45 (1995) 161-183.

[24] T.R. Carlson, Y.T. Cheng, J. Jae, G.W. Huber, Energy Environ. Sci., 4 (2011) 145-161.

[25] T.R. Carlson, T.P. Vispute, G.W. Huber, ChemSusChem, 1 (2008) 397-400.

[26] T.R. Carlson, G.A. Tompsett, W.C. Conner, G.W. Huber, Top. Catal., 52 (2009) 241-252.

[27] H.Y. Zhang, R. Xiao, H. Huang, G. Xiao, Bioresour. Technol., 100 (2009) 1428-1434.

[28] Y.C. Lin, J. Cho, G.A. Tompsett, P.R. Westmoreland, G.W. Huber, J. Phys. Chem. C, 113 (2009) 20097-20107.

[29] Y.T. Cheng, G.W. Huber, ACS Catal., 1 (2011) 611-628.

[30] R.J. Evans, T.A. Milne, Energy Fuels, 1 (1987) 123-137.

[31] N.Y. Chen, T.F. Degnan, Jr., L.R. Koenig, Chemtech, 16 (1986) 506-511.

[32] M.I. Hanniff, L.H. Dao, Applied Catalysis, 39 (1988) 33-47.

[33] A. Pattiya, J.O. Titiloye, A.V. Bridgwater, J. Anal. Appl. Pyrolysis, 81 (2008) 72-79.

[34] A. Aho, N. Kumar, K. Eranen, T. Salmi, M. Hupa, D.Y. Murzin, Fuel, 87 (2008) 2493-2501.

[35] J. Adam, E. Antonakou, A. Lappas, M. Stocker, M.H. Nilsen, A. Bouzga, J.E. Hustad, G. Oye, Microporous Mesoporous Mat., 96 (2006) 93-101.

[36] D.J. Mihalcik, C.A. Mullen, A.A. Boateng, J. Anal. Appl. Pyrolysis, 92 (2011) 224-232.

[37] J. Jae, G.A. Tompsett, A.J. Foster, K.D. Hammond, S.M. Auerbach, R.F. Lobo, G.W. Huber, J. Catal., 279 (2011) 257-268.

[38] R. French, S. Czernik, Fuel Process. Technol., 91 (2010) 25-32.

[39] A. Ausavasukhi, T. Sooknoi, D.E. Resasco, J. Catal., 268 (2009) 68-78.

[40] M. Olazar, R. Aguado, J. Bilbao, A. Barona, Aiche J., 46 (2000) 1025-1033.

[41] A.A. Lappas, M.C. Samolada, D.K. Iatridis, S.S. Voutetakis, I.A. Vasalos, Fuel, 81 (2002) 2087-2095.

[42] K. Bilba, A. Ouensanga, Journal Of Analytical And Applied Pyrolysis, 38 (1996) 61-73.

[43] R.K. Sharma, J.B. Wooten, V.L. Baliga, M.R. Hajaligol, Fuel, 80 (2001) 1825-1836.

[44] B. Yang, Wyman, C.E., Methods in Molecular Biology, (2009) 103-114.

[45] M. Selig, Weiss, N., Ji, Y., Laboratory Analytical Procedure (LAP), (3/21/2008).

[46] A. Sluiter, B. Hames, R. Ruiz, C. Scarlata, J. Sluiter, D. Templeton, in: Laboratory Analytical Procedures, National Renewable Energy Laboratory, Golden, CO, 2005.

[47] R. Ruiz, T. Ehrman, in: Laboratory Analytical Procedure No. 002, National Renewable Energy Laboratory, Golden, CO, 1996a.

[48] R. Ruiz, T. Ehrman, in: Laboratory Analytical Procedure No. 014. , National Renewable Energy Laboratory, Golden, CO, 1996b.

[49] A. Sluiter, B. Hames, R. Ruiz, C. Scarlata, J. Sluiter, D. Templeton, D. Crocker, in: Laboratory Analytical Procedure, National Renewable Energy Laboratory:, Golden, CO, 2006.

[50] A. Sluiter, B. Hames, R. Ruiz, C. Scarlata, J. Sluiter, D. Templeton, in: Laboratory Analytical Procedures, National Renewable Energy Laboratory, Golden, CO, 2005.

[51] N. Mosier, C. Wyman, B. Dale, R. Elander, Y.Y. Lee, M. Holtzapple, M. Ladisch, Bioresour. Technol., 96 (2005) 673-686.

[52] T.A. Lloyd, C.E. Wyman, Bioresource Technology, 96 (2005) 1967-1977.

[53] H.P. Yang, R. Yan, H.P. Chen, D.H. Lee, C.G. Zheng, Fuel, 86 (2007) 1781-1788.

[54] Y.-C. Lin, Cho, J., Geoffrey, T.A., Westmoreland, P.R. and Huber, G.W., J. Phys. Chem. C, 113 (2009) 20097–20107.

[55] A.V. Bridgwater, D. Meier, D. Radlein, in: Workshop on Optimisation of Biomass Pyrolysis for Fluid Fuel Production, Pergamon-Elsevier Science Ltd, Os, Norway, 1998, pp. 1479-1493.

[56] G.V.C. Peacocke, E.S. Madrali, C.Z. Li, A.J. Guell, F. Wu, R. Kandiyoti, A.V. Bridgwater, in: Symposium on Fast Pyrolysis - Processes, Technologies and Products, at the 205th ACS National Meeting and Exposition Program, Pergamon-Elsevier Science Ltd, Denver, Co, 1993, pp. 155-167.

[57] J. Piskorz, D.S. Scott, D. Radlein, Acs Symposium Series, 376 (1988) 167-178.

[58] A.V. Bridgwater, G.V.C. Peacocke, Renew. Sust. Energ. Rev., 4 (2000) 1-73.

[59] A.V. Bridgwater, J. Anal. Appl. Pyrolysis, 51 (1999) 3-22.

[60] A.V. Bridgwater, in: 15th International Conference on Chemical Reactor Modeling (CHEMREACTOR 15), Elsevier Science Sa, Helsinki, Finland, 2001, pp. 87-102.

[61] T.L. Marker, in: Final Technical Report, U.S. Department of Energy, 2005.

[62] C.E. Wyman, MRS Bull., 33 (2008) 381-383.

[63] L.R. Lynd, M.S. Laser, D. Brandsby, B.E. Dale, B. Davison, R. Hamilton, M. Himmel, M. Keller, J.D. McMillan, J. Sheehan, C.E. Wyman, Nat. Biotechnol., 26 (2008) 169-172.

[64] S. Kim, B.E. Dale, Biomass Bioenerg., 26 (2004) 361-375.

[65] G.W. Huber, J.A. Dumesic, in: Symposium on Frontiers in Catalysis - A Molecular View of Inddustrial Catalysis held in Honour of Jens R Rostrup-Nielson/Henrik Topsoe, Elsevier Science Bv, Hornbaek, DENMARK, 2005, pp. 119-132.

[66] G.W. Huber, R.D. Cortright, J.A. Dumesic, Angew. Chem.-Int. Edit., 43 (2004) 1549-1551.

[67] D.C. Elliott, Energy Fuels, 21 (2007) 1792-1815.

[68] G.W. Huber, A. Corma, Angew. Chem.-Int. Edit., 46 (2007) 7184-7201.

[69] E.B. Sanders, A.I. Goldsmith, J.I. Seeman, Journal of Analytical and Applied Pyrolysis, 66 (2003) 29-50.

[70] M. Bjorgen, S. Svelle, F. Joensen, J. Nerlov, S. Kolboe, F. Bonino, L. Palumbo, S. Bordiga, U. Olsbye, J. Catal., 249 (2007) 195-207.

[71] J.B. Paine, Y.B. Pithawalla, J.D. Naworal, Journal Of Analytical And Applied Pyrolysis, 82 (2008) 10-41.

[72] J.B. Paine, Y.B. Pithawalla, J.D. Naworal, Journal Of Analytical And Applied Pyrolysis, 82 (2008) 42-69.

[73] D.R. Lide, 89 ed., CRC Press, Boca Raton, Fla, 2008.

[74] Z. Sarbak, Reaction Kinetics and Catalysis Letters, 69 (2000) 177-181.

[75] A. Miecznikowski, J. Hanuza, Zeolites, 7 (1987) 249-254.

[76] P. Walther, Zeitschrift fuer Physikalische Chemie (Leipzig), 269 (1988) 809-812.

[77] H.A. Wells, Jr., R.H. Atalla, Journal of Molecular Structure, 224 (1990) 385-424.

[78] D.M. Ruthven, B.K. Kaul, Ind. Eng. Chem. Res., 32 (1993) 2053-2057.

[79] M. Cook, W.C. Conner, in: Proceedings of the International Zeolite Conference, 12th, July 5-10, 1998, Baltimore, 1999, pp. 409-414.

[80] S. Bertarione, F. Bonino, F. Cesano, A. Damin, D. Scarano, A. Zecchina, J. Phys. Chem. B, 112 (2008) 2580-2589.

[81] J.A. Biscardi, E. Iglesia, Journal Of Physical Chemistry B, 102 (1998) 9284-9289.

[82] J.A. Biscardi, E. Iglesia, J. Catal., 182 (1999) 117-128.

[83] J.F. Haw, W.G. Song, D.M. Marcus, J.B. Nicholas, Accounts Chem. Res., 36 (2003) 317-326.

[84] D.M. McCann, D. Lesthaeghe, P.W. Kletnieks, D.R. Guenther, M.J. Hayman, V. Van Speybroeck, M. Waroquier, J.F. Haw, Angewandte Chemie-International Edition, 47 (2008) 5179-5182.

[85] J.B. Paine, Y.B. Pithawalla, J.D. Naworal, Journal Of Analytical And Applied Pyrolysis, 83 (2008) 37-63.

[86] K. Lourvanij, G.L. Rorrer, J. Chem. Technol. Biotechnol., 69 (1997) 35-44.

[87] P.T. Williams, S. Besler, Advances in thermochemical biomass conversion, 2 (1994) 771-783.

[88] Ramos-Sanchez C, Rey FJ, Rodriguezmendez L, Martingil FJ, M. J, Thermochim. Acta, 134 (1988).

[89] M. Stocker, Microporous Mesoporous Mat., 29 (1999) 3-48.

[90] T.R. Carlson, J. Jae, G.W. Huber, Chemcatchem, 1 (2009) 107-110.

[91] M. Choura, N. M. Belgacem, A. Gandini, Macromolecules, 29 (1996) 3839.

[92] R.T. Conley, I. Metil, Journal of Applied Polymer Science, 7 (1963) 37.

[93] D. Mores, E. Stavitski, M.H.F. Kox, J. Kornatowski, U. Olsbye, B.M. Weckhuysen, Chem.-Eur. J., 14 (2008) 11320-11327.

[94] N.K. Bar, F. Bauer, D.M. Ruthven, B.J. Balcom, J. Catal., 208 (2002) 224-228.

[95] M. Bjorgen, U. Olsbye, S. Kolboe, J. Catal., 215 (2003) 30-44.

[96] D.W. Breck, in, Wiley, New York, 1974.

[97] http://www.iza-online.org

[98] B. Smit, T.L.M. Maesen, Chem. Rev., 108 (2008) 4125-4184.

[99] R.M. Barrer, in, Academic Press Inc., New York, 1978.

[100] P.B. Weisz, Pure Appl. Chem., 52 (1980) 2091-2103.

[101] S.M. Csicsery, Zeolites, 4 (1984) 202-213.

[102] S.M. Csicsery, Chem. Br., 21 (1985) 473-&.

[103] J.C. Cheng, T.F. Degnan, J.S. Beck, Y.Y. Huang, M. Kalyanaraman, J.A. Kowalski, C.A. Loehr, D.N. Mazzone, in: H. Hattori, K. Otsuka (Eds.) Science and Technology in Catalysis 1998, Elsevier Science Publ B V, Amsterdam, 1999, pp. 53-60.

[104] G. Sastre, C.R.A. Catlow, A. Corma, J. Phys. Chem. B, 103 (1999) 5187-5196.

[105] E.G. Derouane, J.B. Nagy, C. Fernandez, Z. Gabelica, E. Laurent, P. Maljean, Applied Catalysis, 40 (1988) L1-L10.

[106] E.G. Derouane, J.B. Nagy, Applied Catalysis, 52 (1989) 169-170.

[107] E.G. Derouane, J. Mol. Catal. A-Chem., 134 (1998) 29-45.

[108] A. Pattiya, J.O. Titiloye, A.V. Bridgwater, Fuel, 89 (2010) 244-253.

[109] A. Corma, G.W. Huber, L. Sauvanaud, P. O'Connor, J. Catal., 247 (2007) 307-327.

[110] R.K. Sharma, N.N. Bakhshi, Energy Fuels, 7 (1993) 306-314.

[111] S.P.R. Katikaneni, J.D. Adjaye, N.N. Bakhshi, Energy Fuels, 9 (1995) 1065-1078.

[112] P.T. Williams, P.A. Horne, Fuel, 74 (1995) 1839-1851.

[113] P.T. Williams, P.A. Horne, J. Anal. Appl. Pyrolysis, 31 (1995) 39-61.

[114] P.T. Williams, P.A. Horne, J. Inst. Energy, 69 (1996) 176-191.

[115] S. Vitolo, B. Bresci, M. Seggiani, M.G. Gallo, Fuel, 80 (2000) 17-26.

[116] J.D. Adjaye, N.N. Bakhshi, Biomass and Bioenergy, 7 (1994) 201-211.

[117] S.D. Kim, S.H. Noh, K.H. Seong, W.J. Kim, Microporous Mesoporous Mat., 72 (2004) 185-192.

[118] A. Corma, C. Corell, J. Perezpariente, Zeolites, 15 (1995) 2-8.

[119] S.B. Hong, H.K. Min, C.H. Shin, P.A. Cox, S.J. Warrender, P.A. Wright, J. Am. Chem. Soc., 129 (2007) 10870-10885.

[120] S.H. Lee, D.K. Lee, C.H. Shin, Y.K. Park, P.A. Wright, W.M. Lee, S.B. Hong, J. Catal., 215 (2003) 151-170.

[121] G. Gonzalez, M.E. Gomes, G. Vitale, G.R. Castro, Microporous Mesoporous Mat., 121 (2009) 26-33.

[122] G.A. Jablonski, L.B. Sand, J.A. Gard, Zeolites, 6 (1986) 396-402.

[123] S.H. Jhung, J.S. Chang, J.S. Hwang, S.E. Park, Microporous Mesoporous Mat., 64 (2003) 33-39.

[124] Z.R. Zhu, Q.L. Chen, Z.K. Xie, W.M. Yang, C. Li, Microporous Mesoporous Mat., 88 (2006) 16-21.

[125] M.D. Macedonia, E.J. Maginn, Aiche J., 46 (2000) 2504-2517.

[126] S.I. Zones, T.V. Harris, Microporous Mesoporous Mat., 35-6 (2000) 31-46.

[127] N.Y. Chen, W.E. Garwood, J. Catal., 52 (1978) 453-458.

[128] S.I. Zones, C.Y. Chen, A. Corma, M.T. Cheng, C.L. Kibby, I.Y. Chan, A.W. Burton, J. Catal., 250 (2007) 41-54.

[129] Y.F. Chu, in: US Patent, 1990.

[130] J. Houzvicka, S. Hansildaar, V. Ponec, J. Catal., 167 (1997) 273-278.

[131] M.D.S. Machado, J. Perez-Pariente, E. Sastre, D. Cardoso, M.V. Giotto, J.L. Garcia-Fierro, V. Fornes, J. Catal., 205 (2002) 299-308.

[132] R.B. Bird, W.E. Stewart, E.N. Lightfoot, John Wiley & Sons, New York, 1960.

[133] D.R. Lide, CRC, 2008.

[134] C.L. Yaws, McGraw Hill, New York, 1999.

[135] http://cccbdb.nist.gov/

[136] H. Wang, M. Frenklach, Combustion and Flame, 96 (1994) 163-170.

[137] M.J. Frisch, G.W. Trucks, H.B. Schlegel, G.E. Scuseria, M.A. Robb, J.R. Cheeseman, J. J. A. Montgomery, T. Vreven, K.N. Kudin, J.C. Burant, J.M. Millam, S.S. Iyengar, J. Tomasi, V. Barone, B. Mennucci, M. Cossi, G. Scalmani, N. Rega, G.A. Petersson, H. Nakatsuji, M. Hada, M. Ehara, K. Toyota, R. Fukuda, J. Hasegawa, T. Nakajima, Y. Honda, O. Kitao, H. Nakai, M. Klene, X. Li, J.E. Knox, H.P. Hratchian, J.B.

Cross, V. Bakken, C. Adamo, J. Jaramillo, R. Gomperts, R.E. Stratmann, O. Yazyev, A.J. Austin, R. Cammi, C. Pomelli, J.W. Ochterski, P.Y. Ayala, K. Morokuma, G.A. Voth, P. Salvador, J.J. Dannenberg, V.G. Zakrzewski, S. Dapprich, A.D. Daniels, M.C. Strain, O. Farkas, D.K. Malick, A.D. Rabuck, K. Raghavachari, J.B. Foresman, J.V. Ortiz, Q. Cui, A.G. Baboul, S. Clifford, J. Cioslowski, B.B. Stefanov, G. Liu, A. Liashenko, P. Piskorz, I. Komaromi, R.L. Martin, D.J. Fox, T. Keith, M.A. Al-Laham, C.Y. Peng, A. Nanayakkara, M. Challacombe, P.M.W. Gill, B. Johnson, W. Chen, M.W. Wong, C. Gonzalez, J.A. Pople, in, Gaussian, Inc., Wallingford, CT, 2003.

[138] A.D. Becke, Journal of Chemical Physics, 98 (1993) 5648-5652.

[139] C.Y. Lee, Weitao; and Parr, Robert G. , Physical Review B, 37 (1988) 785-789.

[140] P.J.D. Stephens, F. J.; Chabalowski, C. F.; and Frisch, M. J., Journal of Physical Chemistry, 98 (1994) 11623-11627.

[141] W.J. Hehre, R. Ditchfield, J.A. Pople, Journal of Chemical Physics, 56 (1972) 2257-2261.

[142] P.C. Hariharan, J.A. Pople, Thermochimica Acta, 28 (1973) 213-222.

[143] P.C. Hariharan, J.A. Pople, Molecular Physics, 27 (1974) 209-214.

[144] M.M. Francl, W.J. Pietro, W.J. Hehre, J.S. Binkley, M.S. Gordon, D.J. DeFrees, J.A. Pople, Journal of Chemical Physics, 77 (1982) 3654--3665.

[145] M. Krossner, J. Sauer, J. Phys. Chem., 100 (1996) 6199-6211.

[146] R. Netrabukkana, K. Lourvanij, G.L. Rorrer, Ind. Eng. Chem. Res., 35 (1996) 458-464.

[147] S. Li, V.A. Tuan, J.L. Falconer, R.D. Noble, J. Membr. Sci., 191 (2001) 53-59.

[148] D. Topgaard, O. Soederman, Langmuir, 17 (2001) 2694-2702.

[149] T.C. Bowen, Richard D. Noble, J.L. Falconer, J. Membr. Sci., 245 (2004) 1-33.

[150] V.R. Choudhary, Vikram S. Nayak, T.V. Choudhary, Ind. Eng. Chem. Res., 36 (1997) 1812-1818.

[151] C.D. Baertsch, H.H. Funke, J.L. Falconer, R.D. Noble, J. Phys. Chem., 100 (1996) 7676-7679.

[152] C.E. Webster, R.S. Drago, M.C. Zerner, J. Phys. Chem. B, 103 (1999) 1242-1249.

[153] J. Cejka, J. Kotrla, A. Krejci, Appl. Catal. A-Gen., 277 (2004) 191-199.

[154] N.M. Tukur, S. Al-Khattaf, Energy Fuels, 21 (2007) 2499-2508.

[155] R.M. Moore, Chemical Engineering Journal, 6 (1971) 38.

[156] N. Kraikul, P. Rangsunvigit, S. Kulprathipanja, Adsorption, 12 (2006) 317-327.

[157] E.H. Ellison, J. Phys. Chem. B, 103 (1999) 9314-9320.

[158] T.R. Carlson, J. Jae, Y.C. Lin, G.A. Tompsett, G.W. Huber, J. Catal., 270 (2010) 110-124.

[159] V.J. Frillette, W.O. Haag, R.M. Lago, J. Catal., 67 (1981) 218-222.

[160] J.R. Carpenter, S. Yeh, S.I. Zones, M.E. Davis, J. Catal., 269 (2010) 64-70.

[161] W. Fan, M.A. Snyder, S. Kumar, P.S. Lee, W.C. Yoo, A.V. McCormick, R.L. Penn, A. Stein, M. Tsapatsis, Nat. Mater., 7 (2008) 984-991.

[162] M. Hartmann, Angew. Chem.-Int. Edit., 43 (2004) 5880-5882.

[163] J. Perez-Ramirez, C.H. Christensen, K. Egeblad, J.C. Groen, Chem. Soc. Rev., 37 (2008) 2530-2542.

[164] M. Choi, K. Na, J. Kim, Y. Sakamoto, O. Terasaki, R. Ryoo, Nature, 461 (2009) 246-U120.

[165] C.M. Lew, R. Cai, Y. Yan, Accounts of Chemical Research, 43 (2009) 210-219.

[166] S. van Donk, A.H. Janssen, J.H. Bitter, K.P. de Jong, Catalysis Reviews, 45 (2003) 297-319.

[167] S. Zheng, H.R. Heydenrych, A. Jentys, J.A. Lercher, Journal of Physical Chemistry B, 106 (2002) 9552-9558.

[168] Y. Ono, Catal. Rev.-Sci. Eng., 34 (1992) 179-226.

[169] G. Krishnamurthy, A. Bhan, W.N. Delgass, J. Catal., 271 (2010) 370-385.

[170] V.R. Choudhary, A.K. Kinage, T.V. Choudhary, Science, 275 (1997) 1286-1288.

[171] A. Bhan, W.N. Delgass, Catal. Rev.-Sci. Eng., 50 (2008) 19-151.

[172] V.R. Choudhary, P. Devadas, S. Banerjee, A.K. Kinage, Microporous Mesoporous Mat., 47 (2001) 253-267.

[173] V.R. Choudhary, S. Banerjee, D. Panjala, Microporous Mesoporous Mat., 51 (2002) 203-210.

[174] M. Choi, H.S. Cho, R. Srivastava, C. Venkatesan, D.H. Choi, R. Ryoo, Nat. Mater., 5 (2006) 718-723.

[175] R. Srivastava, M. Choi, R. Ryoo, Chem. Commun., (2006) 4489-4491.

[176] V.R. Choudhary, A.K. Kinage, A.A. Belhekar, Zeolites, 18 (1997) 274-277.

[177] V.R. Choudhary, A.K. Kinage, Zeolites, 15 (1995) 732-738.

[178] V.R. Choudhary, A.K. Kinage, C. Sivadinarayana, P. Devadas, S.D. Sansare, M. Guisnet, J. Catal., 158 (1996) 34-50.

[179] L. Rodriguez-Gonzalez, F. Hermes, M. Bertmer, E. Rodriguez-Castellon, A. Jimenez-Lopez, U. Simon, Applied Catalysis A: General, 328 (2007) 174-182.

[180] T.R. Carlson, J. Jae, Y.C. Lin, G.A. Tompsett, G.W. Huber, Journal of Catalysis, 270 (2010) 110-124.

[181] A. Ausavasukhi, T. Sooknoi, D.E. Resasco, Journal of Catalysis, 268 (2009) 68-78.

[182] P.A. Horne, P.T. Williams, Renewable Energy, 7 (1996) 131-144.

[183] A.M. Azeez, D. Meier, J. Odermatt, T. Willner, Energy & Fuels, 24 (2010) 2078-2085.

[184] T.A. Peters, J. van der Tuin, C. Houssin, M.A.G. Vorstman, N.E. Benes, Z.A.E.P. Vroon, A. Holmen, Catalysis Today, 104 (2005) 288-295.

[185] J. Zhao, W. Guo, G. Liu, X. Zhang, L. Wang, Fuel Processing Technology, 91 (2010) 1090-1097.

[186] Y.N. Li, S.L. Liu, Z.K. Zhang, S.J. Me, X.X. Zhu, L.Y. Xu, Appl. Catal. A-Gen., 338 (2008) 100-113.

[187] X.L. Zhu, L.L. Lobban, R.G. Mallinson, D.E. Resasco, J. Catal., 271 (2010) 88-98.

[188] T.Q. Hoang, X.L. Zhu, L.L. Lobban, D.E. Resasco, R.G. Mallinson, Catal. Commun., 11 (2010) 977-981.

[189] V.N. Shetti, J. Kim, R. Srivastava, M. Choi, R. Ryoo, Journal of Catalysis, 254 (2008) 296-303.

[190] C. Fernandez, I. Stan, J.-P. Gilson, K. Thomas, A. Vicente, A. Bonilla, J. Perez-Ramirez, Chemistry: A European Journal, 16 (2010) 6224-6233.

[191] T.Q. Hoang, X. Zhu, L.L. Lobban, D.E. Resasco, R.G. Mallinson, Catalysis Communications, 11 (2010) 977-981.

[192] T.V. Choudhary, A. Kinage, S. Banerjee, V.R. Choudhary, Energy Fuels, 20 (2006) 919-922.

[193] Y.-T. Cheng, J. Jae, J. Shi, W. Fan, G.W. Huber, Angew. Chem.-Int. Edit., (in-press).

[194] O. Levenspiel, 3 ed., Wiley, 1998.

[195] http://www.engin.umich.edu/~cre/12chap/html/12prof2a.htm.

[196] R. Xiao, B.S. Jin, H.C. Zhou, Z.P. Zhong, M.Y. Zhang, Energy Conv. Manag., 48 (2007) 778-786.

[197] A.G. Gayubo, A.T. Aguayo, A. Atutxa, R. Prieto, J. Bilbao, Ind. Eng. Chem. Res., 43 (2004) 5042-5048.

[198] J. Kim, M. Choi, R. Ryoo, J. Catal., 269 (2010) 219-228.

[199] A.A. Rownaghi, F. Rezaei, J. Hedlund, Microporous Mesoporous Mat., 151 (2012) 26-33.

[200] E.J.M. Hensen, E.A. Pidko, N. Rane, R.A. van Santen, Angew. Chem.-Int. Edit., 46 (2007) 7273-7276.